GRAPHENE NANOSTRUCTURED MATERIALS: SELF-ASSEMBLED STRUCTURES AND NANO-CARRIERS FOR ENERGY STORAGE AND AEROSPACE

by

KURT BRADLEY SMITH

A dissertation submitted to the

School of Graduate Studies

Rutgers, The State University of New Jersey

In partial fulfillment of the requirements

For the degree of Doctor of Philosophy

Graduate Program in Chemical and Biochemical Engineering

Written under the direction of

M. Silvina Tomassone

And approved by

_____

_____

_____

_____

New Brunswick, New Jersey

October, 2020

ABSTRACT OF THE DISSERTATION

GRAPHENE NANOSTRUCTURED MATERIALS:
SELF-ASSEMBLED STRUCTURES AND NANO-CARRIERS FOR ENERGY STORAGE AND AEROSPACE

by Kurt Bradley Smith

Dissertation Director:

M. Silvina Tomassone

In our lab graphene oxide membranes are manipulated into higher order structures. Hollow spherical shells (and other geometries) of graphene oxide are summoned into hierarchical assemblies with control over shell membrane thickness, shell size and composition of binding additives. Intact membranes with shell thickness less than 20 nm have been demonstrated. This allows simultaneous control of the composite's surface area, surface properties, and transport resistances as related to diffusion and convection. Utilizing graphene oxide and resorcinol-formaldehyde as the basis for these processes allows for well bonded, high strength, structures to be made from these compatible materials. The ultrahigh surface areas attainable through thermal reduction of these constituent materials opens the door to electrophysical applications, such as supercapacitors. The high electrical conductivity, flexibility, and resiliency inherent from these materials is useful for electrochemical applications, such as lithium ion batteries.

We have developed a technique to load the interior of these hollow graphene spheres with electrochemically active materials, such as silicon nanoparticles. These silicon nanoparticles/hollow graphene sphere composites holds great promise as anodes for high capacity lithium ion batteries and anodes for batteries based on sulfur cathode chemistry. The graphene membrane spheres are able to confine the electrochemically active silicon to prevent agglomeration which otherwise occurs during thermal reduction and cycling. We have developed a facile method of assembly, through which specific properties can be engineered into these higher order structures. This control is precisely what is required to engineer these graphene oxide and graphene based materials for maximum effectiveness in catalysis, fuel cells, electrophysical and electrochemical processes.

ACKNOWLEDGEMENTS

I am very thankful to everyone who has guided my journey at Rutgers University, notably my thesis advisor and committee: M. Silvina Tomassone, Henrik Pedersen, Nina Shapley, and Thomas Emge. I have shared experiences and conversations with Henrik, Nina, and Tom, which I will never forget; you are all more than just a thesis committee to me. There are a lot of fond memories, and you have all influenced me for the better.

I would like to thank my research advisor for sticking with me and the development of this dissertation over the years; such loyalty is greatly appreciated.

I would particularly like to thank Silvina for direction on how to write with clarity, though by comparison, I am still the student in this regard. I was fortunate to find an advisor who would work with me in pursuing a patent - which has now made its's way, from a Provisional Application, to an International Application, and now to national applications, one of which has already been issued. That is not just very unusual, but extremely unusual for a student to hold a patent, and I have my advisor to thank for making this happen. Thank you Silvina!

Of all the people at Rutgers, I would most like to thank Jennifer (Jen) Sherri Winkler, for being a constant source of encouragement. Thanks Jen!

I would like to thank Thomas J. Emge for his expert help with XRD and his kind help in explaining many technical details. Many thanks to Valentin Starovoytov for his assistance with SEM and TEM imaging over many years. Sang-Wook Cheong and Xueyun (Evan) Wang were willing to help me with AFM imaging, simply because I needed their help and they thought the materials were interesting; this was very much appreciated. Many thanks to John Landers who always was interested in my research progress and always had time to discuss research ideas.

I would like to thank the many research group members, research assistants, and fellow students who provided much appreciated camaraderie: Pavithra Valliappan, Francis S. Romanski, Savitha Panikar, Felix Femilman, Kristin Steeley, Emanuel V. Scoullos, Jonathan Gerszberg, Franklin Bettencourt, Michael Tomasini, Ian Dill, Yangyang Shen, and many others who might be absent from this list, but are not absent from many fond memories. (My heart goes out to Yangyang and her family.) I would particularly like to thank Felix for the excellent work and ideas he provided to our research. Michael Clark made for many interesting and fertile discussions, without which my experience at Rutgers would have been less intellectually rich.

It would be incomplete to not to acknowledge the positive and much appreciated influence of the many professors, research collaborators, and fellow students which have come before Rutgers, in particular, those I meet at Northwestern University. This was an experience which had a profound impact on my respect for research goals. I will not forget how enthusiastically, Harold, Mayfair, and the entire Kung

lab, explored new ideas, sought truth, and never made me feel alienated in their endeavors. Jung Kyoo Lee was a true mentor and his dedication to research and selfless guidance has ever since changed me. I would like to thank Cary Hayner for his very much appreciated dedication to our research, and Chris Downing for always having answers to my various and sundry chemistry questions, as well as the many other members of the lab which made the experience very delightful. And finally, all the students and friends with whom I shared the broader academic experience: Chris Wilmer, Kate Bjorkman, Doris Grillo, Andrew Korinda, Denise Ford, Hui Deng, Ryan Boehler, and so many more far too numerous to list here.

I would also like to thank Lori Bocchino, Michael Stoll, David Hill, Chang Yul Cha, David A. Bell, and Linda Broadbelt, for their help in my career and academically.

I wish to express my love and gratitude to my brother Wade Smith, not only for being an amazing brother, but also for help with electronics questions that I have had during my research. Finally, I would like to thank my parents Robert and Eleanor Smith which not only made this dissertation possible, but made me possible as well.

To my parents Robert and Eleanor Smith and my brother Wade Smith.

TABLE OF CONTENTS

TABLE OF FIGURES

CHAPTER 1

PART OF THE DATA IN THIS CHAPTER HAS BEEN PUBLISHED:

Smith, K. B. & Tomassone, M. S. Ultrathin Hollow Graphene Oxide Membranes for Use as Nanoparticle Carriers. *Langmuir* **33**, 3765-3775, doi:10.1021/acs.langmuir.6b04583 (2017).

INTRODUCTION

In recent years graphene (G) and graphene oxide (GO) have been the focus of an intense research effort to exploit the unique properties of these materials [1-5]. It was only relatively recently that graphene was described in the literature as the first 2-dimensional material, physically isolated as individual sheets [6,7]. Likewise, graphene oxide was subsequently understood to be molecularly thin, two-dimensional sheets of remarkably high aspect ratio, which might be chemically reduced to graphene or modified to other 2-dimensional materials [8-11]. While GO itself is not a new material, the discovery of graphene and the realization of the true nature of GO at the molecular level, has prompted a continuous stream of research efforts to exploit the properties of this material such as for example the use of GO as a stabilizer for emulsions due to its amphiphilic nature [12-15]

Despite the great interest in the synthesis of hollow graphene oxide scaffolds[14-19], the research in this area is relatively in its infancy with respect to the more investigated area of solid graphene based materials. This dissertation is centered around the development of a new synthesis platform for the production of hollow core/shell particles or membranes of GO at the micro, and sub-micron scale with

thin (~3 to 25 nm) GO membranes with an O/W technique to use *as nanoparticle carriers* and then utilize these hollow particles for the creation of anodes for lithium ion batteries and foams. As an example of such carriers, sub-micron polytetrafluoroethylene (PTFE) particles and silicon nanoparticles are incorporated into the oil phase (naphthalene), before particle formation to form core/shell particles. We investigate the effect of the shear rate and concentration ratios on membrane thickness and particle size. Such particles have potential for use in drug delivery and energy applications, such as in lithium ion batteries.

The specific aims of this thesis are the following:

AIM 1: To develop a platform technology for the production of graphene oxide hollow membrane particles. As a platform technology we intend to build upon these techniques to develop a host of useful products with HGOM as the basis for Aims 2 and 3.

AIM 2: To develop the technology to interface graphene with other materials (Silicon) at the microscopic level through directed self-assembly and focus on a case study: the creation of Silicon-Graphene Based Anodes for Lithium Ion Batteries.

AIM 3: To develop Hollow Graphene Oxide Membranes (HGOM) reinforced cryogel foam composites utilizing the platform developed in Aim 1 in combination with conventional materials.

Chapter 2

Ultra-Thin Hollow Graphene Oxide Membranes for use as Nanoparticle-Carriers.

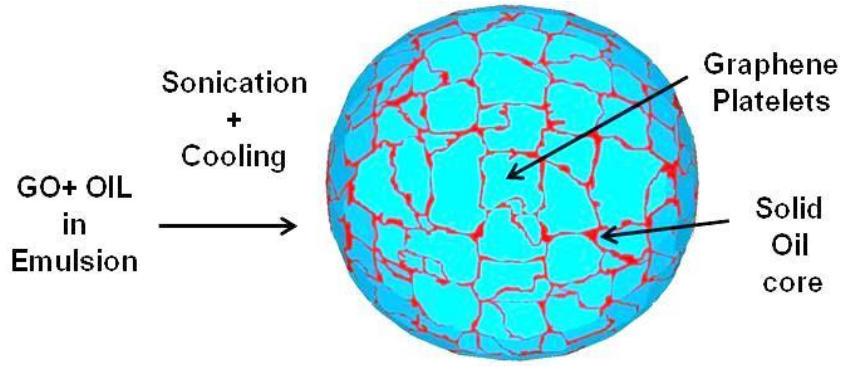

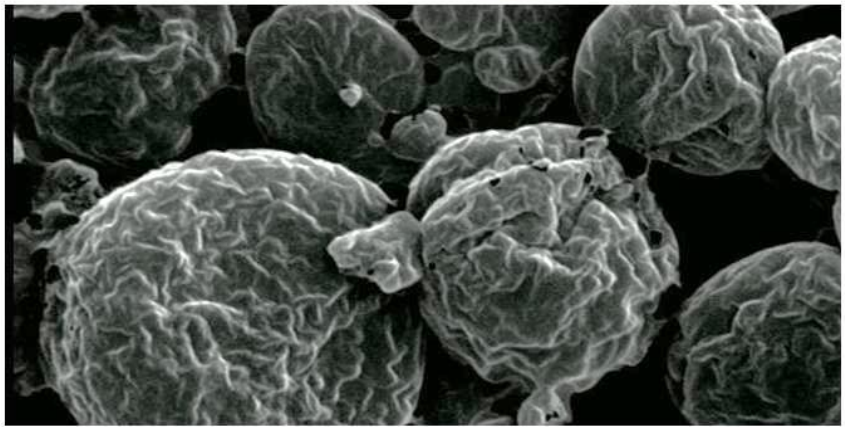

CHAPTER 2: ULTRA-THIN HOLLOW GRAPHENE OXIDE MEMBRANES FOR USE AS NANOPARTICLE-CARRIERS.

Part of the data in this chapter has been published:

Smith, K. B. & Tomassone, M. S. Ultrathin Hollow Graphene Oxide Membranes for Use as Nanoparticle Carriers. Langmuir 33, 3765-3775, doi:10.1021/acs.langmuir.6b04583 (2017).

International Patent (Patent Cooperation Treaty) Application Number: PCT/US2017/035208, **publication number WO2017210289A1**, published 2017-12-07 (Applicant: RUTGERS, THE STATE UNIVERSITY OF NEW JERSEY [US]. Inventors: TOMASSONE, Maria, S., and SMITH, Kurt, B.). Also part of the data in this chapter has been published (all with named inventors as TOMASSONE, Maria, S., and SMITH, Kurt, B.) in **publication number CN109562933** (China [PRC] – from application number CN201780045866.6A) and in **publication number US20190326592** (United States – from applications US201662343480P and US62/343,480).

SPECIFIC AIMS:

AIM 1: To develop a platform technology for the production of graphene oxide hollow membrane particles.

As a platform technology we intend to build upon these techniques to develop a host of useful products with HGOM as the basis for Aims 2 and 3.

ABSTRACT

We synthesize hollow spherical particles/membrane sacks of graphene oxide loaded with nanoparticles to be used as nanoparticles carriers, through a new method based on emulsion precipitation and sublimation of the cores. We vary the synthesis parameters, such as shear rate, pH and graphene oxide and oil concentration ratios. Our results show a concentration dependent membrane thickness that varies

between 3 and 25 nm depending on the concentration, and their mean diameters vary between 500 nm and 70 μm. In addition polymeric nanoparticles are loaded inside the graphene oxide shells forming core-shell particles demonstrating that they can be used as carriers for nanoparticles. Our particles are characterized via laser diffraction, zeta potential, FE-SEM, TEM, BET, and AFM. Potential applications of this work include applications that benefit from core-shell structures and nanoparticle-carriers, including drug formulation, catalysis, and electrochemical applications.

1. INTRODUCTION

There has been a lot interest in the synthesis of hollow graphene oxide scaffolds[14-19], however the research in this area has large room for improvement. For example, Guo et al have worked on "free standing" structures (hollow particles), where the graphene oxide layer was very thick (of the order of a hundred or a few hundreds of nanometers)' thus forming relatively thick walled particles [16] using Water in Oil (W/O) technique. Their work focused more on the effects of the preparation parameters on the morphology of the particles and on the effect of the oxidation time in the formation of GO. Later, Kung et al reported structures of graphene oxide as nanoparticle sacks but these were crumpled structures made with a completely different technique, spray drying, in which an aqueous suspension of graphene oxide was nebulized to form aerosol droplets which were passed through a tube furnace [17]. The work by Zetterlund et al focused on the synthesis of hollow, cross-linked polymeric particles that have an "armor" of graphene oxide in their shells[14]. Their work concentrated on the study of the influence of the monomers and cross-linkers. They also reported loading hydrophobized titania nanoparticles into a hollow GO particle[15]. Etmimi and Sanderson also reported the use of GO as a surfactant in miniemulsion polymerization,[18] and the work of Pentzer has recently been used to make free-standing (cross-linked) GO hollow particles[19]. Very recently, Guan, Wen and Lou have also synthesized hollow structures made out of F127-polydopamine

composite micelles on diverse functional materials but the graphene oxide was encapsulated inside these particles rather than being the material forming the shell [20,21]. Buchold et al have done work on the synthesis of AlO(OH) hollow spheres via a W/O micro-emulsion [22]. However, their method was complicated and time consuming and they did not work with GO. None of these studies have focused on the preparation of GO hollow spheres through assembly of GO using an Oil in Water (O/W) emulsion technique up to now and/or done a systematic investigation of the factors that control membrane thickness and particle size. In addition none of these works have focused on the implementation of GO hollow particles as nanoparticles carriers despite the great amount of papers focused on the utilization of graphene and graphene oxide for the treatment of disease, including, drug delivery, imaging, and theranostics[23-25]. To the best of our knowledge none of the aforementioned works have created these types of hollow GO loaded particles.

---

2. MATERIALS AND METHODS

2.1 Summary of the Materials. Graphene stabilized oil in water emulsions were produced using naphthalene, 9-flourenone, paraffin wax (m.p. 70-80 C), acetic acid, and polytetrafluoroethylene particles, which were purchased from Sigma Aldrich, and used as received. No surfactants, other than the graphene oxide were added to form the emulsions. The glassware and all experimental components were thoroughly washed with acetone and DDI water prior to use. Ultrapure

Milli-Q water produced from the Millipore system, was used as the water source throughout, including the purification of GO, and as the source of water for the emulsions, as well as the final rinse water for all glassware and equipment.

Graphene oxide was synthesized by a modified Hummers method using natural flake graphite (grade 230U), donated by Asbury Carbons, Asbury, NJ. The mean particle size of the graphite was 18 μm. The modified Hummers method consists of an acidic pretreatment followed by the Hummers method as developed by Kovtyukhova and others[26]. The Hummers Method is an oxidation process used to produce graphene oxide by combining graphite and a solution of concentrated sulfuric acid and potassium permanganate ($KMnO_4$). The acidic pretreatment involves the addition of 10 g $K_2S_2O_8$ and 10 g P_2O_5 to 30 mL H_2SO_4, then 20 g of graphite must be added and the mixture must be heated in an oil bath at 80°C for 6 hours, followed by cooling and diluting in DDI. In our experiments, the preoxidized graphite was filtered and washed with DDI water and allowed to air dry overnight. The oxidation step was achieved by the very slow addition of 60 g $KMnO_4$, to the preoxidized graphite and 460 mL H_2SO_4 in an ice bath. Great care was taken to keep the temperature of the mixture below 20°C during the addition of $KMnO_4$, since this step is exothermic. Once the $KMnO_4$ was dissolved the mixture was heated to 35°C for 2 hours, producing a dark green paste. The mixture was cooled and diluted very slowly with 960 mL DDI, keeping the temperature below 50°C (the color of the mixture changes from purple to brown grey). The mixture was stirred for 2 hours and further diluted with 2800 mL of

DDI followed by the addition of 50 mL of 30% H_2O_2, which results in a brilliant yellow mixture. The supernatant was decanted, and the graphene oxide was washed with 5000 mL 10% HCL. The GO was further purified by washing (via centrifuging at 14,000 rpm) an additional 10 times with DDI water. The graphene oxide was stored in the dark in solution. Prior to use in making HGOMs with the rotor-stator, the GO was sonicated for 30 minutes in a polypropylene bottle placed directly into a VWR Ultrsonic Cleaner model 97043-964 (240W, 35kHz). Prior to use in making HGOMs with the sonicator, the GO was sonicated in a glass vial with a Misonix S3000 probe sonicator at a power setting of 4.5. The vial was periodically removed and cooled, for a total sonication time of 15 minutes.

2.2 Methodology.

2.2.1. Synthesis of Hollow Graphene Oxide Membranes on Naphthalene Cores. Hollow graphene oxide membrane (HGOM) particles were obtained using an oil in water (O/W) emulsion. The water phase was created as follows: In a covered 150 mL beaker, 10 g of 0.65 wt% GO aqueous solution and 71 mL of DDI water are mixed. The oil phase: 10 grams of naphthalene (m.p. 80°C) were added to the water phase and heated in a boiling water bath, all the contents of which were also covered to provide even heating and limited evaporation of the bath. The beaker contents were brought to near boiling point (approx. 98^{o}C) in 5 minutes. The beaker was then uncovered and an IKA T25 digital Ultra Turrax rotor-stator homogenizer with S 25N-25T dispersing tool (preheated in boiling water) was inserted in the beaker

and the contents were emulsified at 20,000 rpm for 3 minutes. The rotating tip of the rotor-stator disperser has a high speed rotor and a closely spaced stationary element which is particularly effective at producing high shear rates, and thus fine emulsions. After the first minute of emulsification, 8.6 mL (9.0 g) of glacial acetic acid was slowly added to the beaker, over about 30 seconds. This produced a mixture, in this case, of 650 ppm GO by weight of the total mixture. The aqueous phase of this mixture was 10.0 wt% acetic acid. The oil to total emulsion ratio was 10 wt% for this formulation. The temperature remained near boiling (approx. 98^{o}C) throughout the emulsification process. This process produced micron-scale droplets of the liquid oil phase (naphthalene) which were coated in multiple layers of graphene oxide forming a GO membrane around the oil droplets. After a total of three minutes of rotor-stator stirring, the beaker was removed from the water bath and cooled to room temperature by placing the beaker in a room temperature water bath. As the temperature was brought below the melting point of the oil-phase, the naphthalene droplets solidified, forming a suspension. The experimental steps are shown in Figure 1. A suspension of solid particles was formed after cooling. Figure 1 shows the experimental procedure for the emulsion-precipitation method of creating membrane coated solidified organic particles covered with graphene oxide membranes. After sublimation of the solid oil phase cores, hollow particles were formed. These low density, hollow particles with very thin shells can be seen in the SEM images in Figure 2. These spherical particles and those of other geometries belong to a new class of Hollow Graphene Oxide Membrane particles, with free standing ultra-thin shells. We systematically varied the concentration of the GO

(which changes the GO to naphthalene ratio) and the rotor-stator speed.

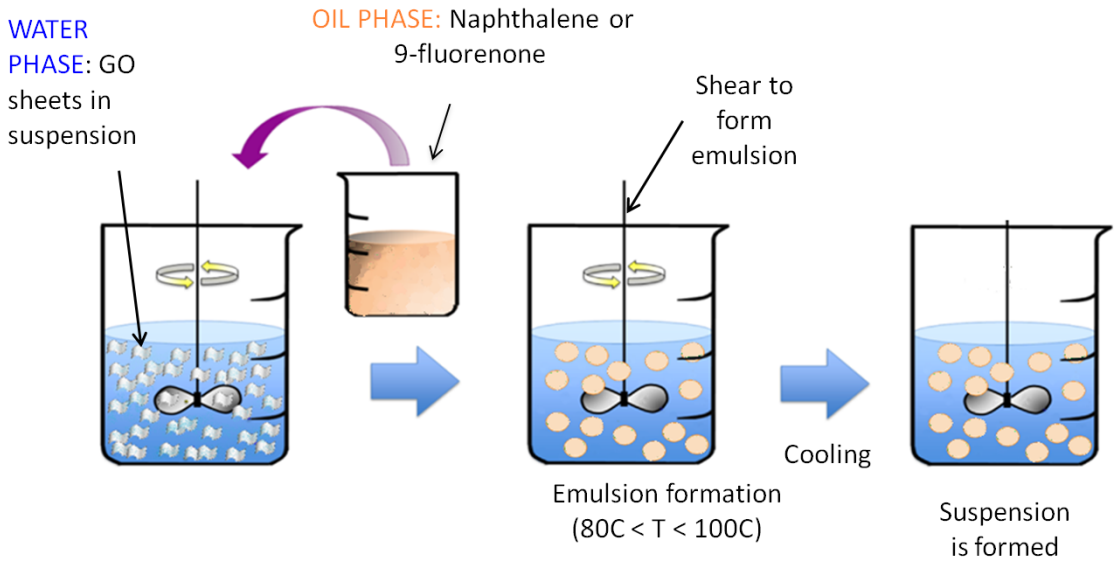

Figure 1: Experimental procedure for the emulsion-precipitation method of creating membrane coated solidified organic particles covered with graphene oxide membranes.

The HGOM particle size was measured by laser diffraction to characterize the particle size created under these conditions. We developed a robust and reliable process and materials parameter space which allows for the control of the properties of the HGOMs produced, including the particle diameter, the thickness of the membranes and the loading materials.

2.2.2. Synthesis of HGOM by Sonication. Hollow graphene oxide membrane particles were also made by sonication using with a Misonix S3000 probe sonicator with a 418 MICROTIP. A total volume of 15 mL of the oil phase (naphthalene) plus water phase (acidified aqueous solutions of GO) were added

to a 20 mL glass vial and sonicated at a power level (25 W) sufficient to heat the sample to near the boiling point (98^{o}C).

2.2.3. Synthesis of loaded HGOM Nanocarriers/Core-Shell Particles. It is possible to load the interior of these HGOMs and create core shell particles uploaded with an active material or with polymers. Core-Shell particles have unique properties which make them valuable in many fields including energy storage applications and medicine. The process can easily be manipulated to incorporate any type of nanoparticle loads, such as polymers, or electrochemically active materials such as silicon nanoparticles. As a case study we first loaded our HGOM particles with polytetrafluoroethylene (PTFE) (teflon). The procedure is as follows: PTFE nanoparticles were added to liquid naphthalene, and subsequently the GO aqueous phase was added to the vial and mixed together. Finally, the mixture was sonicated with the method described above. By incorporating hydrophobic nanoparticles to the oil phase (i.e. naphthalene) the nanoparticles retained inside the graphene oxide membrane shells, creating core-shell particles (PTFE-HGOM). We also followed a similar procedure to load the HGOM with silicon nanoparticles. The void space within any type of core-shell particle (X-HGOMs) generated after sublimation of the core can be controlled by varying the oil to nanoparticle ratio. Larger ratios of oil to nanoparticle produced higher fractions of void space. The probe sonicator produced a much higher concentration of power than the rotor-stator homogenizer, thus X-HGOM particles with mean diameters as small as 500 nm can be produced. These nanoparticle carriers are

promising candidates for a number of applications, included silicon nanoparticles, which we are actively exploring for lithium ion batteries, and polymer particles, which have potential biomedical applications as composite drug delivery agents. HGOM core-shell particles for use in lithium ion batteries is the subject of Chapter 3 of this dissertation.

2.3 Characterization.

Transmission electron microscope (TEM) images were obtained using a Jeol JEM-100CX II, using copper grids. After sample preparation both SEM and TEM samples were dried and then held at 60 °C in a double walled beaker overnight to ensure all of the naphthalene was sublimed. Scanning electron microscope (SEM) images were acquired using the Amray 1830 I scanning electron microscope. SEM sample stubs were prepared by applying liquid suspensions to a mounted silicon wafer with a pipette. SEM samples were allowed to dry and were then vacuum desiccated and sputter coated, using a Balzers SCD 004 Sputter Coating Unit with Gold/Palladium Target (Au:Pd 60/40 ratio), prior to imaging. Additional SEM images were obtained using a Zeiss Sigma Field Emission SEM. Particle size analysis was performed using a Beckman-Coulter LS-13 320 laser diffraction apparatus with a universal liquid module filled with distilled deionized water. A refractive index of 1.582 was used to define the naphthalene cored particles. All particle size measurements were completed on the suspensions at room temperature. The zeta potential of suspensions was measured using photon

correlation spectroscopy using a Malvern Zetasizer Nano Z90 and disposable folded capillary cells. Characterization of the exfoliation of the GO sheets was performed using atomic force microscopy. AFM images were acquired with a Nanoscope IIIA (Vecco) in air in tapping mode. AFM samples were prepared by placing a drop of the dilute synthesized graphene oxide solution onto freshly cleaved mica and immediately drying under flowing argon. Graphene oxide sheet size analysis was conducted with the aid of the computer program, "Image J", to calculate the area and equivalent diameter of each graphene oxide sheet from SEM images. These results were then used to estimate the average size of the GO sheets by using the Sauter mean diameter (d_{32})[27] as well as to produce bar graphs showing the surface area as a function of the graphene oxide lateral sheet size.

The pH of solutions and suspensions was measured using a double junction Oakton phTester 20 after three point calibration using NIST standards.

BET (Brunauer–Emmett–Teller) surface area measurements were obtained with a Quantachrome Autosorb 1 Gas Sorption Analyzer using nitrogen as the adsorbate with a bath temperature of 77 K. Samples for BET analysis were held at 60 °C in a double walled beaker for one day (prior to outgassing) to ensure all of the naphthalene was sublimed. The sample was outgassed under nitrogen at 150 °C for 7 hrs. Results of the BET analysis indicate a surface area of 67.2 m^2/g for the HGOM made at a rotor-stator speed of 20,000 rpm and 2600 ppm GO.

3. RESULTS AND DISCUSSION.

Graphene oxide membranes were templated in an oil in water (O/W) emulsion, allowed to cool forming particles with solid oil phase cores coated with a thin GO membrane spontaneously formed at the oil/water interface. Sublimation of the core material resulted in thin Hollow Graphene Oxide Membrane particles (HGOMs). The method used to form HGOM particles and the modified method to form core-shell particles with graphene oxide membranes are described in detail in Section 2.2.

3.1 Hollow Graphene Oxide Membrane Particles. Core Materials: HGOMs were templated on different core (oil phase) materials: naphthalene, 9-fluorenone and paraffin wax. Naphthalene, which easily sublimes, readily formed three dimensional free standing hollow structures as can be seen in the SEM images of Figure 2.

The naphthalene was allowed to sublime from the sample prior to imaging. Figures 2 A and B show SEM images with needle-shaped particles made out of 9-fluorenone stabilized by graphene oxide. After sublimation particles still looked needle-like. In Figure 2C we can observe an SEM image of HGOM particles with a paraffin wax core that has not been removed. A way of removing the paraffin core is melting it with heat, but when heat is applied to the wax and the wax melts and transitions into a liquid phase, it increases its surface tension significantly.

This surface tension force may be enough to disrupt the structure of the thin graphene oxide membranes, so we did not attempt to remove the wax core. However, the purpose of showing these particles is to demonstrate the synthesis of stable graphene oxide structures with a core that may be used for other applications.

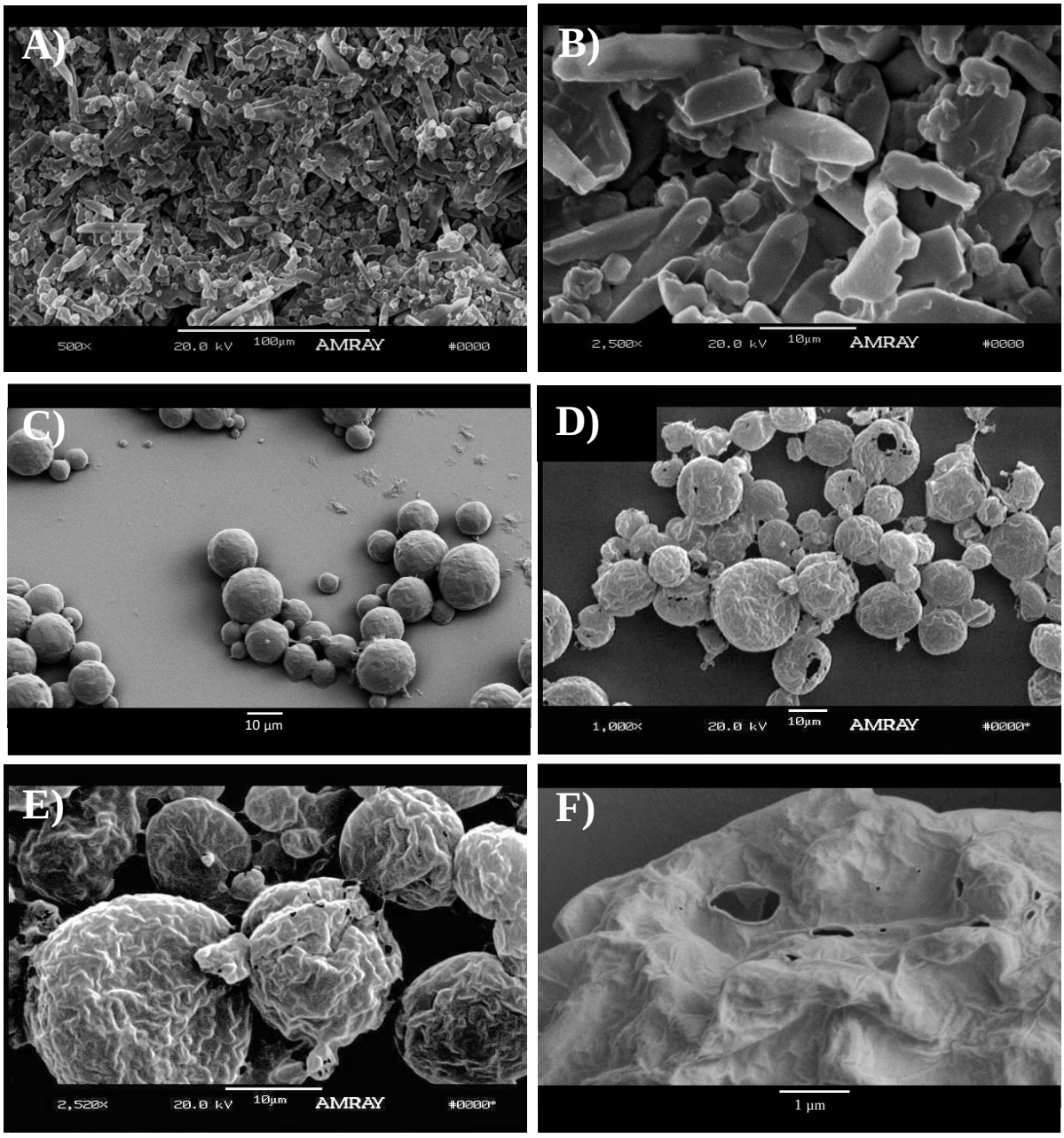

Figure 2 A and B) SEM images show needles of 9-fluorenone stabilized by graphene oxide. After sublimation particles still look needle like. C) SEM image of paraffin wax stabilized by graphene oxide. D- E) The SEM images shows hollow graphene oxide spheres which were templated by this method in which the core material (naphthalene) was subsequently removed through sublimation leaving behind only the shell of graphene oxide. F) SEM image reveals small hole showing the hollow nature of these very thin GO membranes. The thicker shells in the TEM images of Figure 3B appear to be without such holes. Scale bars for images A, B, C, D, E and F are 100 µm, 10 µm, 10 µm, 10 µm, 10 µm and 1 µm, respectively.

Figures 2 D-F, are SEM images of hollow graphene oxide spheres, which were templated by this method in which the core material (naphthalene) was subsequently removed through sublimation leaving behind only the shell of graphene oxide. Lastly, in Figure 2F we can see some SEM images revealing small holes showing the hollow nature of the HGOM particles.

Transmission Electron Microscopy (TEM) images are seen in Figure 3 A, B and C, which shows a 'thin' walled HGOM after sublimation of naphthalene from a suspension formed at 20,000 rpm 10% acetic acid and 325 ppm GO (See Figures 3 A and B). In Figure 3C, we can see that the apparent wall thickness was approximately 4 nm. Figures 3 D, E and F show HGOMs, which were made at 20,000 rpm, 10% acetic acid, with 2600 ppm GO .

Figure 4A shows an AFM image of the exfoliated individual GO sheets, with lateral dimensions approximately 400 nm to 1 micron in size. Figure 4B shows the cross sectional height analysis depicting an individual sheet thickness of approximately 1.1 nm, with little apparent stacking of additional sheets.

It is important to comment on the size of the GO sheets used in our experiments. Previous work has found that GO sheets have size dependent amphiphilicity [12,28]. The reason for this is because GO sheets tend to have carboxylic acid groups in the edges, so the smaller the length, the more edges they have and the more hydrophilic the GO sheets become.

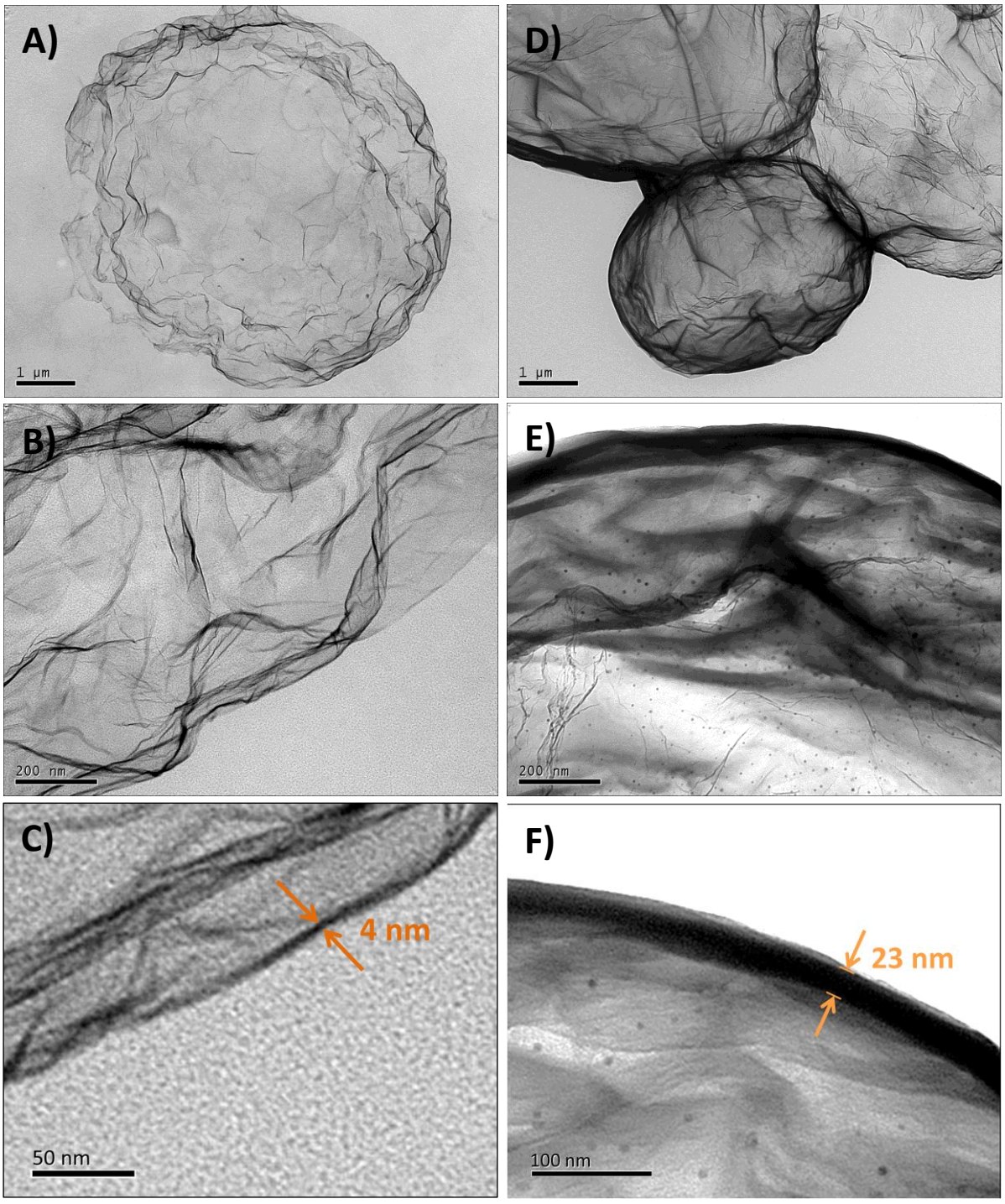

Figure 3: Figures A, B and C show TEM images are of a 'thin' walled HGOM from a suspension formed at 20 krpm 10% acetic acid and 325 ppm GO. In image C, the

apparent wall thickness is about 4 nm. D, E and F show HGOMs which were made at 20 krpm, 10% acetic acid, with 2600ppm GO. The average calculated wall thickness for these HGOMs is 17 nm.

In order to have the GO sheets attract to each other, that situation is not favorable because it affects the stacking and plating of the sheets. By increasing the sheet size, the sheets become larger in length and therefore the number of edges per unit area decreases, and hence, the hydrophilic groups decrease so the sheets become more hydrophobic and attract to each other forming thicker membranes (plating). It was found that larger GO sheets float on an aqueous surface while smaller ones sink due to their increased hydrophilicity[12].

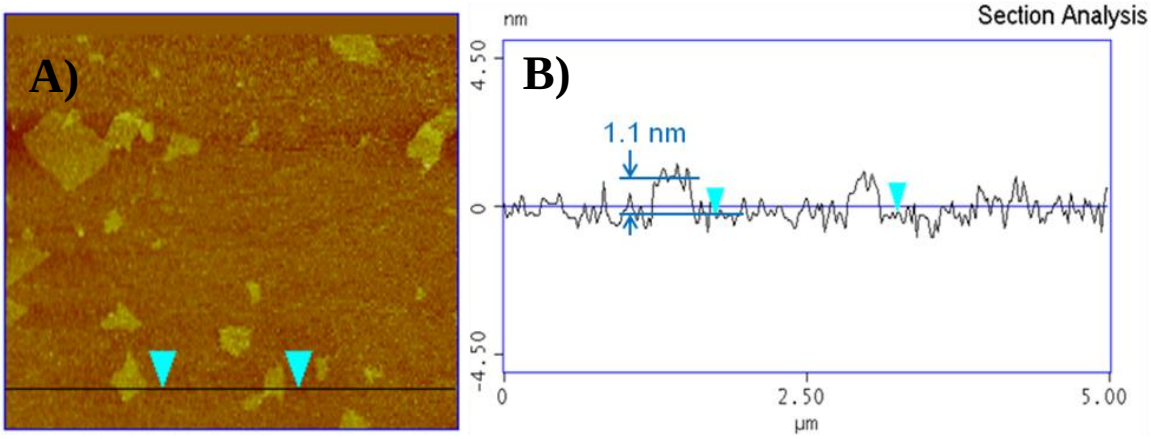

Figure 4: AFM images indicate the GO is single layer. A) The individual sheets can be seen in the AFM image, with increasing height appearing lighter or more yellow than the cleaved mica background which was used as a support for the GO sheets. B) In the sectional analysis, the surface height is graphically represented as a cross section across the sample. The triangles (blue) represent the same location in the image and sectional analysis. The height of the GO sheets is 1.1 nm, or one layer of GO.

In our work we used a range of GO sheet sizes. To synthesize our larger HGOM particles (as described in section 2.2.1.) we used larger graphene oxide sheets of approximately 4µm obtained with a bath sonication method and to synthesize the smaller micron sized HGOM particles, we used smaller GO sheets of the order of 0.52 µm obtained with a higher power probe sonication method. Figures 5A and C depict SEM images showing the size distribution of the GO sheets and Figs. 5B and 5D show bar graphs of the surface area vs. lateral size of the GO sheets. Some stacking or partial overlap of the sheets can be observed in the SEM images, at the graphene oxide concentrations used in these samples.

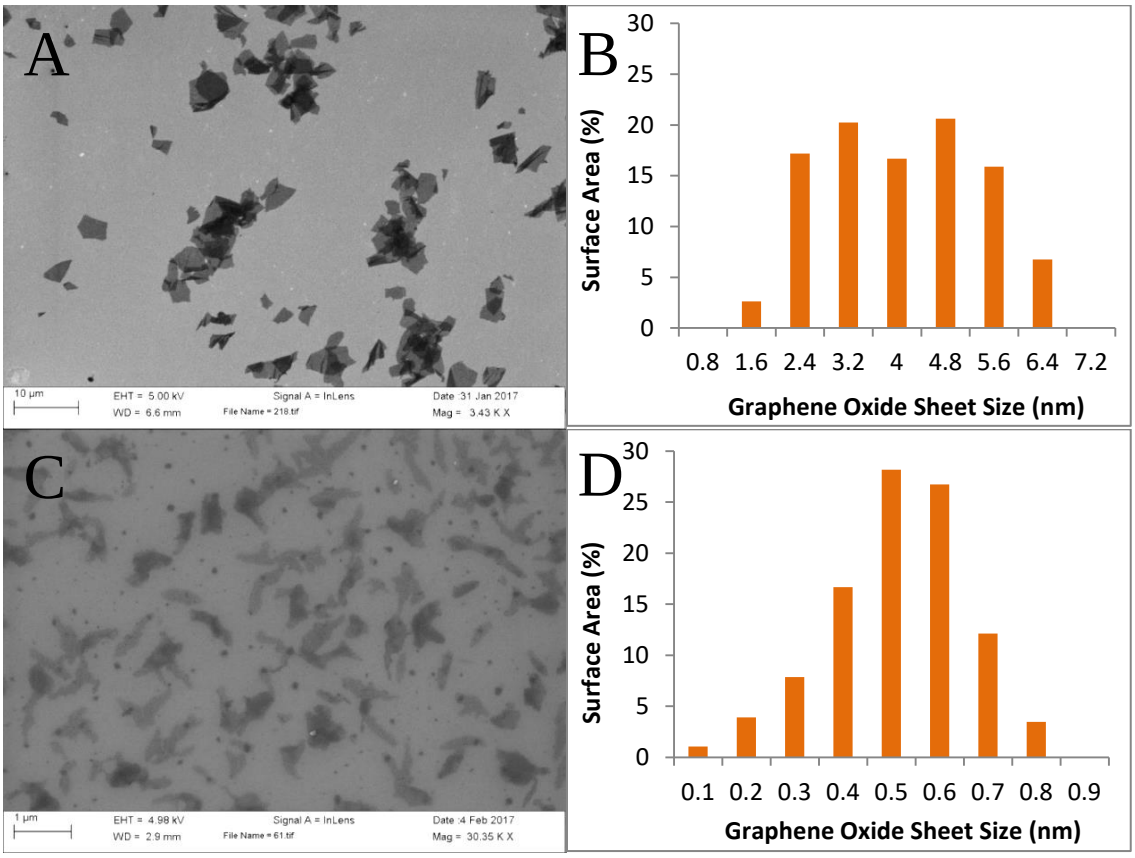

Figure 5: A) The GO sheets used to make HGOM by rotor-stator are of the order of a few microns in lateral size as seen in the SEM images. B) Histogram of the size of the exfoliated GO sheets used to make the HGOM by rotor-stator. The lateral surface area based mean size is 4.0 μm. C) The SEM images of the exfoliated GO sheets used to make HGOM through sonication are sub-micron in size. D) Histogram of surface area based mean size (laterally) of the exfoliated GO used to make HGOM through probe sonication as evaluated by analysis of the SEM images. The surface area based mean size (laterally) is 0.52 μm.

While sheet size is an important factor, especially in stabilizing particles, in our work extremely small sheet sizes are counterproductive, as extremely small sheets can become very hydrophilic [12]. In our experiments we varied the shear rates from 5,000 to 20,000 rpm with a rotor-stator and also systematically varied the concentration of the GO but we kept the naphthalene concentration and aqueous phase (water and acetic acid) concentration constant. Samples were prepared in duplicate and these results are shown in Figure 6. Figure 6A shows the diameter and the membrane thickness of the templated HGOM particles as a function of GO concentration at a fixed rotor-stator speed of 20,000 rpm. The diameter of the HGOM decreased as additional GO was added. This is expected due to the stabilizing amphiphilic nature of GO explained later in this section. At high GO concentrations (above 650 ppm) the HGOM particle diameter became nearly constant reaching a plateau for sizes of the order of 6-8 μm. The membrane thickness increased in what appears to be a nearly linearly trend with

increasing GO concentrations. Stable emulsions could not be produced below a GO concentration of approximately 40 ppm, producing a naphthalene to GO weight ratio of approximately 2500:1. At this limit the membrane thickness was approximately 3 nm. In Figure 6B we observe the same trends for a lower rotor-stator speed of 5,000 rpm. In both figures 6A and B, we observe a HGOM particle diameter plateau reached with increasing GO concentrations above 500 ppm. The diameter formed a plateau at approximately 16 μm for 5000 rpm. The lower limit of stable emulsions was again approximately 40 ppm GO, and this concentration produced membranes, which were also approximately the same minimum thickness of 3 nm.

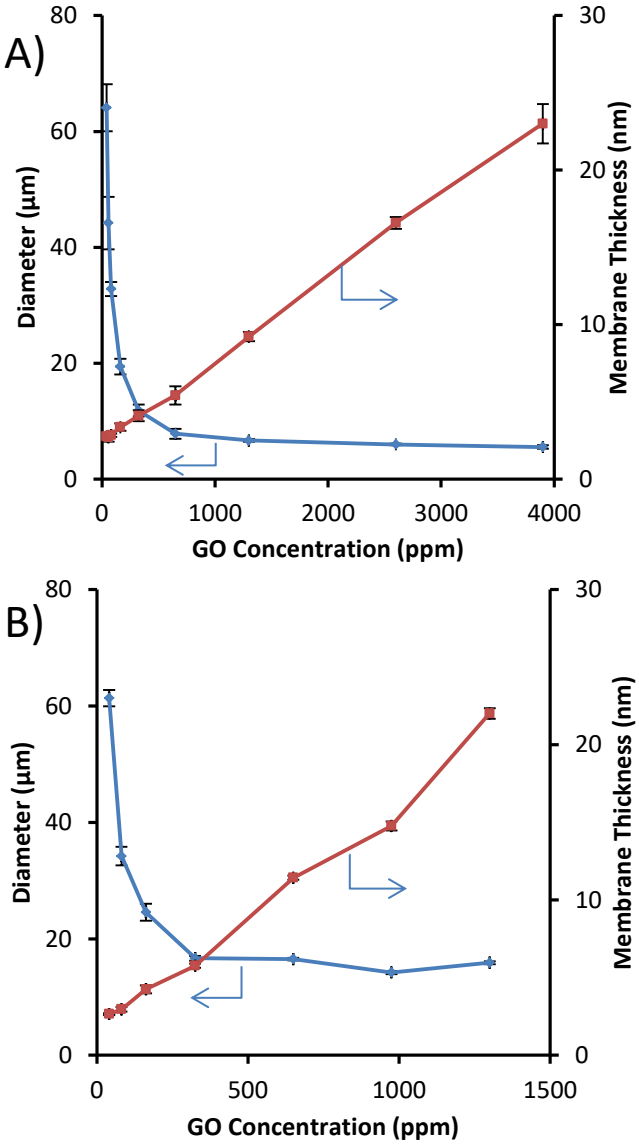
A)
Diameter (µm)
Membrane Thickness (nm)
GO Concentration (ppm)
0
20
40
60
80
0
10
20
30
0
1000
2000
3000
4000
B)
Diameter (µm)
Membrane Thickness (nm)
GO Concentration (ppm)
0
20
40
60
80
0
10
20
30
0
500
1000
1500

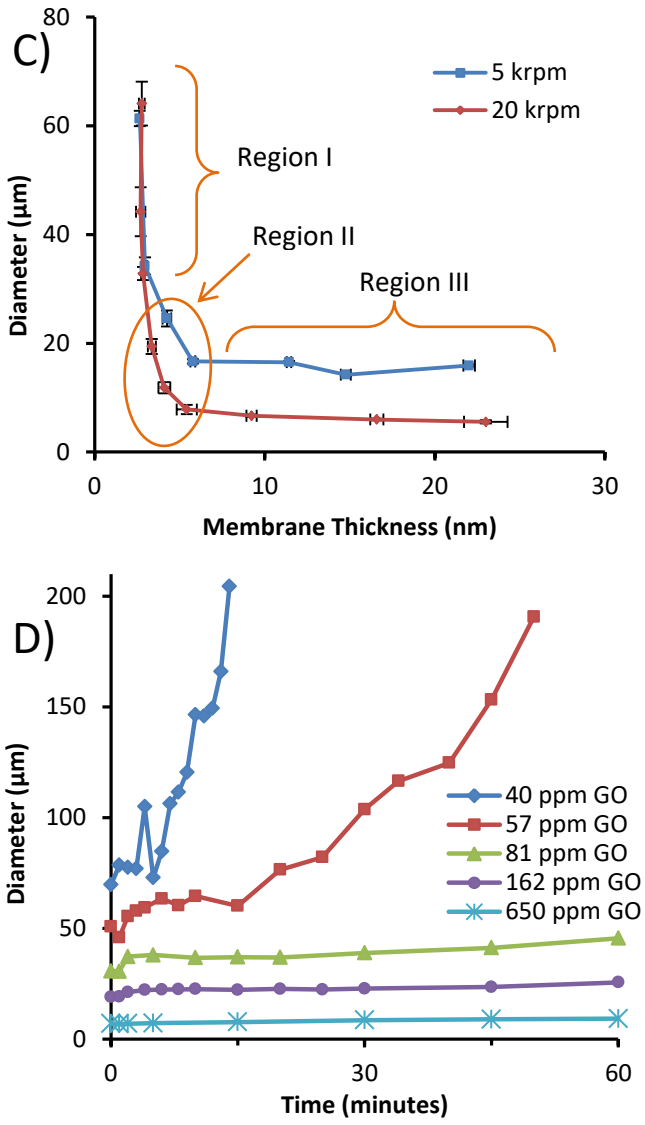

Figure 6 Plots of mean size using particle surface area based distribution, and calculated mean membrane thickness based on mass balance formed at various GO concentrations. The standard error is shown. A) HGOM formed by rotor-stator at 20,000 rpm, and B) at 5,000 rpm. C) Plot of the HGOM diameter to membrane thickness at two different rotor-stator speeds. D) Plot of the diameter of the hot emulsion droplets as a function of time at various GO concentrations.

A very interesting trend was observed when the resulting properties were mapped onto a plot as shown in Figure 6C for two different rotor-stator rates measured in revolutions per minute (rpm), one curve for 5000 rpm (in blue) and another for 20,000 rpm (in red). Using the relationship between membrane thickness and diameter, we could distinguish three regions. At sufficiently low GO concentrations, the membrane thickness was constant and at sufficiently high GO concentrations, the diameter was constant. In particular in this figure we observe that at 20,000 rpm (red curve), there are three distinctive regions: Region I (40 to 325 ppm), Region II (325 to 1300 ppm), and Region III (1300 to 3900 ppm). Region I consists of particles with nearly constant GO membrane thickness and varying particle diameter. Increasing the GO concentration by 300% (from 40 to 162 ppm) results in an increase of 21% in membrane thickness (from 2.9 nm to 3.5 nm). In region I we observe that for a membrane thickness of 3 nm there is only about 3 or 4 layers of GO (i.e. assuming an inter-layer spacing of 0.8 nm as typically reported by XRD for filtration formed GO membrane samples) [29]. This region is dominated by emulsion droplets coalescing, which is a thermodynamically favorable process. Region II consists of a transition region in which the GO concentration affects both membrane thickness and particle size. It occurs because not all droplets initially have enough GO to cover the entire surface of the particles and provide stability, and therefore some coalescing of the droplets occurs, providing diameters slightly larger than those of Region III, but membranes slightly thicker than in Region I. What is remarkable is that Region II occurs across a very narrow range of membrane thickness, between

approximately 3½ and 5½ nm. In Region III it is possible to observe that for a fixed rotor-stator speed (either 5000 rpm or 20,000 rpm), the resulting diameters are independent of the concentration used. In Region III the emulsion droplets are stabilized very soon after their formation. Region III consists of particles with constant diameter as the GO concentration is increased for a fixed shear rate. This is a region in which increasing the GO concentration does not appreciably change particle size but it does change membrane thickness. In this region increasing the GO concentration has almost a 1 to 1 ratio of increasing the membrane thickness. We can also observe that, at 20,000 rpm, increasing the GO concentration from 1300 ppm to 3900 ppm, (i.e. a 200% increase in concentration), resulted in only a slight reduction of approximately 17% in particle size, and a 150% increase in membrane thickness. A similar three region trend is observed at 5,000 rpm, but coarser emulsions were produced in Region III at these lower shear rates. Almost the exact same lower limit in membrane thickness was achieved in Region I for the two shear rates.

Figure 6D shows the particle diameter as a function of time for GO concentrations that go from 40 ppm up to 650 ppm. From 81 ppm up to 650 ppm the diameters of the particles remained quite stable as a function of time. However when the GO concentration was reduced to 57 ppm, the diameters of the particles showed a sharp increase as a function of time. For 40 ppm the emulsion stability lasted up to 8 to 10 minutes as seen in Figure 6D.

For these experiments, rather than immediately quenching the entire emulsion to form a suspension, the emulsions were kept at 98^{o}C for a prolonged period. Over the course of an hour, small samples were withdrawn and immediately quenched in a water bath at room temperature, effectively solidifying the droplets into particles allowing the stability of the emulsion to be measured. The particle (solidified droplets) size of each sample was then determined by laser diffraction. The size of the emulsion particles/droplets may increase, rapidly or hardly at all. We can see in Figure 6D that the stability of HGOM droplets in the emulsion became increasingly better for higher GO concentrations.

Since the oil phase core material solidifies upon cooling (which occurs rapidly for the small samples placed in a water bath), the suspension of solid particles was accurately measured later, over the course of hours. This allows for the measurements of the stability of the emulsion phase on a minute by minute basis without the need to conduct the particle size measurements on the same minute by minute time scale.

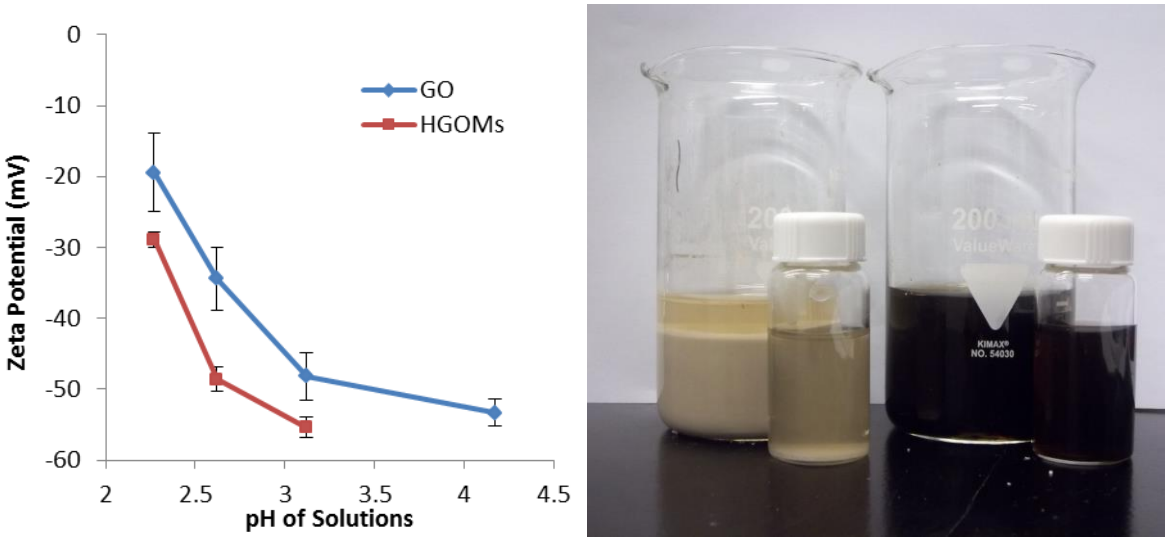

Figure 7: A) The zeta potential of both GO and HGOMs was measured at various pH conditions. The standard deviation of the measurements is shown. B) The left beaker is a HGOM suspension, which has partially settled revealing a layer of supernatant which is clear with very little remaining graphene oxides. The left vial also contains some of the decanted supernatant. The right beaker and right vial contains the same concentration of graphene oxide as used for the preparation of the HGOM. In the left beaker, virtually all of the graphene oxide has been plated as membranes onto the HGOM with solid oil-phase cores.

To understand the interaction of the GO at the surface of the oil droplets, and to more fully characterize the graphene oxide used throughout these experiments, the zeta potential was measured for the GO and HGOM suspensions at different pH conditions. Figure 7 shows the relationship of pH to zeta potential. The combination of favorable interaction between the GO platelets at the surface of

the oil phase, and reduced interaction with the water phase, greatly favors platelet stacking into thin membranes. This is in part accomplished by control of the zeta potential of the graphene oxide platelets. Acetic acid was added to create a series of GO solutions of decreasing pH. In Figure 7A it can be seen that decreasing the pH of the GO solutions produces ever decreasing net charge. The zeta potential of the HGOM particles in suspension was also measured. The zeta potential of the HGOM (red curve in Figure 7A) trends slightly more negative than the zeta potential for the GO solutions (blue curve in Figure 7A) for comparable pH conditions. We argue that the more negative (more highly charged) results for these particles (compared with the GO solutions at the same pH) is due to the preferentially stacking of the sheets on the HGOM particles, with more hydrophilic sheets being the last to stack upon the membrane.

It is interesting to notice that for a coarse emulsion with large HGOM particles, the particles would settle over the course of a few hours, in contrast to a finer emulsion which would take much longer time to settle. Figure 7B is a photograph depicting the separation of the precipitate from the supernatant in the left beaker. The left beaker was a HGOM suspension, which had partially settled revealing a layer of supernatant, which was clear with very little remaining graphene oxide. Notice that the supernatant was clear because all the grapheme oxide was covering the HGOM particles and it was not in solution. The transparent, nearly colorless, supernatant from the HGOM contained almost no GO. For comparison, the right beaker contained a dark solution of only GO at the same initial

concentration as used for the preparation of the HGOM before these particles are formed. Quantitative analysis by UV-vis spectroscopy indicated that the supernatant in the left beaker contained less than 10% of the original GO, with more than 90% on the suspension particles. Surprisingly, the HGOM could be washed on a filter with distilled water without release of the GO from the solid oil phase cores. We initially prepared emulsions without adjusting the pH, however, a significant portion of the GO was left in the supernatant (30-40 %). We then considered lowering the pH of the emulsions with acetic acid. By comparison, a sample with a lower pH, prepared with 10% acetic acid (such as the sample in the beaker shown in Figure 7B) had nearly all of the GO plated onto the Naphthalene particles and the supernatant appeared clear.

The reason why lowering the pH has a significant effect is because decreasing the pH removes the surface charge and decreases the hydrophilic nature of the GO sheets. According to the studies by Huang et al, [12] on the pH-dependence on amphiphilicity, GO sheets become more hydrophilic as the pH is increased, and conversely more hydrophobic when the pH is decreased. In our experiments, as depicted in Figure 1, we can visualize that GO membranes are essentially formed by the creation of oil droplets in an aqueous environment. The graphene oxide membranes cover the exterior of these droplets. Thus, by making the GO more hydrophobic, and hence lowering the pH, the GO sheets tend to be more attracted to the oil phase or stack to each other, minimizing the amount of GO that can migrate to the water phase.

Additionally, GO is composed of small 'solid' particles and it has the potential to act both as an amphiphilic emulsifier and as a stabilizer in a Pickering emulsion [12,13]. In a Pickering emulsion small solid particles adsorb at the interface between two non-miscible liquids. For particles with intermediate wettability of the two phases, there tends to be a large free energy of adsorption, which for some systems yield highly stable emulsions for which the adsorption of the particles at the surface is effectively irreversible [30]. This is in contrast to conventional amphiphilic small molecule surfactants, which partition in rapid equilibrium between the bulk phases and the interface.[31]

It should be noted that pH is not the only factor affecting the zeta potential and the ability of GO to not only form a Pickering emulsion, but also to stack into membranes. For example, DVLO (Derjaguin, Verwey, Landau and Overbeek) theory, predicts that changing the electric permittivity of the water phase by adding salt should promote coagulation of GO. Indeed, we found, adding NaCl (instead of acetic acid) assisted the formation of emulsions with naphthalene stabilized by GO. However, one advantage of using the acetic acid lies in the fact it can be removed through evaporation, thus facilitating the preparation of samples free of contaminants. Finally, we comment on factors affecting the adsorption of the initial layer of GO sheets upon the oil-water interface. Although it was possible to produce paraffin cored particles (as evidenced by Figure 2C,) the emulsions were in fact very unstable with the bulk of the paraffin wax coagulating soon after sonication was discontinued, even under low pH conditions. Both

naphthalene and 9-flourenone are aromatic and form very stable emulsions, while paraffin wax is aliphatic. It was hypothesized that the additional emulsion stability of the aromatic compounds is most likely due to π-π interactions with the GO and that the additional attractive forces and associated energy of adsorption from these π-π interactions play a critical role in the formation of HGOMs[12].

3.2. Graphene Oxide Membranes as Nanoparticle Carriers.

Upon sublimation of the oil phase (naphthalene), the PTFE particles remained within the graphene oxide shells, producing HGOM-PTFE composite core shell particles (See Figure 8 (A-C)). The darker PTFE particles can be seen within the GO membranes. In Figure 8D, we can observe the resulting plot of the HGOM-PTFE particle diameters as determined by laser diffraction. The results show that 80% of the volume was contained within the HGOM-PTEFs of diameters between 1.8 and 4.4 μm, with essentially no particles larger than approximately 6 μm. The mean size was 3.0 μm.

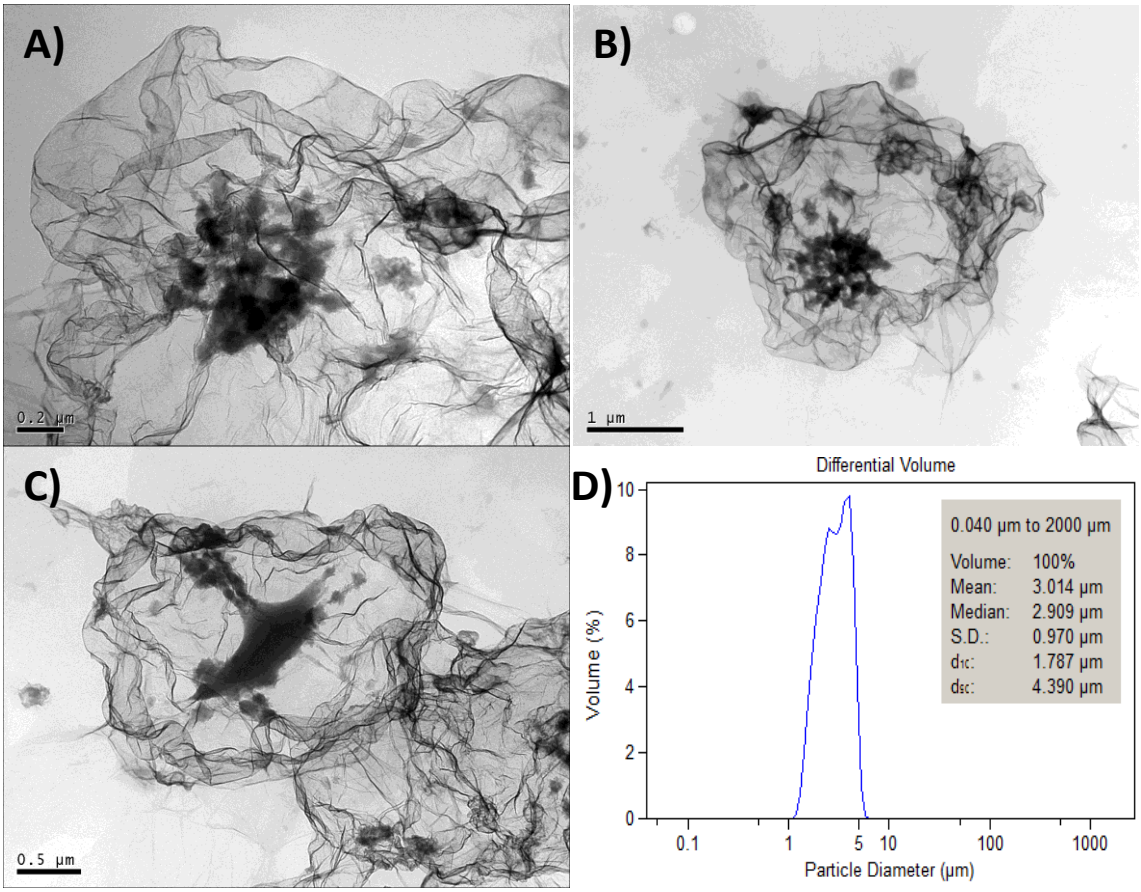

Figure 8: A-C) TEM images show the darker sub-micron polymer (PTFE) particles, loaded into the interiors of the HGOM. One potential application of these cargo carrying HGOMs is for drug delivery where nanoparticles or sub-micron polymer particles are loaded with drug. D) Plot of the size distribution of the encapsulated HGOM-PTFE particles produced through sonication.

Drug loaded polymer particles are being aggressively developed to target cancer and other diseases [32-34]. Although yet unexplored, HGOM core-shell drug delivery systems, using drug loaded polymer nanoparticles, could be a promising utilization of these HGOM nano-carriers. Furthermore, graphene oxide has been covalently functionalized by others to target cancer cells with specific receptors,[10]

and GO has been PEGylated to reduce renal clearance and increase circulation times [35,36]. It may be possible to functionalize the exterior of these HGOM core-shell drug delivery particles to assist in targeting disease. Figure 9 shows SEM and TEM images of silicon nanoparticles loaded into HGOM to further show that inorganic particles can be loaded into HGOM. The size of the silicon-HGOM composites core-shell particles produced through sonication varied depending upon the processing conditions. Silicon-HGOM particles as small as 560 nm were produced using a high power probe sonication method.

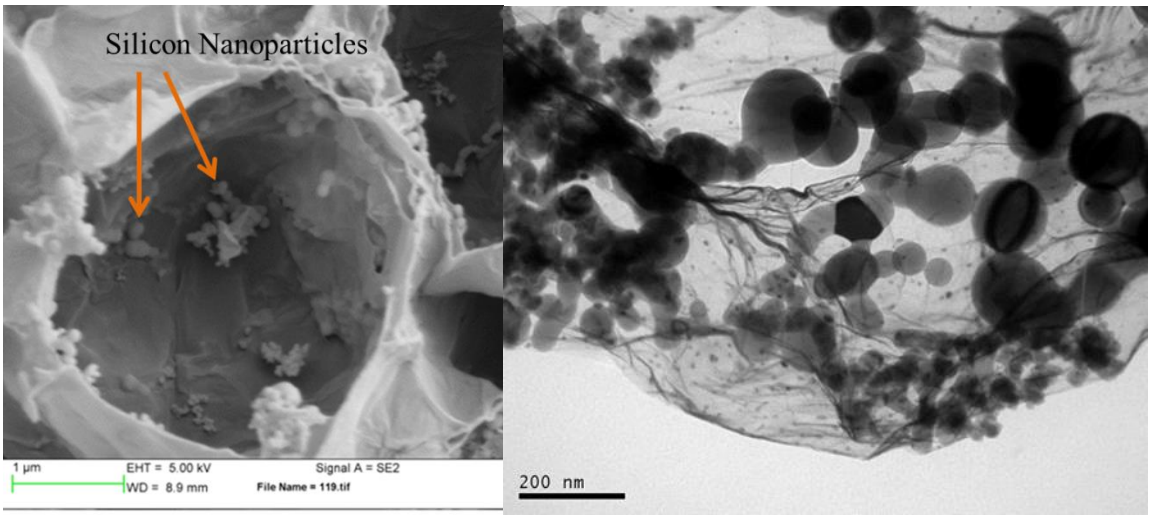

Figure 9: A-B) Silicon nanoparticles are encapsulated into the HGOM particles A) The SEM image shows the nanoparticles inside a HGOM particle which has been cut open. B) The corresponding TEM image shows the Silicon nanoparticles trapped inside the HGOM particle.

4. Conclusions and Summary

We have produced a novel method of producing nanoscaled HGOM hollow particles after sublimation of a naphthalene core. These structures were produced

using an oil in water Pickering type emulsion using graphene oxide as the stabilizing agent. These very thin shells may be vastly more useful in applications that require high specific surface areas, and will provide greatly decreased diffusion resistances in electrochemical applications such as lithium ion batteries. The hollow graphene oxide particles were also loaded with PTFE (Teflon) and also silicon nanoparticles, thus, demonstrating that they can be loaded with different types of particles such as polymers or electrochemically active materials.

We have identified processing parameters, such as GO concentration, shear rate and pH that produce graphene oxide stabilized Pickering emulsions. When these emulsions were subsequently cooled they produced stable suspensions of a solid oil phase wrapped in graphene oxide membranes. Proper adjustment of the processing parameters can provide control over the size of the templated membranes and the thickness of the graphene oxide layer. When high shear rates and high concentrations of graphene oxide were used, particles of smaller diameters with thick membranes were produced. HGOM particles with diameters as small as 500 nm to 3000 nm were produced for use as carriers for silicon and PTFE nanoparticles, respectively. By decreasing the concentration of graphene oxide, membranes as thin as 3 nm could be produced. Plotting the various processing parameters and the resulting particle characteristic results in three distinctive regions, which appear to be characteristic to this process. Region I consists of particles with nearly constant GO membrane thickness and varying particle diameter. Region II consists of a transition region in which the GO

concentration affects both membrane thickness and particle size. Region III consists of particles with constant diameter as the GO concentration is increased for a fixed shear rate.

Because this is fundamentally a directed self-assembly process, it is possible to achieve control over the size of the resulting droplets of the emulsion. It is a directed self-assembly process in the sense, that although the membrane of GO spontaneously forms upon the interface between the oil phase and aqueous phase, energy input (e.g., sonication, rotor-stator, high pressure homogenization, or energetic stirring) is required to finely divide the phases and create the interfacial area. The graphene oxide provides high stability to the emulsions, on the order of minutes or hours. The emulsions could be stabilized down to graphene oxide concentrations as small as 40 ppm. Increasing the graphene oxide concentrations above 40 ppm enhances the stability of the emulsions.

Naphthalene can be made to crystallize in thin platelets, however, our results show the emulsion droplets solidified spherically in the presence of GO, whereas 9-fluorenone produced needles when the same method was applied.

The process of coating the emulsion oil droplets with successive layers of overlapping graphene oxide is responsible for the resulting structures. Decreasing the pH assists in forming multiple layers of graphene oxide, since lower pH values favor the interactions between individual graphene oxide sheets and these

interactions are more favorable than the interactions with the aqueous phase. We found that pH conditions which resulted in zeta potentials of approximately -20 mV to -30 mV provided very stable emulsions. It is worth mentioning that stable emulsions using graphene oxide and naphthalene or other aromatic compounds could also be obtained without adding acetic acid. However, by adding extra acid, membranes become more hydrophobic and hence, the amount of GO that may migrate to the water phase is minimized. Thus, in this way GO sheets tend to be more attracted to the oil phase and stack to each other.

Future work includes incorporating these HGOMs into foams for use in supercapacitors, as an absorbent for the remediation of oil spills, and core-shell structures for use in catalysis and battery electrodes.

ACKNOWLEDGEMENTS

We acknowledge funding from the United States Department of Education, Grant Number P200A090356 Graduate Assistance in Areas of National Need (GAANN) and ERC-SOPS Engineering Research Center – Structured Organic Composites Rutgers University.

CHAPTER 3

Core-shell Graphene/Silicon Nanoparticles for use as Lithium-ion Battery Anodes.

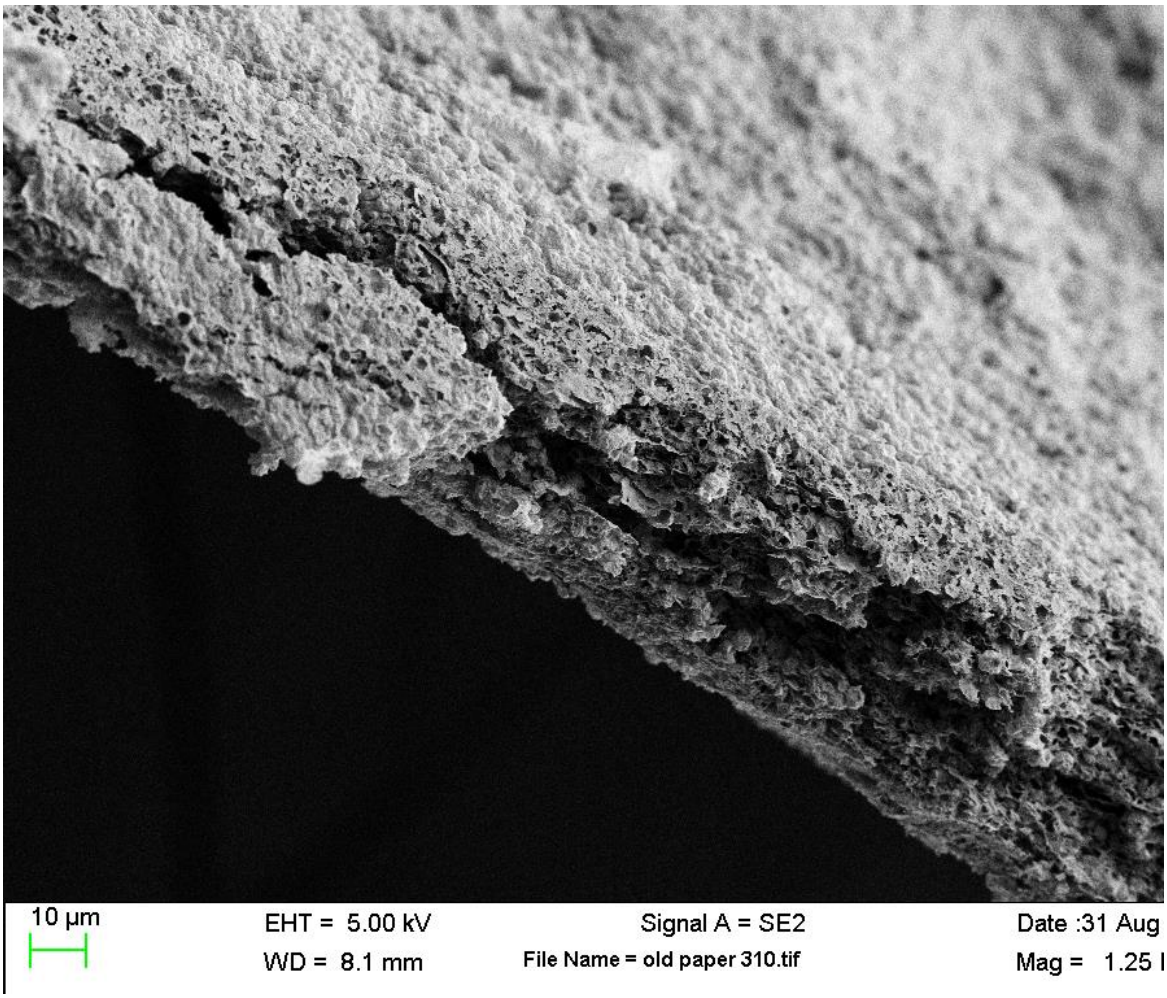

CHAPTER 3: CORE-SHELL GRAPHENE/SILICON NANOPARTICLES FOR USE AS LITHIUM-ION BATTERY ANODES.

Part of the data in this chapter has been published:

International Patent (Patent Cooperation Treaty) Application Number: PCT/US2017/035208, **publication number WO2017210289A1**, published 2017-12-07 (Applicant: RUTGERS, THE STATE UNIVERSITY OF NEW JERSEY [US]. Inventors: TOMASSONE, Maria, S., and SMITH, Kurt, B.). Also part of the data in this chapter has been published (all with named inventors as TOMASSONE, Maria, S., and SMITH, Kurt, B.) in **publication number CN109562933** (China [PRC] – from application number CN201780045866.6A) and in **publication number US20190326592** (United States – from applications US201662343480P and US62/343,480).

Smith, K. B. & Tomassone, M. S. Ultrathin Hollow Graphene Oxide Membranes for Use as Nanoparticle Carriers. Langmuir 33, 3765-3775, doi:10.1021/acs.langmuir.6b04583 (2017).

AIM 2: To develop the technology to interface graphene with other materials (Silicon) at the microscopic level through directed self-assembly and focus on a case study: the creation of Silicon-Graphene Based Anodes for Lithium Ion Batteries.

ABSTRACT

Silicon nanoparticles were encapsulated in hollow graphene shells with controlled void space to form an anode with high lithium ion storage capacity. An electrode with high cycling stability was made which exhibited a storage capacity of 1450 mA h/g after 200 cycles and greater than 1300 mAh/g after 350 cycles. The coulombic

efficiency of the anode rapidly rose as cycling continued, eventually reaching 99.9%. The electrode materials were characterized via laser diffraction, battery cycling, FE-SEM, TEM, and XRD. Capacities greater than 1200 mA-hr/g were possible at a current of 3200 mA/g.

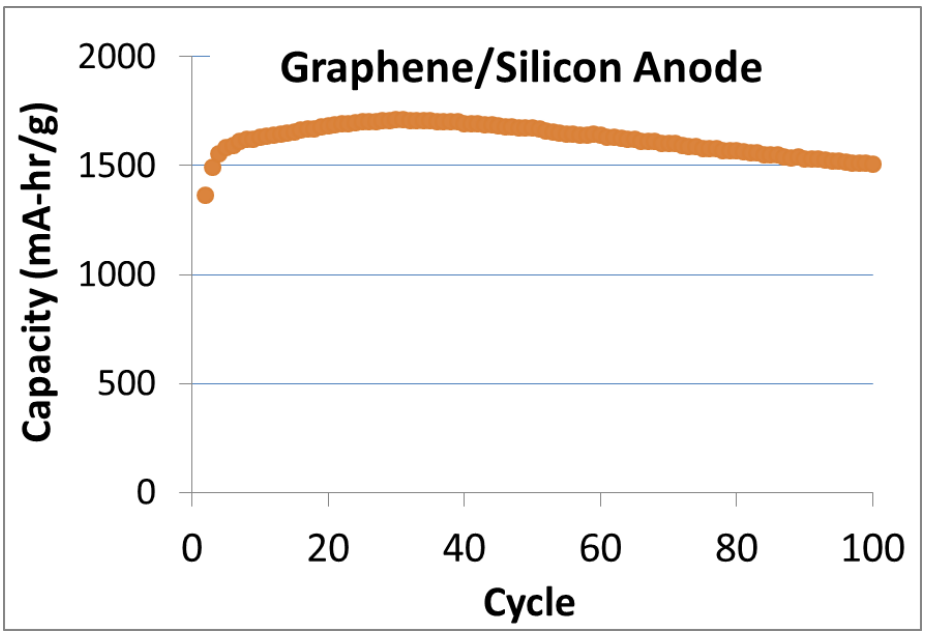

---

1. INTRODUCTION

Although lithium-ion batteries have the highest specific energy capacity of any rechargeable battery chemistry in wide-spread use today the cycling stability and specific energy capacity of these batteries are still problematic for all-electric vehicles and a host of other high energy applications.[3,37] Increasing the capacity of these batteries is crucial to keep pace with the demands of these new applications.

To decrease the weight of the anode, researchers have turned to materials with higher specific capacity than graphite, the most commonly used anode material in

commercially available batteries. Silicon, with the highest known lithiation capacity of any material, has about 10 times the theoretical capacity of graphite.[38] It has been noted that increasing the capacity of the anode up to about 1000 mAh/g greatly increases the total capacity of a lithium-ion battery cell.[39]

Silicon has previously been used by a number of researchers, who have used simple and straightforward mixtures of graphene oxide and silicon in a suspension, however, they tend to have poorer cycling stability.[39-43] Other, more complicated techniques, use hazardous materials or are difficult to scale up.[44,45]

There are several well-known issues with utilizing silicon in anodes, both related to the fact that silicon undergoes a high expansion ratio upon lithiation (during the cycling of a battery). As the battery is charged (lithiated) expansion occurs in the anode, and as the battery is discharge (delithiated) contraction occurs in the anode. The volumetric expansion is only 10% percent for graphite,[46] but is approximately 300% for silicon.[47] Using crystalline silicon particles which are less than 150 nm or amorphous silicon particles less than 870 nm prevents fracture of the silicon as expansion and contraction occurs during cycling.[48-50] Even when using these smaller silicon particles, the high volumetric expansion and contraction in the silicon can induce mechanical stress and leads to reformation and breakage of the solid electrolyte interface (SEI) during cycling producing loss of capacity and stability.[3] The SEI layer is a polymeric boundary which naturally forms from the electrolyte at the surface of the anode and is known to further protect the electrolyte from further reactions at the surface of the anode.[51] However, if the

expansion ratio of the anode materials is sufficiently high, it appears that the SEI layer is broken and reformed to some extent during each cycle, thus leading to loss of efficiency and cycling stability.[52]

In addition, it is important to notice that when silicon nanoparticles are incorporated into the anodes, the silicon needs to be in an electrically conductive environment (such as is provided by reduced graphene oxide or various binders with carbon black as a conductive additive). With such slurries there is the potential for uneven distribution of the silicon nanoparticles within the composite matrix and many papers have commented on the need of achieving well dispersed composites or a uniform distribution of the composite components.[39,40] The silicon nanoparticles can agglomerate if the particles do not interact favorably with the matrix material in the composite. Since many composites originate in the form of liquids or pastes the potential for segregation is high for those systems before the composites are solidified.

Our approach consists of encapsulating silicon nanoparticles inside hollow graphene oxide membrane particles (HGOM) and thus, it avoids the uneven distribution of the silicon particles, where the HGOM particles act as nanoparticle carriers. When silicon nanoparticles are encapsulated inside these hollow sacks, they do not occupy the entire volume leaving some “void space” necessary to accommodate the physical change in volume of the silicon nanoparticles during cycling of the batteries. Such particles are often called “yolk-shell” particles (with a

core@void@shell configuration) to distinguish these from simpler core-shell particles (core@shell configuration) in which there is no interstitial void space between the core and shell.[53,54] In our method, the SEI forms around the graphene shells rather than around the silicon particles, which has a much smaller and more stable surface area providing larger stability and enhancement of capacity.

We have recently published a method to obtain these hollow graphene oxide membrane particles with controlled size and thus, controlled void space.[55] Here, we propose a new facile method, for engineering the required void space and controlling the formation of the SEI around HGOM particles, which are assembled into anodes for Lithium ion batteries. There has been significant work in the area of graphene oxide based anodes. Liu, M. X. et al., were able to grow MnO_x layers on the surfaces of reduced graphene oxide (rGO) to produce high capacity, high power supercapacitor electrodes.[44] They noted that the core-shell 3D nanoarchitecture avoided aggregation and leaching of the manganese oxides which 'guaranteed' the full activity of the electroactive components.[44] These core shell particles incorporated the reduced graphene oxide in the interior of the particles rather than use the graphene oxide as the shell.

Some work has been accomplished with the aim of encapsulation of silicon or other materials within carbon spheres for the construction of anodes.[42,45,52,56] S. B. Yang et al[45] wrapped graphene oxide around Co_3O_4 with good stability, however the lower capacity of Co_3O_4 compared with silicon limits the capacity gains attainable.

However, this method which does not employ the creation of void space was not able to accommodate the volume expansion of silicon. Yu Zhou et al[56] followed a modified approach by coating silicon nanoparticles with phenolic resin and graphene oxide, followed by chemical and thermal reduction. Even using a relatively low silicon content of 29% did not result in very high cycling stability.

Recently, the less explored use of "yolk-shell" particle structures have been incorporated into lithium-ion battery anodes using a number of active materials.[57,58] Both Nian Liu et al [52,59] and L. Y. Yang et al [45] used tetraethyl orthosilicate (TEOS) to created carbon encapsulated silicone particles with void space, but the process requires removal of the sacrificial silica scaffolds through harsh chemicals and diffusion in a liquid state. Under these conditions it was not possible to recycle these materials. Zhai et al created porous core-shell particles for use in Li-ion batteries, by chemically etching aluminum-silicon particles with hydrochloric acid.[60] Considerable waste materials must be produced to create the necessary void space in this method as well.

Yang Xiang et al trapped Cr_2O_3 within carbon and graphene shells using a spray drying method, however, the lower capacity Cr_2O_3 limited the capacity of the final anode.[61] The capacity of these anodes at 120 cycles was only 41% of the capacity which we have demonstrated with our new method.

Very recently, Mingru Su et al also used a spray drying method to combine graphene oxide and silicon nanoparticles to produce spheres composed of reduced graphene oxide and silicon.[42] However it is unclear what the interior structure of these sphere are composed: they report free silicon particles on the exterior of the spheres at low graphene oxide concentrations, and a 'disorganized' structure at high graphene oxide concentrations. The best results they were able to attain resulted in capacities which dropped rapidly from the first cycle capacity of 1298 mAh/gr to 600 mAh/g at only 50 cycles, the maximum number of cycles which they reported. Our method appears to provide much higher stability as we report capacities greater than 1300 mAh/g after 350 cycles.

We employ a different technique based upon the newly discovered method of encapsulating silicon nanoparticles within graphene oxide shells, through the process of emulsification-precipitation, followed by sublimation of naphthalene [55] and assembly into anodes. To our knowledge this method has never been accomplished before. This method has the potential to be scalable, while being able to control the void space within the core-shell structure. Although a sacrificial scaffold is used to create the void space, there is a great potential to recycle this material since no reactions occur during sublimation of the sacrificial scaffold.

Thermal reduction (pyrolysis) of the silicon/HGOM core shell particles yields highly conductive composites. Since the silicon nanoparticles have very high specific

capacity, the resulting composite also has high specific capacity, thus increasing the specific capacity of lithium-ion batteries which employ these composites.

Section 2 is focused on the experimental methods, Section 3 explains the results obtained and provides a discussion and Section 4 is devoted to the conclusions.

2. MATERIALS AND METHODS

2.1. Summary of the Materials.

Naphthalene and acetic acid were purchased from Sigma Aldrich, and used as received. C-Nerge Super C65 conductive additive was donated by Timcal America, Inc. (Westlake, Ohio). Silicon nanoparticles (20 to 30 nm) were purchased from US Research Nanomaterials, Inc. (Houston, Texas). No surfactants, other than the graphene oxide were added to form the emulsions. The glassware and all experimental components were thoroughly washed with acetone and DDI water prior to use. Ultrapure Milli-Q water produced from the Millipore system, was used as the water source throughout, including the purification of graphene oxide, and as the source of water for the emulsions, as well as the final rinse water for all glassware and equipment.

2.2 Methodology.

2.2.1 Graphene oxide production:

Graphene oxide was synthesized through a modified Hummers method developed by Kovtyukhova and others[26]. In this process we used natural flake graphite (grade

230U) donated by Asbury Carbons. The graphene oxide was then washed 10 times with DDI water and sonicated with a Misonix S3000 probe sonicator with a power setting of 4.5. During sonication, the vial was removed and cooled every 90 seconds. After a total sonication time of 15 minutes the lateral mean size of the graphene oxide sheets was on the order of 0.53 μm.[55] The exact details of the synthesis and characterization are detailed in Chapter 2 of this Dissertation.

2.2.2 Hydrophobic Functionalization of the Silicon Nanoparticles: Silicon nanoparticles (20 to 30 nm) were purchased from US Research Nanomaterials, Inc. (Houston, Texas) and made hydrophobic through a surface treatment in a standard process.[62]. In this approach, the surface was capped through covalent bonds with hydrogen. The silicon particles (e.g., 1 g) were placed inside a polyethylene bottle and 30 mL of 15% hydrofluoric acid (HF) was added. The solution was allowed to stand at room temperature, during this time, the hydrophilic surface oxide layer (SiO_2) of the silicon particles was removed and replaced with a hydrophobic, hydrogen capped surface. After standing for two hours at room temperature, 30 mL of hexane was added to the silicon particles and HF solution. The hexane layer and treated silicon particles (which then have a hydrogen-capped hydrophobic surface) were together removed by a plastic pipette. The hexane, containing the silicon particles was evaporated to dryness, to yield the final dry product of hydrogen-capped silicon particles. The hydrogen capped silicon nanoparticles were either used immediately or were stored in a tightly sealed vial under hexane. Further functionalization of the silicon surface with alkanes[63] or other hydrophobic

components was considered as a method to both increase the silicon nanoparticle affinity for the oil phase, and increase the oxidative stability of the surface. Such additional treatments have previously been described in the literature to suspend silicon nanoparticles in oil phases, although not for doing so within graphene oxide shells. [29] However, it was found that when the HGOM-Si composites were processed soon after capping with hydrogen that further functionalization was unnecessary.

In what follows we will explain the different steps to synthesize the final anodes by encapsulating silicon nanoparticles, with hydrophobic surfaces, inside of the HGOM particles after sublimation of the naphthalene. To produce the HGOM on naphthalene cores we have used the method explained in Chapter 2 Section 2.2 of this Dissertation

2.2.3 Synthesis of the Silicon-HGOM particle composites: Naphthalene was heated and the hydrogen capped silicon nanoparticles were dispersed into the liquid naphthalene. A few minutes before the addition of the silicon nanoparticles, the silicon nanoparticles were dried at 40 °C to ensure no hexane was added to the naphthalene phase (and lowered its melting point) and to facilitate accurate weights of the hydrogen capped nanoparticles. An aqueous dispersion of graphene oxide was also heated and the naphthalene liquid containing the hydrophobic silicon nanoparticles was added. Energy to create an emulsion is added to create a fine oil-in-water type emulsion, consisting of the silicon nanoparticles containing droplets of naphthalene dispersed in the aqueous phase. Droplet size was reduced

and controlled by applying shear through the application of sonication power. Upon cooling of the emulsion, the hybrid droplets of silicon nanoparticles and naphthalene solidify and the solid cores become wrapped in a shell of graphene oxide. The overall process is shown in **Figure 10**.

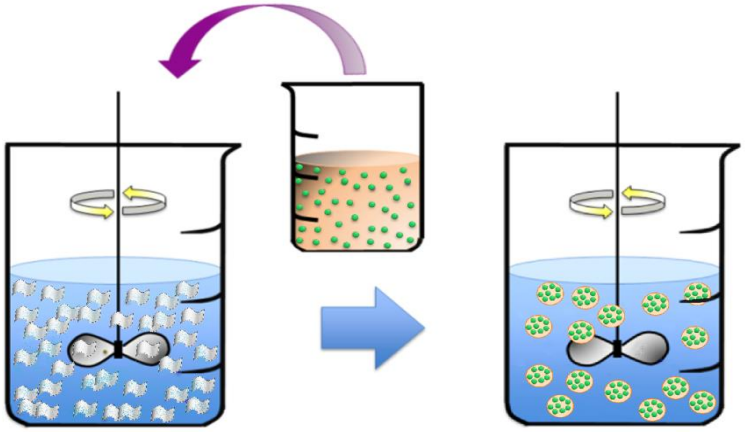

Figure 10: An oil phase (shown at the top in orange) with suspended electrochemically active nanoparticles (shown as green particles) which has been made hydrophobic (e.g., H-capped silicon nanoparticles suspended in naphthalene) are added to an aqueous suspension of graphene oxide sheets (left) and shear is applied through rapid mixing, rotor-stator, or sonication. At the right: the graphene oxide sheets form shells around the oil phase which is cooled to form a solid with the electrochemically active nanoparticles trapped inside.

An important consideration is the relative volume of silicon nanoparticles to the available space within the hollow graphene oxide membrane particles. The lithiated volume of the silicon is by some calculations (depending upon the final lithiation state) as much as 4.12 times the volume of the unlithiated state.[47] Additionally, we should expect that some pore volume remains around the silicon nanoparticles,

increasing the space needed to accommodate the silicon without producing excessive forces on the membrane shells.

In a 40 mL glass vial 100 mg of hydrogen caped silicon nanoparticles were added to 0.530 g of naphthalene and the naphthalene was briefly melted above 80°C to become a liquid to wet the silicon nanoparticles. Afterwards, 33.3 g of 0.20 wt % graphene oxide suspension and 2.00 mL of glacial acetic acid were added to the naphthalene wetted silicon nanoparticles and then sonicated with Misonix S3000 probe sonicator at 30 W for 4 minutes, The final temperature of the mixture at the end of sonication was near the boiling point (100˚C). These processing parameters have been adjusted to facilitate the directed self-assembly of the yolk-shell particles creating shells of graphene oxide at the interface of the oil droplets. Surface tension, interfacial energy and processing parameters affect assembly of the composite particles and their ultimate size.[30,31,33,34,64] We previously published an extensive study allowing for the engineering of these yolk-shell particle properties.[55]

We have utilized three different methods to synthesize the anodes. The first is by using thermal reduction producing free standing anodes (without any copper currant collector/substrate). The second approach using chemical reduction method using a copper foil. The third method is a thermal reduction method with alginate binder using copper foil current collector. All three approaches are explained below. We have concentrated our efforts on characterization of the anodes on what we believe to be the most promising approach, thermal reduction of

free standing anodes. However, we include addition results, of other methods of anode construction, for comparison.

2.2.4 Thermal Reduction Method Producing Free Standing Anodes: We first considered a Si-HGOM particle suspension with solid naphthalene cores. A thin layer of the suspension was placed in a petri dish and allowed to dry for two days in an oven at 60°C. After naphthalene sublimation the film was removed and cut into free standing anodes (without any copper foil current collector), containing no additional binder or conductive additives. The freestanding anode was then thermally reduced by heating in a Thermo Scientific Lindburg Blue M horizontal tube furnace to 600˚C, 700˚C, or 900˚C under flowing nitrogen with 10% hydrogen. Typical loading of the Si-HGOM particles was about 0.5 mg/cm^2.

2.2.5 Chemical Reduction Method: We first considered a Si-HGOM particle suspension with solid naphthalene cores. The Si-HGOM was then mixed in an aqueous suspension with sodium alginate (which acts as a binder) and a C-Nerge Super C65 conductive additive (Timcal; Westlake, Ohio) was pasted to a 10 mm diameter copper foil. The ratio by weight of Si-HGOM particles, sodium alginate, and conductive additive was 75:20:5 percent respectively. We allowed the binder to dry and the naphthalene cores to sublime. To reduce the graphene oxide we utilized a method proposed in the literature[65] for the reduction of graphene oxide sponge. We adapted the method for our application, in which **t**he anode was first placed in a sealed container adjacent to another beaker that contains hydrazine monohydrate.

The vapors of hydrazine in the sealed environment interact with the graphene oxide anodes and chemically reduce the graphene oxide particles making them electrically conductive (Figure 11). The anodes were then removed and the naphthalene cores were allowed to sublime.

Figure 11: The anode (in the small beaker right) is chemically reduced under hydrazine vapor by sealing the anode in a large beaker with an open container (small beaker left) of liquid hydrazine monohydrate

2.2.6 Thermal Reduction Method with Alginate Binder and Copper Foil Current Collector: We first considered a Si-HGOM particle suspension with solid naphthalene cores. A thin layer of the suspension was placed in a petri dish and allowed to dry in a desiccator which in addition to desiccant also contained a petri dish of naphthalene. Under these conditions the water was dried from the Si-HGOM particle suspension but the naphthalene was not removed. The dried film was removed from the petri dish and crushed and placed into an oven at 60 °C for 2 days to allow sublimation of the naphthalene from the Si-HGOM particle. The Si-HGOM

was then mixed in an aqueous suspension with sodium alginate (which acts as a binder) and a C-Nerge Super C65 conductive additive (Timcal; Westlake, Ohio) was pasted to a 10 mm diameter copper foil. The ratio by weight of Si-HGOM particles, sodium alginate, and conductive additive was 75:20:5 percent respectively.

2.2.7 Assembly of the anodes into a electrochemical cell: The Si-HGOM anodes were dried are then transferred to an argon filled glove box for assembly into to a Swagelok cell with a lithium foil counter electrode, using a binderless micro-fiber fiberglass separator, and 1.0 M $LiPF_6$ in 1:1 volume ethylene carbonate: dimethyl carbonate (EC : DMC) electrolyte.

2.3 Characterization.

The electrochemical cells were cycled on a MTI BST8 Battery Analyzer (Richmond, California) using the constant current method. The capacity was determined based on the mass the Si-HGOM, which for free standing anodes is the entire mass of the anodes.

A high-flux rotating anode x-ray generator (CuKα radiation at 1.54 angstroms) and a sensitive Bruker HiStar area detector were used to gather X-ray diffraction patterns from the unreduced and thermally reduced composite of silicon nanoparticles encapsulated in the graphene oxide spheres. The powder XRD patterns were obtained by integrating the area detector to obtain patterns in units of 2-theta.

Transmission electron microscope (TEM) images were obtained using a Jeol JEM-100CX II, using copper grids. After sample preparation both SEM and TEM samples were dried and then held at 60 °C in a double walled beaker overnight to ensure all of the naphthalene was sublimed. Scanning electron microscope (SEM) images were acquired using a Zeiss Sigma Field Emission SEM. SEM sample stubs were prepared by applying liquid suspensions to a mounted silicon wafer with a pipette. SEM samples were allowed to dry and were then vacuum desiccated and sputter coated, using a Balzers SCD 004 Sputter Coating Unit with Gold/Palladium Target (Au:Pd 60/40 ratio), prior to imaging. Additional SEM images were obtained using a Zeiss Sigma Field Emission SEM. Particle size analysis was performed using a Beckman-Coulter LS-13 320 laser diffraction apparatus with a universal liquid module filled with distilled deionized water. A refractive index of 1.582 was used to define the naphthalene cored particles.

3. RESULTS AND DISCUSSION

Silicon nanoparticles along with naphthalene were successfully placed within the graphene oxide shells using this method. It is possible to control the Si-HGOM particle size and composition. For example we were able produced Si-HGOM particles diameters as large as 6 μm using lower shear levels when making the emulsions. The naphthalene was easily sublimed yielding hollow graphene oxide particles with encapsulated silicon nanoparticles as can be seen in the transmission electron microscopy (TEM) images in **Figure 12**. By using higher ratios of silicon to graphene oxide the silicon content could be controlled. The core-shell Si-HGOM

particles shown in the TEM image of **Figure 12** and the SEM image of **Figure 13** produces a 90% silicon anode when thermally reduced at 700°C.

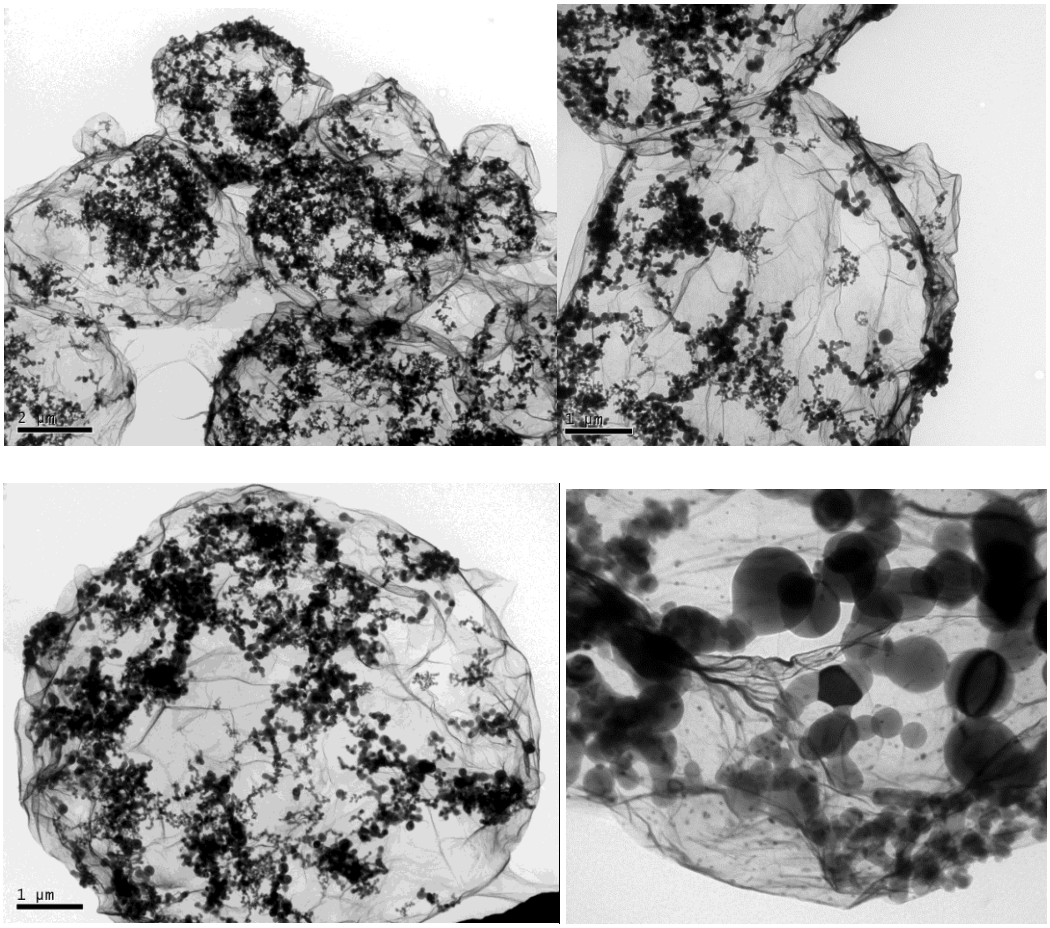

Figure 12: TEM images of thin graphene oxide sacks with silicon nanoparticles added to the spheres.

Under these conditions, the TEM images show silicon nanoparticles, approximately 30 to 80 nm in size, encapsulated in graphene oxide shell membranes which are approximately 5 micrometers in diameter. SEM images in Figure 13 show the cross sectional area which has been cut with a razor blade. The higher magnification SEM image reveals the silicon nanoparticles within the cut open HGOMs.

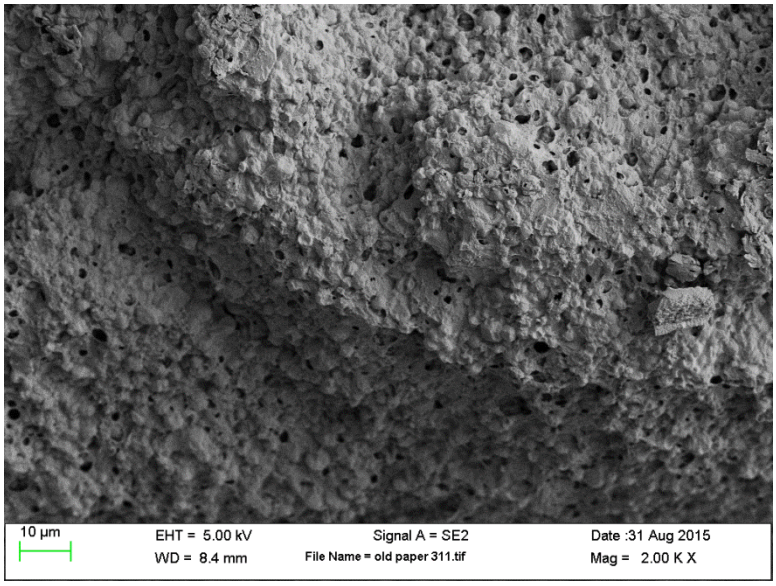

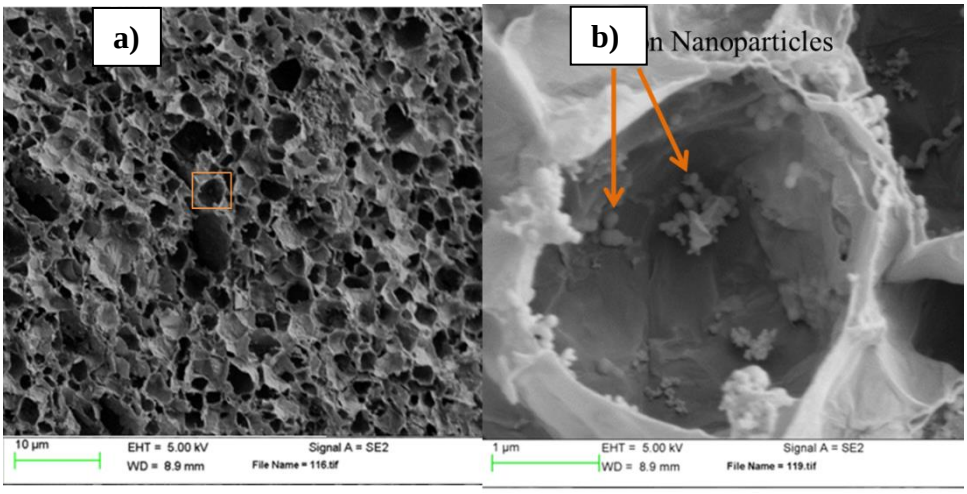

Figure 13: a) SEM images of the composite HGOM-Si anode made with larger shells. b) The boxed area in the left image is shown with higher magnification in the right image and reveals silicon nanoparticles inside the cut open HGOMs.

The schematic in **Figure 14** shows the HGOM-Si particles which we have successfully made by this process, with graphene oxide platelets providing mechanical linkage between the spheres. For this system we have added no binder or conductive additive, since the reduced graphene oxide serves both purposes. Upon thermal reduction the graphene oxide yields a free standing network of highly electrically conductive carbon and graphitic phases, with the silicon nanoparticles in intimate electrical contact throughout the electrode. Some areas in the lower SEM image are collapsed beyond the resolution of the SEM image and appear as more or less solid bands:

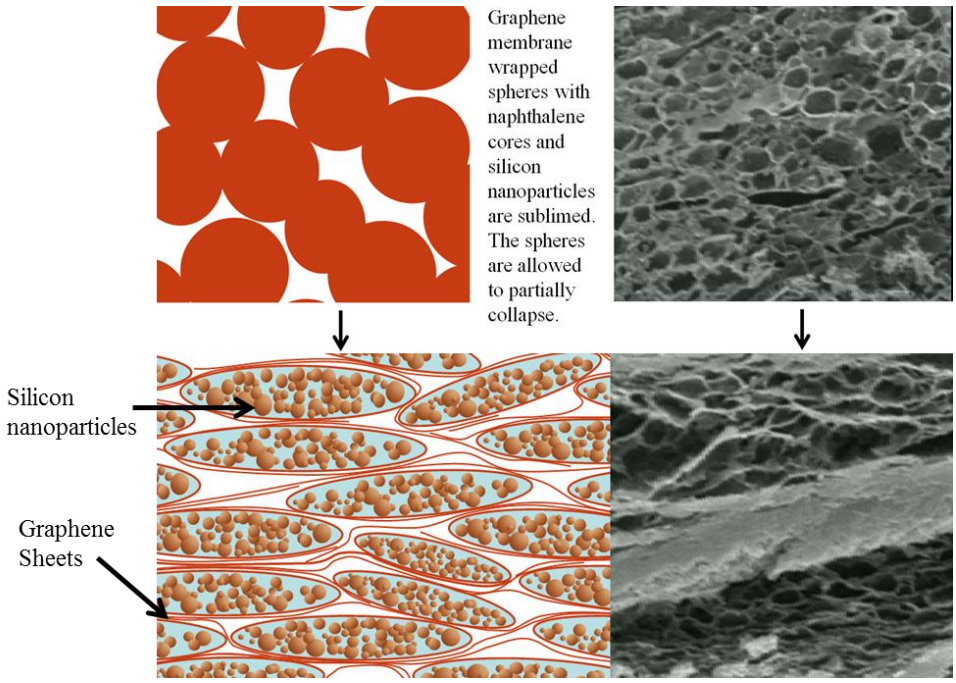

Figure 14: Schematic showing Graphene oxide membrane spheres containing silicon nanoparticles form a composite for use as anodes in lithium ion batteries and sulfur-lithium ion batteries. The upper left drawing shows the cross section of uncollapsed naphthalene filled Si-HGOM spheres. At the right, the upper SEM image shows uncollapsed spheres, prepared by cutting the GO/Si-NP composite with a razor blade. The upper SEM image (at the right) is taken directly into of the face of the cut (into the edge of the anode) and shows graphene oxide spheres of this sample, which were cut open by the razor blade, and which are now hollow, since the naphthalene was sublimed before the SEM image was taken. The lower SEM image (at the right) shows a cross section of an anode prepared by cutting the sample with a razor blade after being partially collapse by applying pressure to the composite after sublimation of the naphthalene cores. The silicon nanoparticles are

beyond the resolution of the SEM image. The lower left drawing is an interpretation of the structure produced by this method after collapsing of the spheres.

This desired state allows for flexibility of the graphene oxide shells, which are then compressed but remain intact and flexible for expansion and contraction about the silicon nanoparticles as the battery is cycled.

By controlling the emulsion parameters, such as increased shear rates, smaller core-shell graphene oxide particles are produced. This also allows for the reduction in the thickness of the graphene oxide layer[55]. The structure of the sub-micron diameter composite spheres of silicon nanoparticles encapsulated in graphene oxide membranes are shown in the TEM images in **Figure 15.**

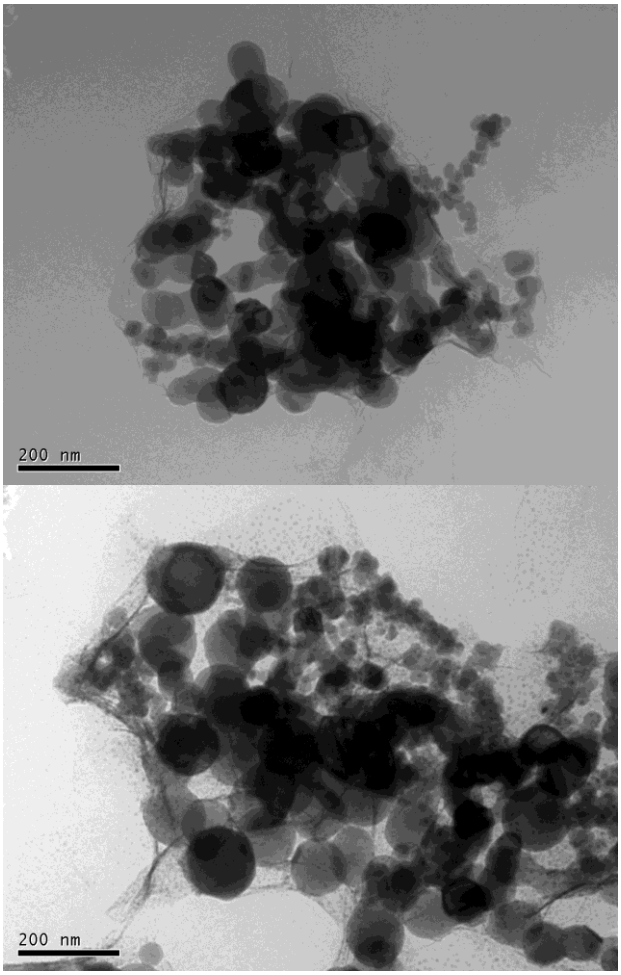

Figure 15: By increasing the ratio of graphene oxide to silicon nanoparticles smaller composite particles are produced (compared to those in Figure 12).

There is not a significant amount of aggregation of silicon nanoparticles because the silicon nanoparticles are inside the graphene oxide sacks. These TEM pictures show silicon nanoparticle encapsulated graphene oxide shells less than 1.0 micron. Shell thickness is on the order of 6 nm.

Figure 16 contains the particle size distribution of the naphthalene filled Si-HGOM spheres obtained using laser diffraction. The particle size distribution, normalized

by surface area is between 0.1 μm and 4 μm. The Sauter mean diameter (d_{32})[27] of the yolk-shell particles is 0.56 μm.

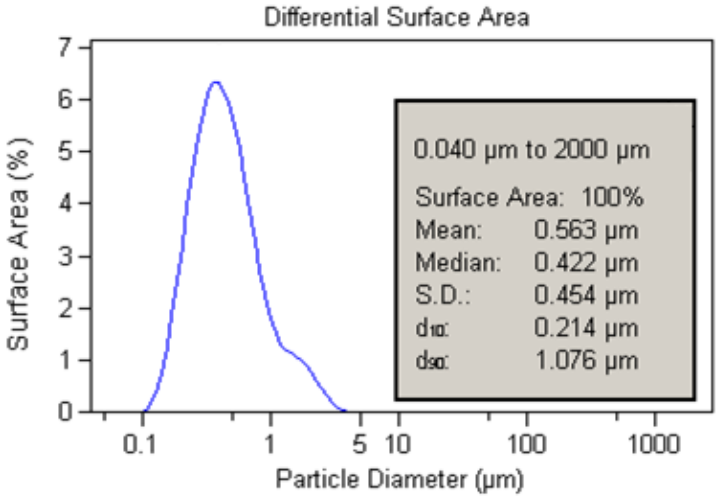

Figure 16: Size distribution of the hollow graphene oxide membranes which are filled with silicon nanoparticles.

The XRD pattern for the unpyrolyzed sample in **Figure 17** shows the GO stacking peak (002) at 12.4 degrees, corresponding to approximately 7.1 angstroms, and is indicative of the interlayer spacing of the graphene oxide sheets. The membrane shells of the graphene oxide spheres, although they appear to be well defined in TEM images, are thin and therefore may produce a weaker GO 002 XRD peak than might otherwise be expected.

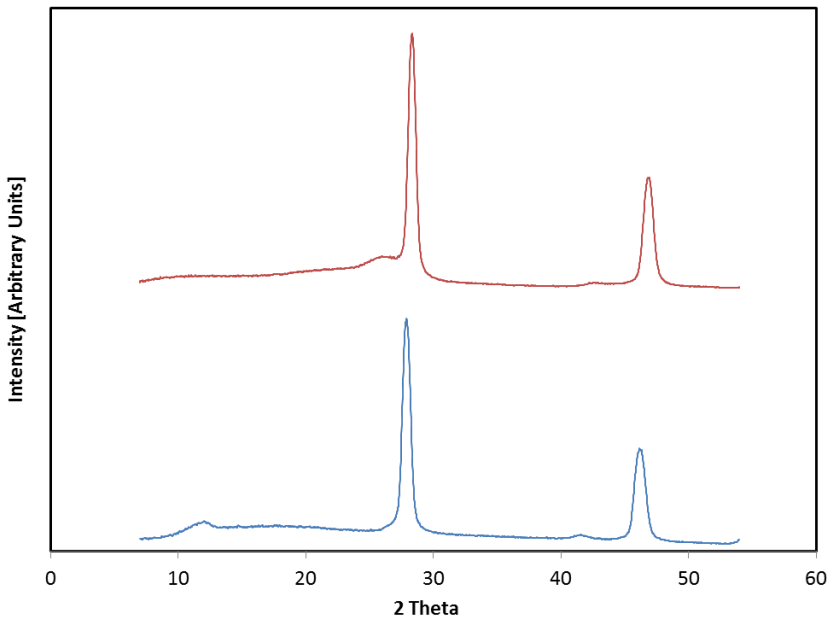

Figure 17: Upper XRD pattern (red) is for the pyrolyzed sample of silicon nanoparticles encapsulated in the graphene oxide spheres (HGOM-Si). The lower XRD pattern (blue) is the unpyrolyzed HGOM-Si sample. Intensities are offset for clarity. This figure corresponds to the thermally reduced anode.

The Peak at 26 degrees (3.4 angstroms) of the thermally reduced (pyrolyzed) sample corresponds to the interlayer spacing of graphite, and it can be inferred that the material becomes somewhat graphitic in nature as thermal reduction occurs, since the peak is absent in the unreduced sample, but except for the silicon peaks is dominate in the pyrolyzed sample. The graphene/graphene oxide peak at 42 degrees (100) has been described in the literature for graphene oxide and reduced graphene oxide. The diffraction peaks at 28 and 47 degrees are typical of silicon (111) and (220), respectively and are an indication that the silicon is crystalline and has not been oxidized under the processing conditions. The labeling of the

diffraction pattern peaks for graphene and graphene oxide follows the assignments from Physics and Applications of Graphene – Experiments.[66]

The Scherrer equation, yields an approximate silicon crystallite size of 20 nm, using a shape factor of 0.9 based on the equation for full width at half maximum (FWHM) of the silicon 111 and 220 peaks. No broadening of the peaks was observed in the pyrolyzed sample. Many of the silicon particles are on the order of ~20 nm, however the TEM images reveal that there are many 80 nm diameter particles as well. It is possible that the nanoparticles contain more than one crystallite domain, and that the domain size is on the order of 20 nm.

Raman spectra of the thermally reduced anodes were acquired with an excitation wavelength of 514 nm**. Figure 18** shows the Raman peak of the D band is at 1340 (cm^{-1}) and the G band is at 1591 (cm^{-1}), for the unreduced anodes samples. The reduced samples have the D band at approximately 1349 (cm^{-1}) with the G band at 1595 (cm^{-1}). Figure 18 shows that the Raman peak of the D band is at 1358 (cm^{-1}) and the G band is at 1594 (cm^{-1}). This is very similar to other studies which have reported graphene oxide D band in the range of 1354 (cm^{-1}) to 1363 (cm^{-1}), and the G band in the range of 1594 (cm^{-1}) to 1591 (cm^{-1}). [8,67] Those studies reported very similar results for the peak positions as those of Figure 18 for reduced graphene oxide, although the method of reduction was different than ours, either using chemical or under microwave radiation to assist reduction.[8,67] For reduced graphene oxide the peak positions in those studies were reported for the D band in

the range of 1348 (cm^{-1}) to 1352 (cm^{-1}), and the G band in the range of 1584 (cm^{-1}) to 1591 (cm^{-1}) .[8,67] Although, Stankovich et al report the intensity ratio of the D band the G band to increase with chemical reduction of graphene oxide, Parades and Chen both reported little change this ratio upon reduction.[8,67,68] The largest silicon peak at approximately 520 (cm^{-1}) in all of the samples, is consistent with crystalline silicon. [69] [70]

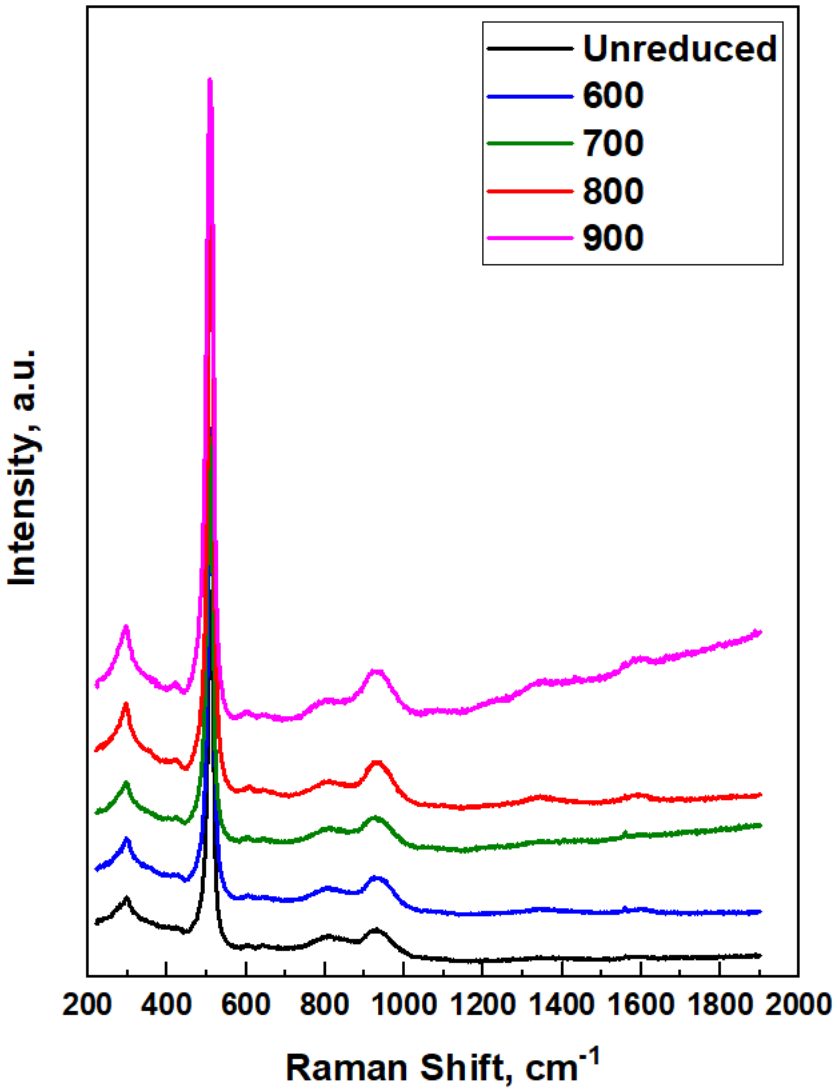

Figure 18: Raman spectra of thermally reduced anodes.

The capacity of unreduced and chemically reduced Si-HGOM anodes made are displayed in **Figure 19**. Both of these anodes were both made with alginate binder. The chemically reduced anode is much more stable than the unreduced anode.

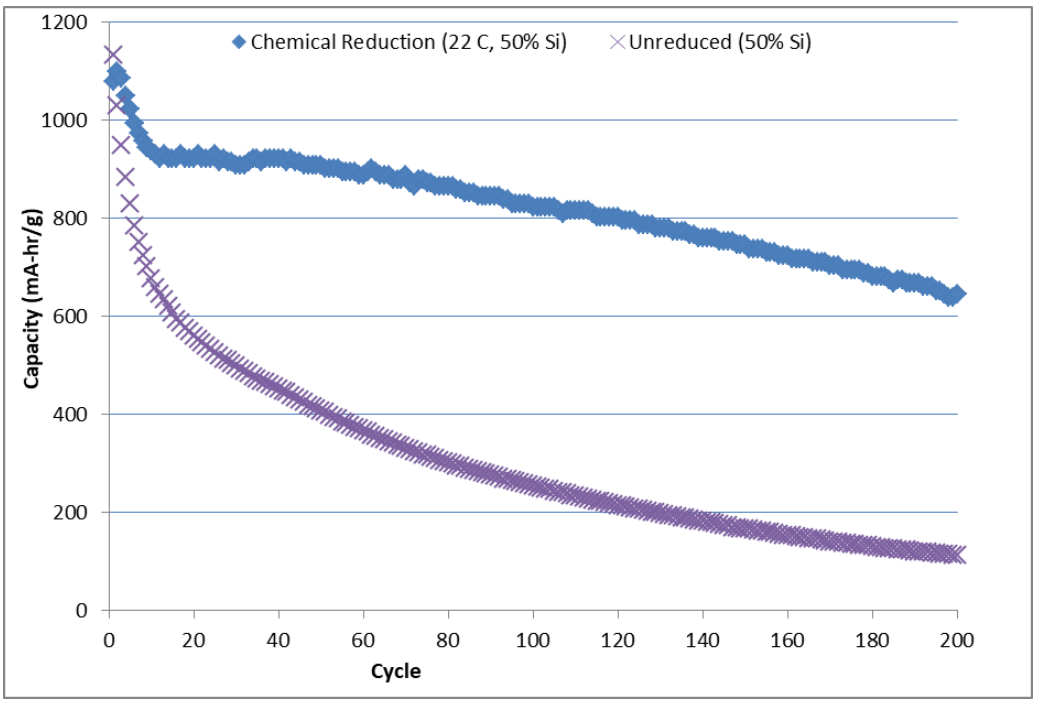

Figure 19: Capacity vs numbe of Cycles for anodes made from unreduced HGOM-Silicon nanoparticles with alginate binder. In the unreduced anode (purple) was cycled and shows a relatively fast decay with poor stability. The second sample (blue) was chemically reduced by exposing the sample to hydrazine vapor at and room temperature for 3 days before assembly into a cell.

The HGOM-Si anode material was assembled in a test cell and repetitively charged and discharged on a battery analyzer. In **Figure 20** we observe that when the rate of charge is increased, the total charge (capacity) in the anode decreases. This is

because at larger charge rates, the overpotential of the anode increases, and therefore the capacity decreases. [The overpotential is the difference between the potential (Voltage) at the cell terminals and the equilibrium potential (equilibrium Voltage) of the cell.]

After 90 cycles, we reduced the rate of charge on the anode and the total charge reversed its behavior, increasing again. As the rate of charge was decreased to the original value of 50 mA/g, the capacity of the anode nearly achieved the initial value.

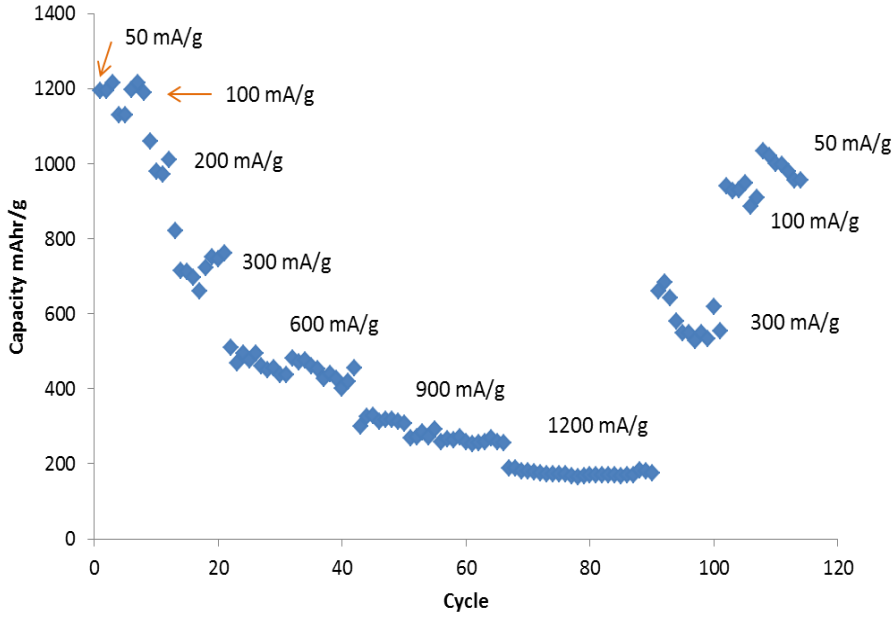

Figure 20: Systematic study of the total charge on 50% silicon HGOM-Si anode which was thermally reduced at 700 °C and assembled with alginate binder. The capacity of the anode was cycled at different charge and discharge rates.

The rate capabilities of the HGOM-Si anodes with 75% silicon were studied by cycling with constant current charge and discharge current densities from 150 to 3000 mA/g. **Figure 21** shows that at the current densities of 150, 300, 600, 1200 and 3000 mA/g the discharge capacities are 1951, 1807, 1645, 1429, and 947 mAh/g respectively. Thus the total capacity of the cell decreased as the current density was increased. Notice that the rate of charge was increased up to 3000 mA/g and was kept constant thereafter, showing good stability.

Another interesting factor is that the capacity at low rates of charge and discharge is nearly proportional to the silicon content of the anodes. However, there is great difference in the capacity at high rates of charge and discharge. This may be due to the higher reduced graphene oxide content, which is double for the 50% silicon anode versus the 75% silicon anode. We hypothesis that the extra graphene oxide may have blocked pore passageways which are necessary for transport of lithium ions by diffusion.

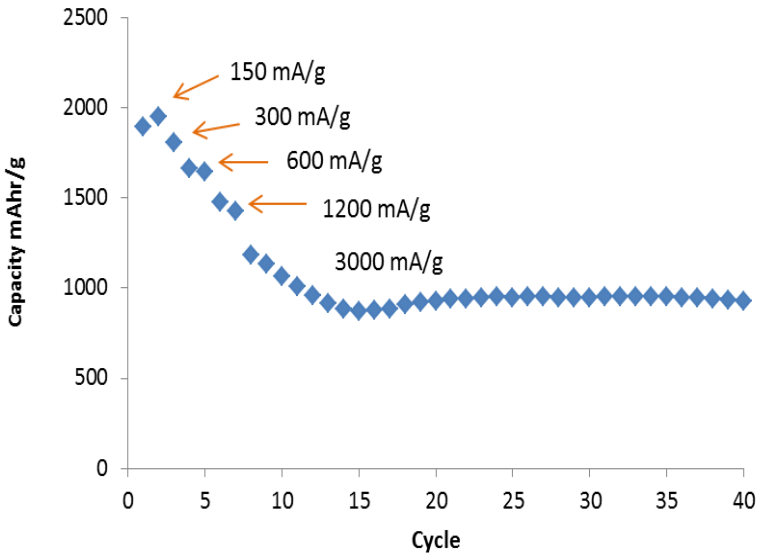

Figure 21: 75% Silicon HGOM-Si anode cycling data. The figure shows that at the current densities of 150, 300, 600, 1200 and 3000 mA/g the discharge capacities are 1951, 1807, 1645, 1429, and 947 mAh/g respectively Initial rates are 2 cycles at 150 mA/g, 1 cycle at 300 mA/g, 2 cycles at 600 mA/g, 2 cycles at 1200 mA/g, and the remaining cycles at 3000 mA/g.

Si-HGOM anodes were made with 75% silicon. The method of creating a thin free standing film without binder was used for these anodes. These were thermally reduced at three different temperatures in a quartz reactor in a horizontal tube furnace under flowing nitrogen gas with 10% hydrogen. The increased capacity and stability of these anodes is shown in **Figure 22**.

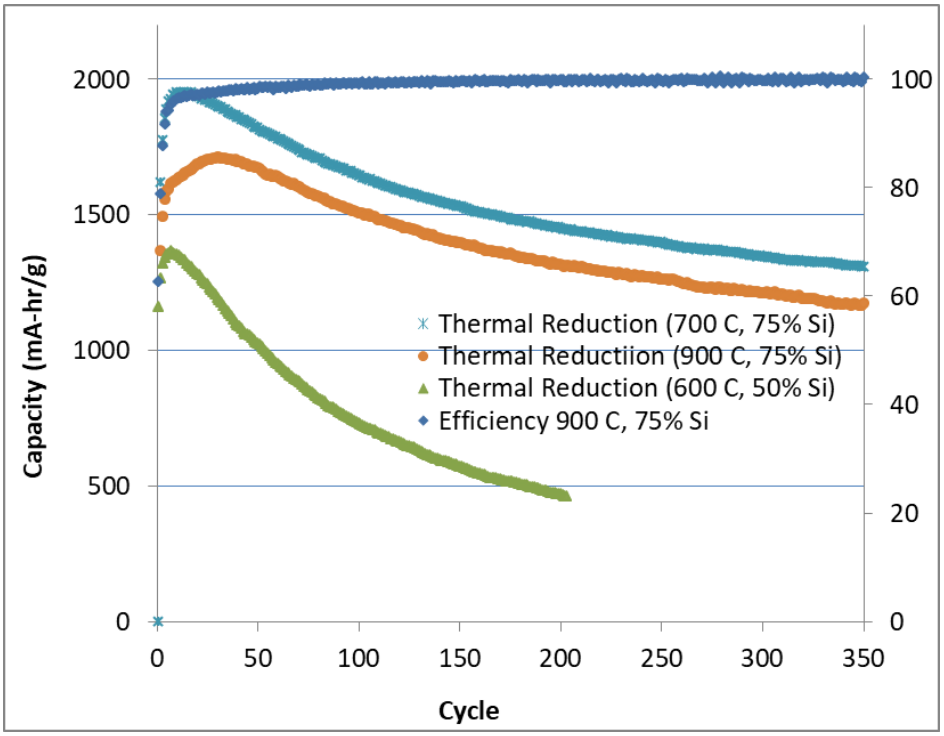

Figure 22: Comparison of free standing anodes made with thermal reduction at 600 C, 700 C, and 900 C; The anode made with 75% silicon and thermally reduced at 700 °C has in excess of 1400 mA-hr/g at 180 cycles. B) The anode made with 75% silicon and thermally reduced at 900 °C has an efficiency of approaching 99.9%.

Voltage profiles of the charge and discharge at current rates between 200 mA/g and 6400 mA/g are shown in Figure 23. The charge-discharge curves are depicted in the same color because they correspond to a fixed current indicated in the legend of Fig. 14. Typically high current rates are desirable for certain applications such as cell phones, computers, automobiles, etc. However very high currents rates cause the capacity to drop and that poses a problem. In Figure 14 we observe that for the anodes considered, when rates of charge/discharge were increased from 200 mA/g to 3200 mA/gram, 60% of the capacity of the anode remained. At 3200 mA/g, a

complete charge/discharge cycle took only 46 minutes using the constant current (cc) method of charge and discharge. These anodes were deeply cycled between 0.020 V and 1.200 V, which provides good data on the maximum capablities of the anodes, however, such deep cycling is often associated with lower stability. We note that from the data in Figure 23 that 90% of the charge and discharge occurs between 0.062 V and 0.740 V for the 200 mA/g case, and between 0.044 V and 0.850 V at 3200 mA/g.

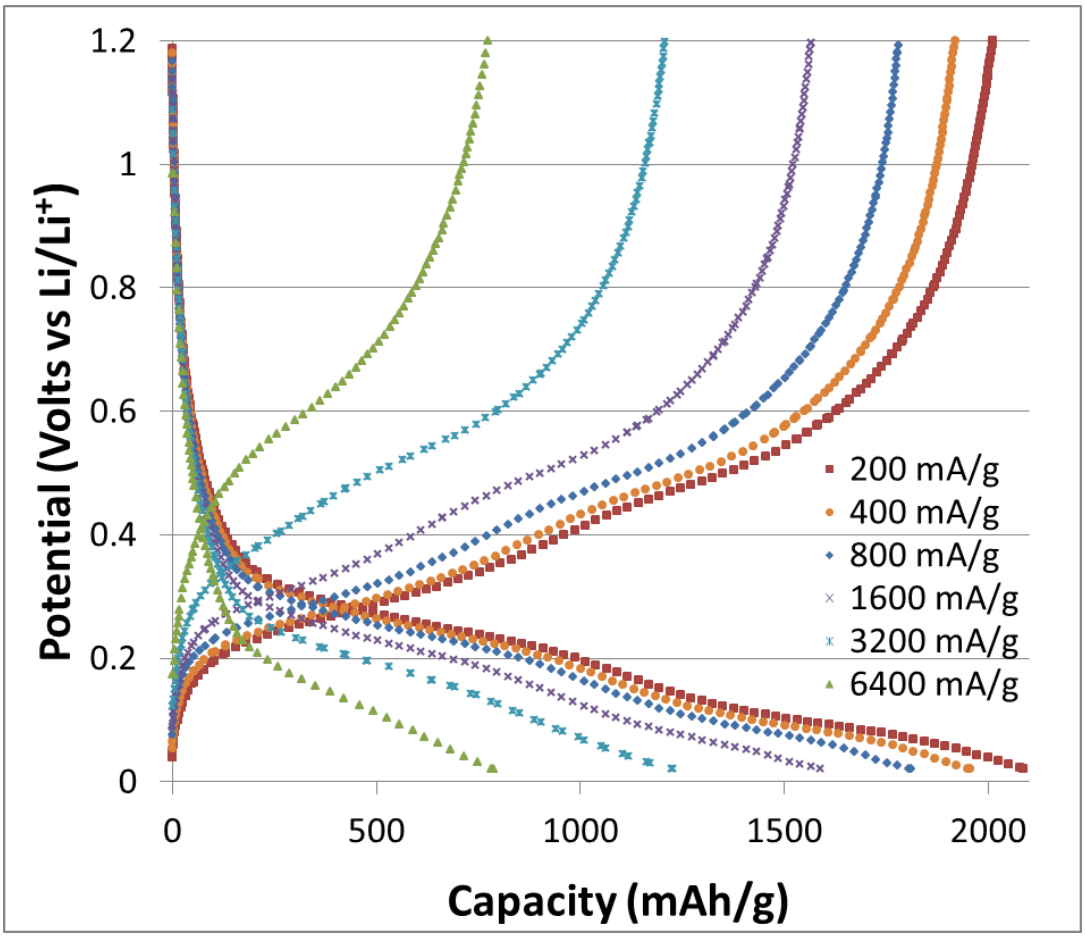

Figure 23: Constant current charge/discharge voltage profiles of the free-standing thermally reduced anode with 75% Si at various rates between 200 mA/g and 6400 mA/g.

Our approach differs from previous approaches in two significant ways. First, agglomeration is prevented by encapsulating the particles in shells. Other attempts have been able to utilize the flexibility of graphene and thin graphitic layers to accommodate the large volume changes of silicon. Impressively these experiments approached the theoretical limit of silicone over many cycles, but capacity loss eventually occurred.[29] This capacity loss is in part speculated to be the result of irreversible agglomeration as the particles redistribute themselves within the loosely packed graphene/graphitic matrix. Additionally the silicon nanoparticles appear to be still in direct contact with the electrolyte, allowing for formation and re-formation of the solid electrolyte interface (SEI layer) during cycling.

The second major difference that we propose, compared with the majority of previous studies, is that the graphene shells are be 'loosely' fitted about the silicon nanoparticles. This means that when fully lithiated the silicon nanoparticles will not completely fill (or overfill) the volume of the thermally reduced graphene oxide shells. Other attempts to wrap electrochemically active material in graphene have been successful, but not with the volumetric expansion ratio required to utilize silicon. But it would appear that such shells are unable to accommodate silicon's 300 percent expansion upon lithiation. Thus, the more desirable silicon anodes appears to be incompatible with the process of directly templating the shells upon

the silicon cores. The technique developed in this Chapter is designed to produce 'loosely fitted' shells, which will provide both containment of the nanoparticles, and the flexibility and room for volumetric expansion during cycling. This broadly applicable method will facilitate a wide choice of active materials, with the highest capacity anode material known, silicon, at the forefront of our endeavors.

We hypothesize that the SEI layer growth is confined to the outer surface of the graphene shells and not on the silicon nanoparticles. Protection of the silicon surface is necessary, since the high expansion and contraction of the silicon produces an unstable surface for the SEI formation, resulting of repeated rupture of the SEI layer upon cycling. This situation would lead to rapid buildup of the SEI polymer material. For our particles we propose that any electrolyte entering the SI-HGOM particles is expelled during the first few cycles and the particles become sealed to further electrolyte and therefor to further SEI layer build-up within the Si-HGOM particles. Another possibility is that any holes in the reduced graphene oxide shells are sealed in the first few cycles with SEI material. In this case it may be that lithium ions do not enter the interior of the Si-HGOM particles, but rather are transported from the reduced graphene oxide shells to the silicon as unreduced lithium. With successive cycles the particles (Si-HGOM) eventually become completely sealed. Therefore, lithiation and delithiation occurs by diffusion only (in and out) through the GO membranes and SEI layer. Figure 24 shows such a possibility for enhanced stability of yolk-shell anode materials.

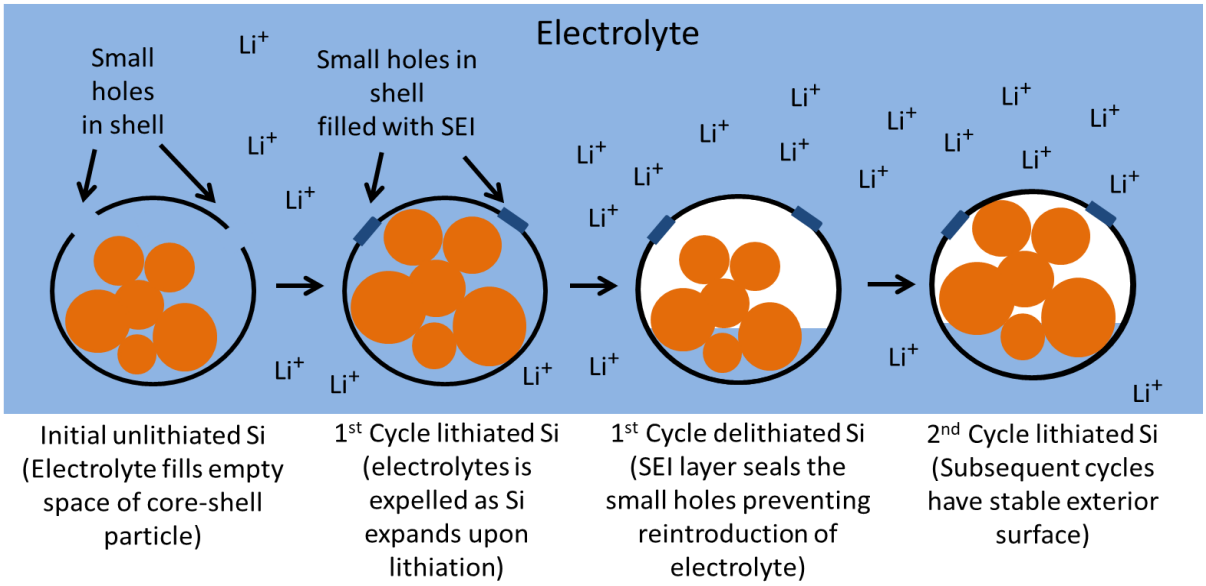

Figure 24: The shell structure enables the SEI layer to form on only the exterior of the dimensionally stable shells rather than the surface of the silicon particles which undergo a large change in surface area. Thus, repeated rupture and rebuilding of the SEI layer on the silicon nanoparticles is prevented.

4. CONCLUSIONS

Silicon nanoparticles were encapsulated in hollow graphene shells with controlled void space (yolk-shell particles, a type of core-shell particle) to form an anode with high lithium ion storage capacity. This void space appears to be critical to accommodate the large expansion and contraction of silicon as the battery cycles.

When thermal reduction (pyrolysis) was applied to the yolk shell particles, powder XRD results confirmed that the graphene oxide sheet spacing was reduced to that similar to graphite (from 2Θ of approximately 12° to 26°, indicating a reduction in sheet spacing from 7 angstroms to 3.4 angstroms). Also the powder XRD pattern

confirmed that the silicon nanoparticles remained crystalline, with a calculated diameter of 20 nm.

Yolk-shell particles with silicon inside a shell or membrane of graphene oxide were created of different average diameter depending of process conditions, such as the amount of shear apply during the emulsification-precipitation step. Yolk-shell particles with were produced diameters as large as 6 μ or a small as approximately 500 nm as determined by laser diffraction. Yolk-shell anode materials were created with silicon content between 25% and 75%, with the ideal composition of the anodes produced being 75%. Not only was the 75% silicon anode of higher capacity, it was more stable than the 50% silicon anode. It also had a much lower relative capacity reduction when cycled at high charge and discharge rates in relation to the capacity at low rates when compared to the 50% silicon anode.

Anodes made of yolk-shell particles of 50% silicon were assembled with sodium alginate binder on copper foil current collector and were either left unreduced or chemically reduced with hydrazine vapor. The first few cycles of both the unreduced and chemically anodes had nearly identical capacity (just over 1100 mA h/g), however, the chemically reduced anodes exhibited much higher stability as cycling continued.

Thermally reduced yolk-shell particles were also produced and assembled into anodes with sodium alginate binder on copper foil. At high rates the 75% silicon

anodes retained a much higher percentage of the low rate capacity when compared to anodes of 50% silicon. We believe that during the emulsion process the larger proportion of graphene oxide may lead to graphene oxide not only coating the naphthalene/silicon nanoparticle cores, but also might lead to graphene oxide also plugging the pores spaces around the yolk-shell particles, thus reducing the transport of lithium by diffusion into the entire depth of the anode. This effect might be solved by reducing the graphene oxide lateral sheet size for lower silicon content anodes, since small sheets of graphene oxide would be less able to bridge the pores on the outside of the yolk-shell particles.

We also produced free-standing electrodes (with no binder, conductive additive, or copper foil current collector). These electrodes were thermally reduced at 600°C (50% silicon), 700 °C (75% silicon), and 900 °C (75% silicon). Thermal reduction of these free-standing anodes appears to be more stable than anodes made through chemical reduction, and they also have improved capacity since there is no need for binder. These anodes also have superior cycling stability compared to anodes made with through thermal reduction and assembled with binder on a copper foil current collector.

A free-standing electrode, thermally reduced at 700 °C (75% silicon), exhibited a storage capacity of 1450 mA h/g after 200 cycles and greater than 1300 mA h g-1 after 350 cycles. Capacities greater than 1200 mA-hr/g were possible at a current of 3200 mA/g for an anode thermally reduced at 700 °C. A free-stand anode

thermally reduced at 900 °C (75% silicon) also exhibited a storage capacity nearly as high as that produced at 700 °C, with slightly improved cycling stability. The coulombic efficiency of both the anodes produced at 700 °C and 900 °C rapidly rose as cycling continued, eventually reaching 99.9%. By comparison the anode thermally reduced at 600°C (50% silicon) did not cycle with as much stability compared to those produced at 700 °C and 900 °C.

The excellent capacity and cycling stability is likely due to several advantages of these composites include: (1) graphene provides a highly conductive graphene matrix with high surface area allowing for intimate contact with silicon allowing a path for electrical contact with the silicon particles; (2) expansion and contraction of the silicon nanoparticles (which occurs during lithiation and delithiation) is accommodated due to the yolk-shell structure of the composite particles with engineered pore space; (3) fully encapsulating the electrochemically active material allows for the SEI layer to build on the stable graphene surface, rather than the ever-changing state of the silicon nanoparticles inside; (4) The pore spaces around the yolk-shell particles allow for rapid diffusion of lithium ions throughout the depth of the anode, maintaining high capacity of the anode and high charge and discharge rates; and (5) incorporating the silicon inside the shells prevents agglomeration of the silicon nanoparticles as the anode material is processed as a liquid suspension.

5. ACKNOWLEDGMENTS.

We acknowledge funding from the United States Department of Education, Grant Number P200A090356 Graduate Assistance in Areas of National Need (GAANN). The authors wish to acknowledge and thank Dr. Thomas Emge for assistance with the XRD data.

Chapter 4

Hierarchical Structured Foams: Ordered Lightweight Foams With High Surface Area

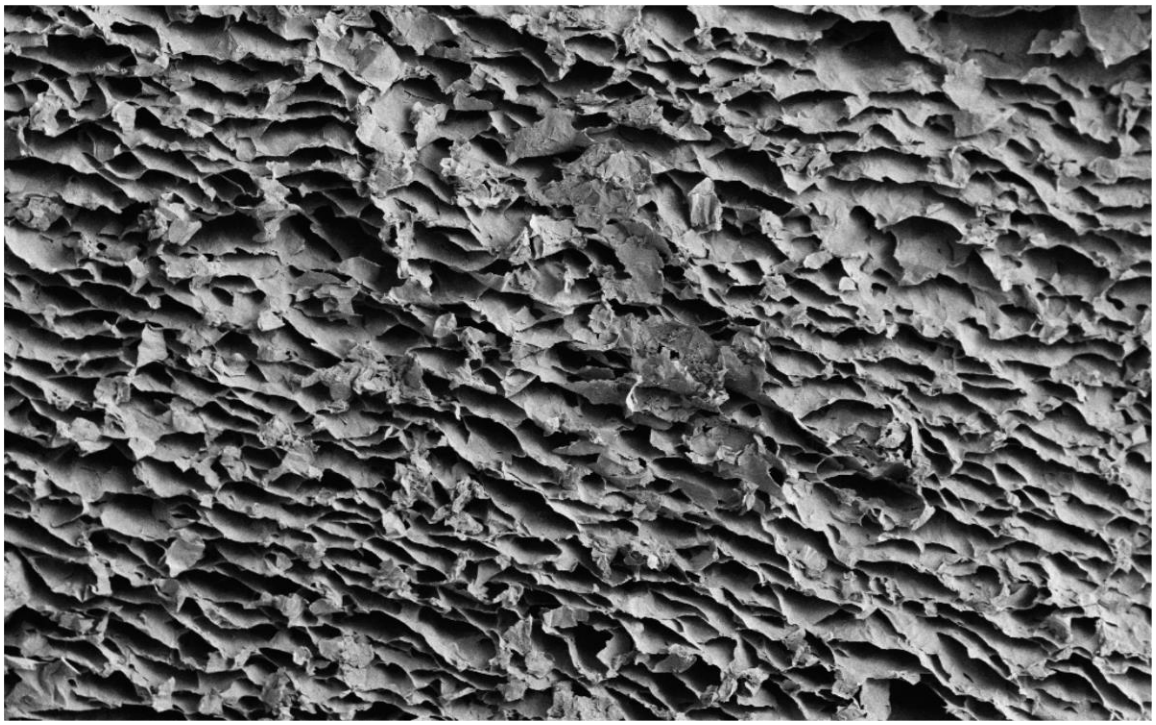

CHAPTER 4: Hierarchical Structured Foams: Ordered Lightweight Foams With High Surface Area

Part of the data in this chapter has been published:

International Patent (Patent Cooperation Treaty) Application Number: PCT/US2017/035208, publication number WO2017210289A1, published 2017-12-07 (Applicant: RUTGERS, THE STATE UNIVERSITY OF NEW JERSEY [US]. Inventors: TOMASSONE, Maria, S., and SMITH, Kurt, B.). Also part of the data in this chapter has been published (all with named inventors as TOMASSONE, Maria, S., and SMITH, Kurt, B.) in publication number CN109562933 (China [PRC] – from application number CN201780045866.6A) and in publication number US20190326592 (United States – from applications US201662343480P and US62/343,480).

AIM 3: To develop Hollow Graphene Oxide Membranes (HGOM) reinforced cryogel foam composites utilizing the platform developed in Aim 1 in combination with conventional materials.

1. INTRODUCTION

Much recent work has focused on ordered porous materials with structural hierarchy. However, even after much optimization, a well-known and very significant drawback to actual utilization of these materials is that they are typically very fragile.[71,72] Both graphene oxide membranes and graphene membranes possess high specific tensile strengths exceeding both buckypaper (paper made from carbon nanotubes) and A36 mild steel (2 ½ to 5 times higher), while the specific modulus of elasticity of graphene oxide and graphene membranes exceeds buckypaper and is nearly equivalent to that of steel.[73,74] Graphene oxide therefore, have an obvious potential to increase the resiliency

and strength of organic cryogels. Additionally, graphene oxide can easily be reduced to highly conductive graphene, a valuable attribute in electrical and electrochemical applications such as supercapacitors and lithium ion batteries.[75] In the literature, some recent attempts have been made to incorporate graphene into aerogels with very promising results.[76,77]

Ordered porous materials with a structural hierarchy have interconnected mesopores and macrospores in which the channel width is controlled over a wide range of length scales, and in some cases the channel orientation is directionally controlled as well. Such systems have enhanced properties including the ability to obtain a high surface area due to the inclusion of micropores and mesopores, while having enhanced transport properties due to the interconnecting macropores.[78-80] Some of these materials have directionally oriented channels on the order of microns or tens of microns, which allow for diffusive and even possibly convective transport depending up on the application. This chapter focuses on the development of methods to produce such materials by templating 2-dimensional materials into intricate 3-dimensional foams. This approach differs from other approaches since removal of the template is facilitated by sublimation. By removing the templating material this way, the intricate details of these structures are retained with high fidelity, and exceptional lightweight materials may be produced.

The specific goals of this chapter are to:

1) produce graphene oxide and binder based foams with an emulsion method,

2) characterize the foams by surface area, pore size, SEM, Raman spectroscopy, density, and X-Ray Diffraction.

3) explore the ice segregation-induced self-assembly of graphene oxide and resorcinol-formaldehyde based foams.

Previous Work and Novelty of Our Work:

Several workers have worked on the synthesis of foams using graphene oxide [81,82,83,84, 85, 86,87,88,89]. For example, He et al [84]synthesized foams with a composite of graphene oxide foam coated with bismuth oxyiodide (GOF–BiOI) at room temperature using an in-situ deposition approach. In the composite, BiOI flake arrays stand vertically and uniformly on the surface of GOF. There have other attempts at creating porous structures through Pickering emulsions [90,91]. For example Pan et al produced macroporous foams from lignin-based Pickering emulsions by adding toluene under high speed stirring to a continuous phase consisting of water, lignin, and urea-formaldehyde monomer. After polymerization of the urea-formaldehyde monomer, the resulting particles were washed with ethanol to remove the toluene leaving porous structures.[91] Zaijun et al [92]obtained Poly(styrene-co-methacrylic acid) (PS-co-MAA)particles via surfactant-free emulsion polymerization and then used as particulate emulsifiers for preparation of Pickering emulsions. They synthesized polystyrene (PS) foams via polymerization of Pickering high internal phase emulsion. Yu and coworkers[93] produced silica foams and functionalization of pore surface with an interfacial sol–gel reaction within high internal phase emulsion (HIPE) micro-reactors, where a hyperbranched

polyethoxysiloxane was used as the sole stabilizer for the HIPEs. However, none of the methods published in the literature attempted to create internal structures comprised of graphene oxide membranes. Our approach to creating higher-order structures is to create graphene based membranes incorporated into lightweight foams in which the final processing step is through a cryogel type sublimation. In this work we develop novel lightweight composites, comprised of Hollow Graphene Oxide Membranes (HGOM) in a light weight foam matrix to create an entirely new breed of engineered materials with high specific strength, high resiliency, and tunable transport properties.

The novelty of the work is the development of a new experimental technique that considers ultra thin membranes glued together with controlled pores structure after sublimation of the core of the constituent particles. These bonded ultra-thin membranes (HGOM) form a macroporous structure or foam with enhanced properties. Many composite aerogel and cryogel systems have been studied. However, systems which allow for controlled placement of thin graphene oxide membranes have not been described in the literature. To the best of our knowledge, this technique has never been reported in the literature before.

BACKGROUND AND LITERATURE SEARCH

One of the goals of this aim for our fabricated foams is to obtain structures with a very high surface area to be utilized, for example, in catalysis, supercapacitors, chemical reactions, lithium-ion batteries, and drug loading.[94-97] A crucial aspect of

obtaining a high surface area is to control the pore structure of the material. In what follows we will give a brief background and literature search about foams, their pore structure and the preferred pore size or mixtures of pore sizes optimal for high transport rates and high flux rates.

1.1 Foams

Solid foams are solid lightweight materials[71,72], with high pore space, and predictable properties due to their cellular structure, (i.e. Solid materials formed with gas filled voids such as bubbles). The cellular structure of engineered foams is uniform on length scales much larger than the length scales of the cells themselves, thus leading to is uniform properties at large length scales.[98] Typically such solid foams can be classified as being either closed cell or open cell; the latter is sometimes referred to as reticulated foams, meaning they have a network structure in which the pore space is interconnected. Both open and closed cell foams can be used for applications such as thermal insulation or acoustic dampening. In principle, foams can be made from various materials, including polymers, ceramic, or even metal.[99,100]

Foams including the familiar closed cell polystyrene foam (Styrofoam) and polypropylene foam, which is often used in packaging for high value goods which might be susceptible to damage.[101] Such engineered closed cell materials have applications in aerospace due to the light weight nature and relative high modulus

of elasticity of the foams. Their closed cell, water tight nature, is also utilized in floating docks for buoyance, exterior below grade building insulation, and even more humble applications such as food containers. Open cell foams are also used in numerous applications such as acoustic insulation, furniture and mattresses, and other applications in which high compressibility and/or the ability to absorb impact energies is desired without damage to the foam material.[102,103] Additionally, open cell foams are useful in other applications, in which the interconnected pore structure is important.[97]

1.2 Structural Hierarchy and Void Space

When structural elements that make up a solid have internal structure themselves, this is known as structural hierarchy. Structural hierarchy can even give rise to emergent properties, sometimes unexpected properties, such as materials with negative Poisson's ratio, even though the underlining materials do not have such properties.[104,105] Such structure affects virtually every physical property, including strength, surface area, heat flux, and fluid flow.[106] In fact, structural hierarchy is common and contributes much to the utility of many natural materials such as wood, tendon, bamboo, and bone.[107] Engineering is just at the beginning of the effort to order matter in an engineered way at the micro, meso, micron, and millimeter scale. In the cases of catalysis, electrochemical (e.g. batteries), and electrophysical processes (e.g. supercapacitors) such structures can greatly aid

these processes, and such complex structures can be referred to as transport hierarchy.[108 109]

However, it can be difficult to control all structures across a wide range of scales in the same process or material. Common to many of these methods is the fact that the formation of many of these internal structures are controlled by thermodynamics and kinetics, which makes tuning these materials in an engineered way challenging. These so called bottom up approaches, which assemble materials atom by atom, cannot directly create macropores, in the same way they create micropores and mesopores.[110]

The specific characteristics of void space are very important for any porous material in which chemistry occurs.[111] Many applications of catalytic materials require the careful structuring of nanostructured and macrostructured materials. While micropores (pores <2 nm) may provide high surface area, the transport rates are much lower than for mesopores (pores with diameters between 2 and 50 nm). This is especially important for electrocatalytic processes and for electrochemical processes, since ion mobility is likely to be rate limiting as the pore size decreases. For pores with diameters ~1 nm, the diffusion rate of ions is several orders of magnitude lower than in the bulk liquid, which means electrocatalytic transport process in microporous material may occur at different time scales than mesoporous materials.[111,112] Further complicating the issues is that, even for larger pore sizes, blockage can disrupt transport if the pores are not connected into a

network to allow for three dimensional transport around such blockages.[111] So our challenge is to create materials with a broad range of pore sizes.

1.3 Aerogels and Cryogels

Aerogels and cryogels are very light weight nanofoam materials which typically have remarkably high surface area and thermal insulating properties. These materials (aerogels and cryogels) are made from gels which are set through chemical reactions in which the liquid is subsequently replaced by air, by two different fundamental means. If simply evaporated, these gels tend to collapse due to the internal forces created by liquid surface tension on the very high surface area within the gel structure. Aerogels circumvent the creation of a liquid-vapor interface (and the associated surface tension) by using high pressures (above the critical point pressure) and then increasing the temperature above the critical point, after which, the vapor may then be removed. (Above the critical point temperature there is no liquid-gas transition phase.) Cryogels circumvent the creation of a liquid-vapor interface by freezing the liquid and then subliming the frozen liquid within the frozen gel at temperatures below the melting point.

Because of their high thermal resistance these lightweight materials are natural candidates for insulation in aerospace and for other applications in which either space or weight are limited. Research has shown that lightweight carbon based foams are promising materials for hydrogen storage,[113,114] pseudocapacitors,[115,116]

lithium ion batteries,[117] catalysis,[118] electric double layer capacitors (EDLC),[72,119,120] also called 'supercapacitors', and nanoconfined hydrides for energy storage.[121] In addition to the direct use as capacitors for energy storage, the electric double layer effect can be applied to the related applications of capacitive desalination[122] to produce fresh water from brackish, and the harvesting of renewable power from the mixing of river water with sea water via osmotic power production using the capacitive method.[123-126] (The capacitive method of power generation, is a new alternative to reverse electrodialysis and pressure-retarded osmosis, both of which have struggled to economically harvest this vast source of renewable energy.) Additionally, carbon based foams are also used in a variety of applications, including as a matrix for phase change material for thermal heat management,[127] and electromagnetic interference shielding. [128]

1.4 Hollow Graphene Oxide Membrane (HGOM) Foams

In this work we use different types of resins or binding agents to produce HGOM foams: (i) resorcinol-formaldehyde (RF) resin, (ii) an amine cross-linker or an epoxy resin.

(i) The first system we explore is hollow resorcinol formaldehyde-graphene oxide membrane (HGOM-RF) foam. Resorcinol-formaldehyde (GO-RF) chemistry is reportedly able to covalently link graphene oxide sheets with high strength.[129] In work by Worsley et al, resorcinol-formaldehyde was mixed with graphene oxide to form '3D graphene assemblies' using traditional organic sol-gel chemistry.[129] In that

work, graphene oxide was gelled with resorcinol-formaldehyde and dried with supercritical carbon dioxide in the traditional aerogel method. Other work by Yu el al, has more recently incorporated graphene oxide into composites using a freeze drying method (which does not produce channels in the foam).[130] In all cases, no attempt was made to introduce HGOMs or other such elements to the foam. For our purposes, any resorcinol-formaldehyde (RF) not directly bound to the graphene oxide (GO) may also contribute additional properties which are known to be characteristic of RF aerogels/cryogels, including a low density mesoporous structure with high specific surface area.[122,131] Additionally, these structures may be thermally reduced allowing the combined properties of these materials to be utilized for electric double-layer capacitors (EDLC) also known as supercapacitors, for lithium ion batteries, and potentially other applications. There are several key issues to make this selection of materials particularly usefully for energy applications. In lithium ion batteries, graphene has been particularly invaluable in accommodating the volumetric changes of electrochemically active materials, yielding both high power and high cycling stability.[29,132] For supercapacitors, graphene's theoretically high double layer capacitance of 550 F/g exceeds other carbon based materials, and per unit weight is the highest known.[133] We explore activation of RF-HGOM nanofoams to increase the surface area, the first step in utilizing these materials for EDLC and a number of other applications.

(ii) In addition to using resorcinol-formaldehyde, we also create foams only adding a cross-linker (triethylenetetramine hydrate) which can covalently bond to the

epoxide groups on the graphene oxide sheets, thus binding them together.[134] Since, triethylenetetramine has more than one active group it has the potential to bind two adjacent graphene oxide sheets together. Additionally, it is possible to add additional components to the cross-linker (e.g. 1,4-butanediol diglycidyl ether) to form a resin which not only can cross-link graphene oxide sheets, but could potentially fill in spaces between the sheets in a manner similar to resorcinol-formaldehyde resin.

Such materials have potential applications as acoustic insulation in aircraft and as thermal insulation in applications where space is limited. This higher order structure made of strong graphene oxide has the potential to reinforce these fragile materials making them useful in many additional applications, perhaps even as core materials, replacing the familiar honeycomb webbing in reinforced panels for aerospace. Aircraft weight reduction has the potential to increase fuel efficiency of passenger and cargo transport.

Additionally, these thin and ultra-thin graphene oxide membranes naturally have high surface area. This high surface area makes them ideal for the creation of aerogel and cryogels as the active material in supercapacitors (EDLC). Supercapacitors have specific power about one order of magnitude larger than conventional batteries (lithium-ion or nickel metal hydride). This has potentially great weight, cost, and energy savings in many important applications, such as hybrid electric vehicles.

The advantage of the cryogel system (via sublimation) is that it does not require high pressure equipment while simultaneously it can provide exceptional properties, including highly porous structures with high transport rates and mechanical strength. (Aerogel systems often require precisely controlled pressures above 1071 psi for many common applications).

1.5 Ice-Templated Materials

Ice formed channels were first reported in 1980 for freeze-formed silica fibres.[135] Since then, ice-segregation-induced self-assembly, as it has sometimes become known, has evolved to produce structures which have organization at multiple scales, from the nano to micron in size.[136] Such directional channels can be formed by freezing colloids / sol-gels.

We expanded the ice-segregation-induced self-assembly technique for a new material: resorcinol-formaldehyde and graphene oxide composites. To the best of our knowledge this has not been reported in the literature before. In the case of the resorcinol-formaldehyde – graphene oxide (RF-GO) sol-gel, the reaction is allowed to proceed to the point that the sol-gel is still somewhat deformable but also somewhat rigid. At this point the sol-gel is still capable of plastic deformation as the channels are formed through the freezing process, but it has hardened just enough

and is rigid enough to retain the shapes imposed by the ice crystals after they have melted.

Of particular interest is that transport properties can be enhanced directionally, indeed some of the structures formed look on the microscale like miniature solid catalysts used for engine exhaust treatment. Such structures naturally lend themselves to process in which both convective and diffusive transport is required. However, these properties can even potentially improve transport properties for lithium-ion batteries.[137]

In this dissertation we will utilize an ice-templating method to synthesize foams. Specifically, in this chapter we will develop two different methodologies to create structural hierarchical foams with pores across a wide range of scales, from the less than 1 nm to more than tens of microns. The two selected methods are the following:

1) ***Synthesis of foams created by self-assembly of HGOM using different resins or binding agents.*** Within this method we consider different resins or binding agents: 1) resorcinol-formaldehyde (methods described in section 4.2.2) and 2) amine cross linked (triethylenetetramine hydrate) as well as epoxy resins using triethylenetetramine hydrate and 1,4-butanediol diglycidyl ether (methods described in section 4.2.3) These approaches utilize the materials (HGOM) developed in chapter 2 of this dissertation to create

rigid foams with interconnected pores created by 'gluing' the HGOM particles with different binding agents. The HGOM resorcinol-formaldehyde was tuned through systematic changes in the chemical activation agents (such as the amount of KOH) to achieve high surface area, and useful distribution of mesopores and micropores.

2) ***Synthesis of foams created through ice segregation induced self-assembly with micron size channels.*** These ice templated materials can be used for transport of fluids through those channels in catalysis or microfluidics. In ice segregation self-assembly, we were able to obtain channels widths from 5 to 30 μm. We varied the concentration of GO to Resorcinol-Formaldehyde and observed that the higher the GO concentration, the less organized the channels become, and the less parallel they set. More studies need to be made to elucidate the factors that control the size of the channels.

In the remainder of the chapter, we detail the experimental methods and results, focusing on how we incorporate higher order structural elements (microspheres) to act as reinforcing elements for these foam materials with high specific surface area. With control of properties of the membranes and composite polymer chemistry, we tune the surface area.

2. EXPERIMENTAL METHODS AND MATERIALS.

2.1 Summary of the Materials.

Resorcinol, formaldehyde (formalin), sodium carbonate, triethylenetetramine hydrate (98%) %) [also known as TETA or trien] and 1,4-butanediol diglycidyl ether (95%), glacial acetic acid, dichloromethane, and hexane were purchased from Sigma-Aldrich and used as received. Polytetrafluoroethylene (PTFE), 1 μm diameter, particles were purchased from Sigma-Aldrich and washed with dichloromethane and hexane and dried prior to use. Graphene oxide was synthesized through a modified Hummers method developed by Kovtyukhova and others.[26,55] In this process we used natural flake graphite (grade 230U) donated by Asbury Carbons (Asbury, NJ and Kittanning, PA). The graphene oxide was then washed 10 times with DDI water. The exact details of the synthesis and characterization are detailed in Chapter 2 of this Dissertation. Ultra-high purity distilled deionized water was proved by the Millipore system and used as the source water throughout.

2.2 Preparation of HGOM-RF materials using emulsion precipitation

Naphthalene templated graphene oxide membranes and resorcinol formaldehyde (RF) chemistry: Graphene oxide templated membranes are washed with DDI water on a Buchner funnel to remove any additives used in processing the template membranes (such as acetic acid used to adjust pH). Resorcinol and formaldehyde are mixed in a 1:2 molar ratio with sodium carbonate catalyst (with a Resorcinol to catalyst molar ratio of 200:1). The pre-gelled mixture is aged for a period of time at

room temperature to nucleate the sol-gel, but short of producing a gelled material (e.g., 20 percent 'solids' (R + F) aged for 24 hours at 20 C). The pre-gelled mixture is added to the graphene oxide template membranes (still containing cores) and mixed. Air bubbles are removed from the mixture by centrifuging, but at accelerations (500 rpm) much below that required to concentrate graphene oxide in aqueous solutions. For mixtures in which air-entrapment is not an issue the centrifuge step is unnecessary. The mixture is place into tightly sealed glass vials and aged at temperatures below the melting point of the oil phase cores (e.g., naphthalene templated membrane based - RF foams are aged at 65 C). **Figure 25** describes the process with the oil-phase cores composed of naphthalene and the cryogel matrix material composed of resorcinol formaldehyde (RF). Resorcinol-formaldehyde has been used for a number of years by itself to produce organic aerogels and cryogels. However, this method of assembly using HGOMs is novel.

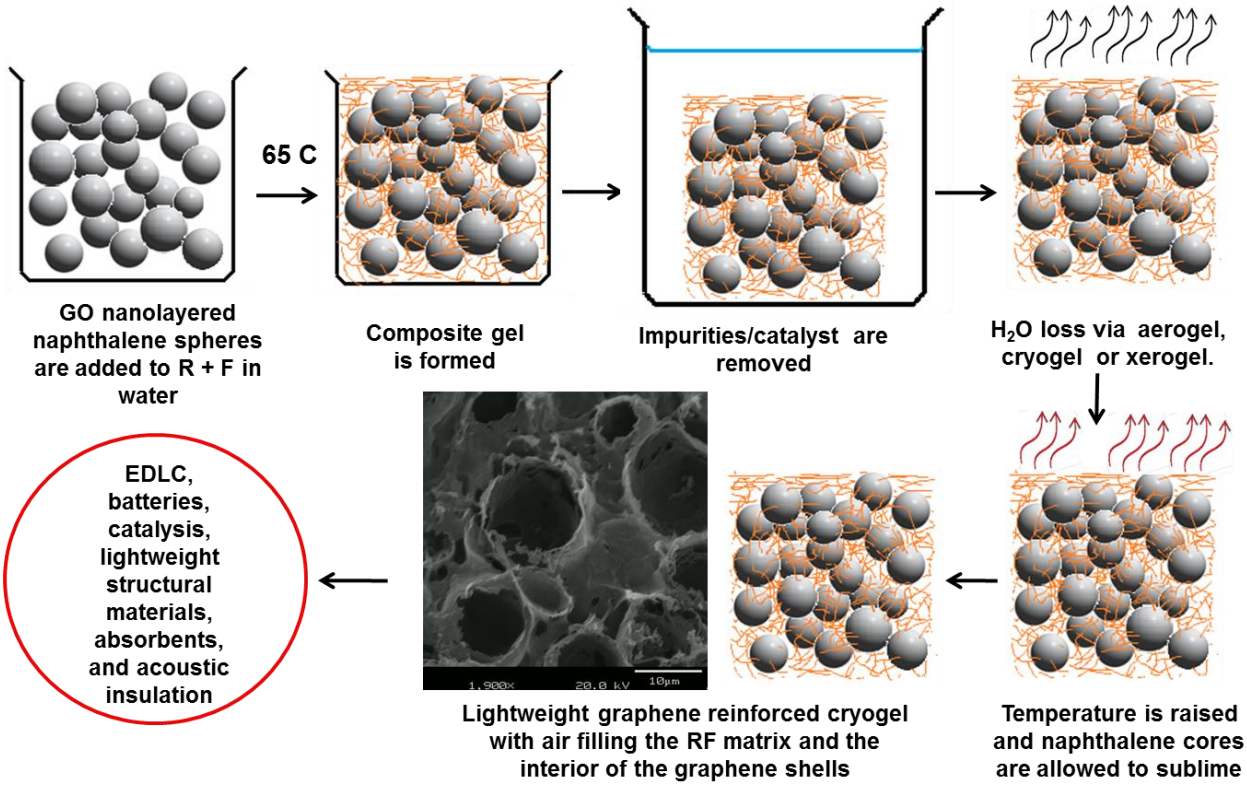

Figure 25: This schematic shows the experimental steps to produce composite RF-HGOM cryogel foam starting clockwise from the upper left corner. The SEM inset is a cross section of an actual composite showing the internal structure with hollow graphene oxide membranes.

One of the GO-RF foam samples was activated with potassium hydroxide. Activation is a well know process which partially oxidizes and roughness the surface, thus increasing the surface area. By increasing the surface area this adds additional possibilities for uses, such as, adsorption of oil allowing for easier cleanup for remediation, or potentially for use as supercapacitors utilizing the EDLC effect.

2.3 Preparation of HGOM Cross-linked Foams and HGOM-Epoxy Foams

The procedure shown in the figure above was modified to include additional chemistries. An amine base cross-linker. triethylenetetramine hydrate, was added at the rate of 2 wt% to the concentrated HGOM particles to produce a solid foam. For a water based epoxy formulation: triethylenetetramine hydrate (98%) [also known as TETA or trien] and 1,4-butanediol diglycidyl ether (95%) was mixed in a 3:1 molar ratio which will provide a molar 1:1 ratio between amine protons and epoxide rings. A similar ratio was proposed for clay based aerogels in 2007.[138] The general procedure is similar to that described above for GO-RF gels.

Engineering these structures to control the pore space has the potential to enhance transport properties within the nanofoam, achieving a better balance between the competing requirements of high surface area and high transport rates. There are many ways to achieve *hierarchically porous structures*, however this system requires no additional sacrificial scaffolds, other than naphthalene (or other oil-phases) which can easily be recycled.

2.4 Preparation of GO-RF ice segregation induced self-assembly samples

Graphene oxide with Resorcinol-formaldehyde resin samples were prepared with different ratios of graphene oxide to resorcinol-formaldehyde. As with the case of hollow graphene oxide particles, resorcinol-formaldehyde acts to chemically form bonds with graphene oxide platelets and bind them together. The liquid sample mixtures were poured into polyethylene tubes. The samples were allowed to cure

at 65 °C into a hydrogel which retained its shape when cut, but was still plastic (deformable under pressure). Then the sample was treated by freezing in liquid nitrogen. One end of the polyethylene tube was dipped into liquid nitrogen to create a constant freezing rate (approximately 1 cm/minute), progressing directionally from one end of the sample tube to the other end. Internal channels were created by the growing ice crystals while the GO-RF hydrogel was still deformable, but not fully hardened. After thawing the samples were then aged at 65 °C to allow the resorcinol-formaldehyde resin to completely harden. The sample remained sealed to prevent evaporation throughout this process.

The sample was dried via the cryogenic method of t-butyl alcohol replacement and sublimation. This involved adding the sample to excess t-butyl alcohol and replacement of the t-butyl alcohol twice per day for two days. The sample was refrozen and since liquid t-butyl alcohol and frozen t-butyl alcohol have remarkably similar densities, little strain is placed upon the internal structures of the foam samples during the freezing process. (This step would be unnecessary, except for very low density foams, as simple drying would be sufficient.) After freezing the samples which have the aqueous phase replaced by t-butyl alcohol, they were dried at 10 °C under flowing air.

The SEM samples were prepared by cutting the frozen samples and then subliming the t-butyl alcohol under flowing air at 10 °C. SEM imaging itself was completed at 20 °C; additional details of sample preparation are included in section 4.2.5.2 of this

dissertation. The basic steps are described in **Figure 26**, except for the t-butyl alcohol replacement and sublimation method.

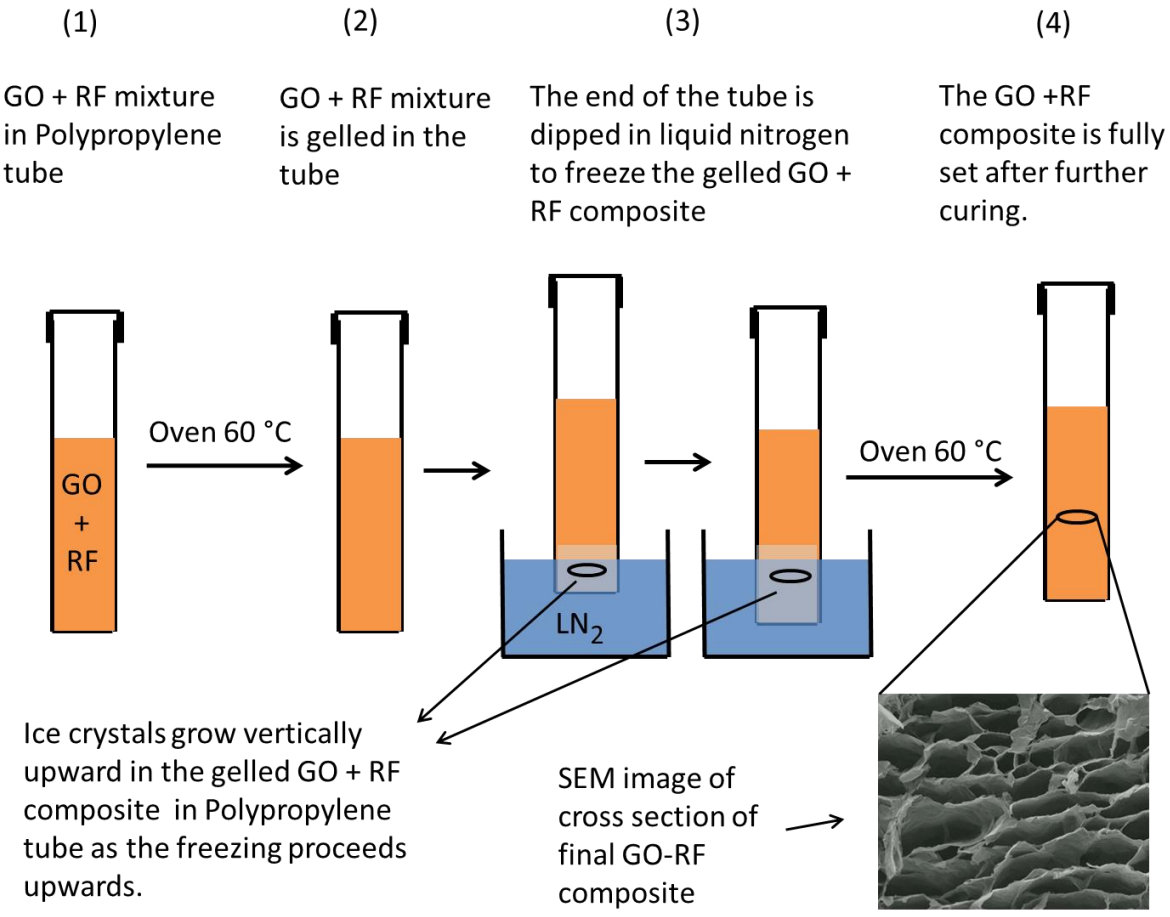

Figure 26: Schematic diagram of the process used to create graphene oxide resorcinol-formaldehyde ice segregation induced self-assembly materials. (1) A GO and RF mixture was made with a specific concentrations of GO and RF solids. (2) Then the mixture GO and RF was partially reacted to form a 'gelled' semi-solid material. (3) Freezing in liquid nitrogen promotes the growth of ice crystals in the direction of the freezing, forming micron sized channel vertically. (Note that it may be necessary to dip the polypropylene tube deeper into the liquid nitrogen as the

process progresses to keep the growth rate of the frozen portion of the sample constant.) (4) The sample is dried via the cryogenic method of t-butyl alcohol replacement and sublimation. Finally, the light weight sample is revealed through SEM imaging.

2.5 Characterization

The graphene oxide based organic foam samples were characterized during production to determine the particle size distribution, and after production to determine structure and the final properties of the foam samples.

2.5.1 Surface area and pore size distribution

The gas-sorption measurements were obtained with a Quantachrome Autosorb 1 Gas Sorption Analyzer using nitrogen as the adsorbate with a bath temperature of 77 K. Samples for BET analysis were held at 60 °C in a double walled beaker for one day (prior to outgassing) to ensure all of the naphthalene was sublimed. The sample was outgassed under nitrogen at 150 °C for 7 hrs. From these measurements the internal surface area and pore size distributions were calculated. Traditional Langmuir and Brunauer–Emmett–Teller (BET) theories to calculate surface areas were used, which allows for direct comparison with other results in the literature. Additionally, the more recently developed, Non-local Density Functional Theory (NLDFT) was used for analysis of the pore size and pore space within the samples.

Non-local Density Functional Theory may provide a more complete analysis for these types of structures. [139-141]

HGOM particle size analysis was performed using a Beckman-Coulter LS-13 320 laser diffraction apparatus with a universal liquid module filled with distilled deionized water. A refractive index of 1.582 was used to define the naphthalene cored particles. All particle size measurements were completed on the suspensions at room temperature (approximately 21°C).

2.5.2 SEM imaging

For solid samples, SEM samples were prepared by first cutting and/or fracturing the sample to an appropriate size using a new razor blade. Some of the samples were frozen and cut and/or fractured before sublimation of the naphthalene (the samples which received this treatment are identified in the Results and Discussion Section of this Chapter). The sample was mounted to a standard SEM stub. Double-sided electrically conductive, non-porous carbon tape was applied to the mounting surface of the SEM stub, and finally, the sample was mounted to the surface using forceps. SEM images were obtained using a Zeiss Sigma Field Emission SEM. All images were obtained without sputter coating of the sample, unless otherwise indicated in the Results and Discussion Section of this chapter.

2.5.3 Density of Foam Samples

For some of the foam samples, the final cured and dry densities of foams samples were measured. To accomplish this, the foam samples were cast into round cylinders of constant diameter. The mass of the dry foam sample was measured to readability of 0.1 mg (repeatability 0.12 mg). Typical dimensions of the samples were 10 mm diameter by 50 mm length. After curing and drying of the samples, the foam cylinders were mitered perpendicular to the axis of the samples, to allow precision in the measurement of the length of the samples. Measurements of the diameter at 8 points along the cylinder were taken and the length of the sample was measured at 4 positions. The diameter and length of the sample was recorded to a resolution of 0.01 mm (10 μm) using a micrometer. The standard error, when reported in the Results and Discussion section, was propagated from the dimensional measurements and mass of the sample.

2.5.4 Raman Spectroscopy

Raman Spectrum of samples was acquired using a Renishaw inVia Raman Microscope. Imaging and spectrum acquisition was through the associated Leica DMLM microscope. A laser excitation wavelength of either 514 nm or 633 nm was used for characterization of the foam samples. The Raman spectrometer was calibrated using an internal silicon calibration reference. WiRE 3.4 software was used to calibrate and acquire the spectrum. After acquisition the spectrum was

smoothed to a resolution of 4 cm^{-1} to allow better interpretation and presentation of the data.

2.5.5 X-ray Diffraction Patterns:

A high-flux rotating anode x-ray generator (CuKα radiation at 1.54 angstroms) and a sensitive Bruker HiStar area detector were used to gather X-ray diffraction patterns. The powder XRD patterns were obtained by integrating the area detector to obtain patterns in units of 2-theta.

3. RESULTS AND DISCUSSION

Results for the foams synthesized with different methods are explained in the following subsections of this dissertation:

(i) Foams synthesized with hollow graphene oxide membrane and resorcinol formaldehyde (RF) . (4.3.1)

(ii) Foams synthesized with activated HGOM-RF materials (section 4.3.2)

(iii) Foams obtained with HGOM amine based materials (section 4.3.3)

(iv) Foams formed with ice-segregation induced self-assembly of GO-RF foams. (section 4.3.4)

3.1 Foams synthesized with hollow graphene oxide membrane and resorcinol formaldehyde (RF) foams.

First we report the results of the RF-HGOM nanofoam composites using both RF and Epoxy Chemistry to 'glue' the HGOM foam together. The graphene oxide membrane covered particles which we previously reported in the literature[55] are incorporated into a matrix and the solidified oil phase cores are removed through sublimation. This is essentially the same type of process by which the light weight structures of cryogel are retained. This produces a very light higher-order structure with graphene oxide membrane reinforcement. As described in detail in the Methods and Materials section, graphene oxide templated membranes were washed with DDI and then used to produce a HGOM-RF foam composite. Then a premixture of resorcinol and formaldehyde were mixed in a 1:2 molar ratio and catalyzed with sodium carbonate. After the pre-gelled mixture was aged for a period of time at room temperature to nucleate the sol-gel, the graphene oxide template membranes (still containing cores) were combined with the pre-gelled RF mixture and aged to form the composite HGOM-RF foams. Such materials can be observed in **Figure 27**, in which assemble of HGOM with RF 'glue' was used to produce a lightweight foam.

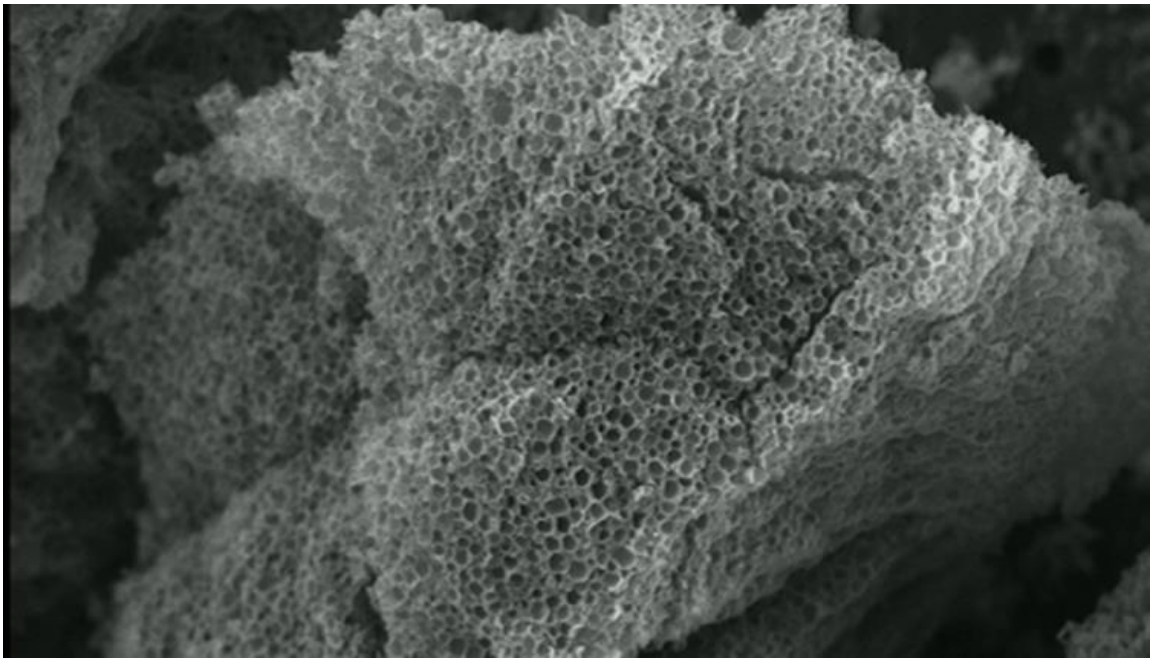

Figure 27: Sample of foam HGOM-RF in which the regular cellular structure can be observed throughout the material. This sample was made with concentrations GO 60% and RF 40%.

The starting material for making carbon based foams using this process is the HGOM particles themselves. Following the production methods in Section 2 of this chapter, the HGOM particles were imaged by light microscopy and are shown in ***Figure 28***.

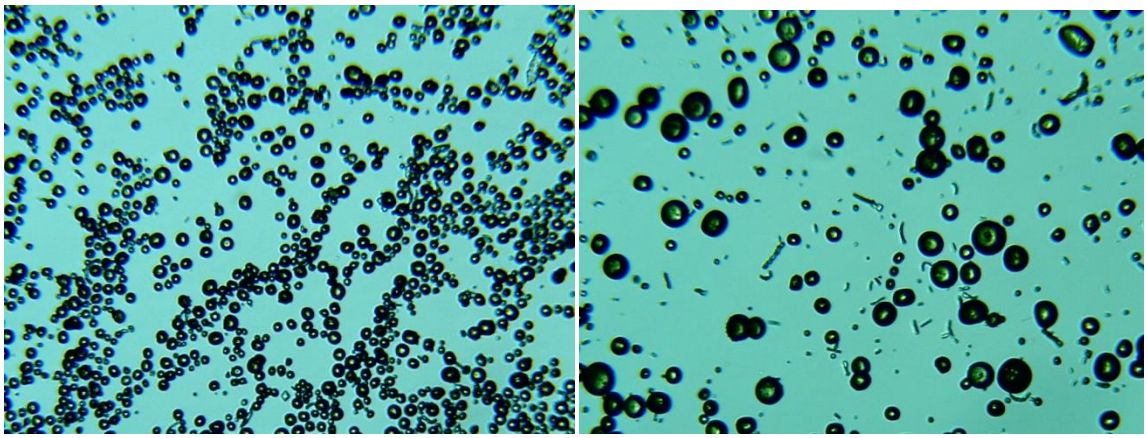

Figure 28: *Digital optical microscope images of HGOM templated on naphthalene cores. These samples were imaged in the solution in which they were made.*

Figure 29 shows SEM images from a GO-RF foam composite sample which has been cut and broken to reveal an array of closely packed hollow graphene oxide spheres which have been bound by resorcinol formaldehyde.

A detail of the HGOM – RF foam can be seen in **Figure 30**. **Figure 30a** is a RF-HGOM foam sample which was cut open with a razor blade to reveal a cross section of the sample. **Figure 30b** shows a magnification of the small orange box that is shown at the top left of the SEM image in (a)). it is the outer surface of an HGOM microsphere. Notice that the scale bar is 100 nm, so the small structures/spheres are approximately 20 to 40 nm indicative of RF foam nano-structure and are apparent only on the outer surface of the HGOMs. **Figure 30**c shows a magnification of the big orange box located at the lower center of **Figure 30**a, showing the detail of the HGOM-RF reinforced spheres. This sample was obtained with 7% GO and 93% RF. It is possible to observe that for this low GO concentration the size of the HGOM with high shear rotor stator tends to be larger reaching 3 to 8 microns. The size of the pores is approximately 3-8 microns as can be appreciated in **Figure 30**a.

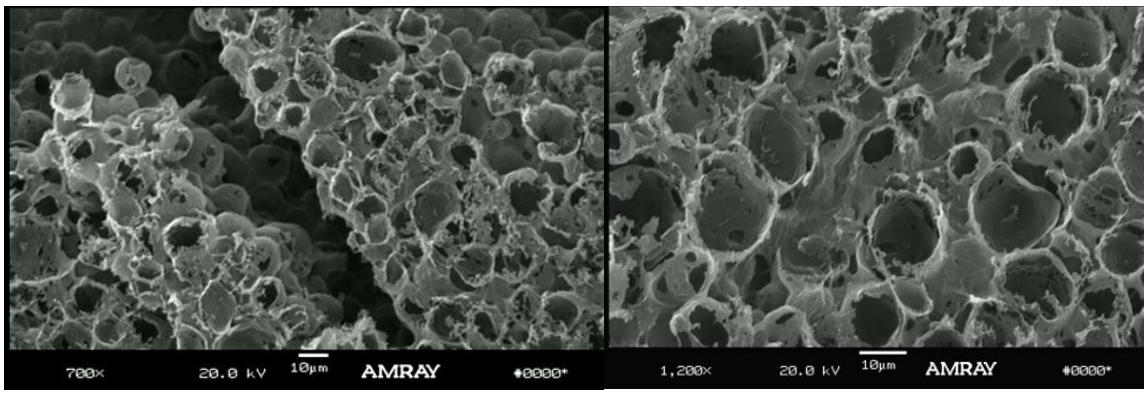

***Figure 29**: SEM images are of a HGOM-RF sample which was made with 20 mg/mL (4 mg/mL GO and 16 mg/mL RF). This HGOM-RF sample sample has been cut and*

broken to reveal an array of closely packed hollow graphene oxide spheres which have been bound by resorcinol formaldehyde.

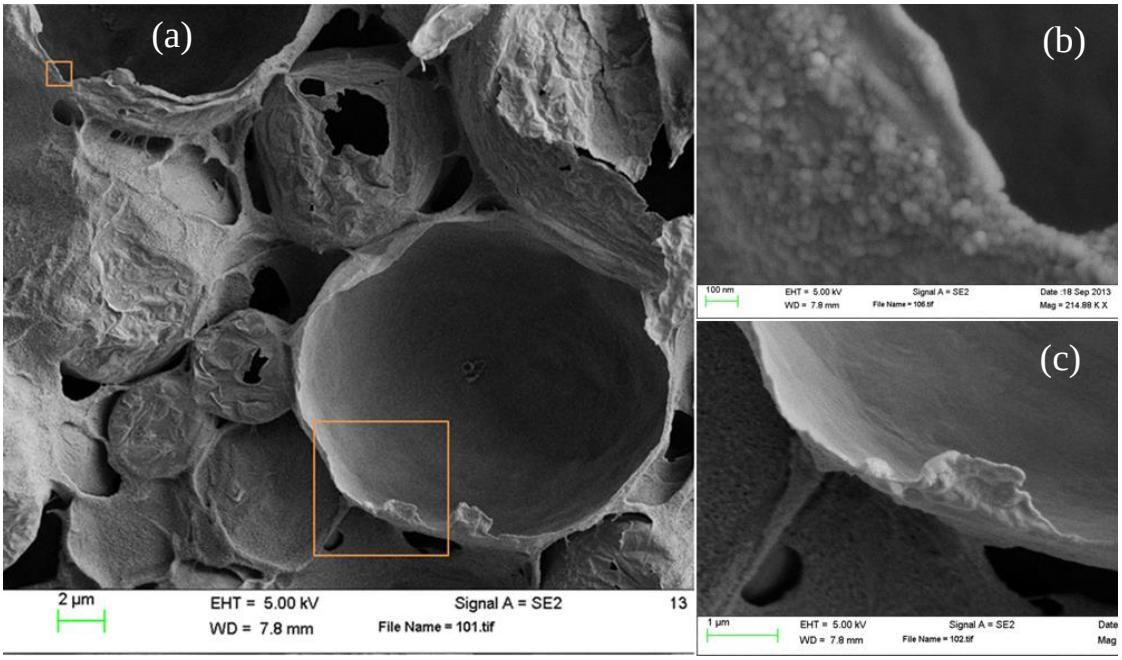

Figure 30: SEM image and detail of HGOM-RF foam sample of RF-HGOM foam 7 wt% GO and 93 wt% RF). (a) The sample which was cut open with a razor blade to reveal a mg solids (cross section of the sample. (b) Magnification of the small orange box at the upper right hand corner of picture (a) showing the outer surface of microsphere; (c) SEM image shows the magnification and detail of the large orange box located at the lower center of figure (a) Scale bars are 2 microns (a) 100 nm (b), and 1 micron (c).

We have also taken the Raman spectrum of this same sample using a laser excitation wavelength of 633 nm (Renishaw RL633 Laser, 150 mW max). The spectrum shows very similar D and G band spectrum peaks similar to the amine cross linked sample. The spectrum can be seen in **Figure 31** in which the D band of the RF-HGOM foam

sample is at 1355 (cm^{-1}) and the G band is at 1594 (cm^{-1}). We note that the D and G bands are not shifted in position with the addition of resorcinol-formaldehyde resin. Since the resorcinol-formaldehyde is still polymeric for these samples (not pyrolyzed), it has no sharp peaks that could interfere with the peak positions of the D and G bands. Some studies have indicated an extremely broad Raman peak for unreduced resorcinol-formaldehyde polymer stretching nearly the entire breadth between 700 (cm^{-1}) to 2000 (cm^{-1}) of the spectrum.[142] However, being such a broad peak, this would not be expected to shift the G and D band positions of the graphene oxide component.

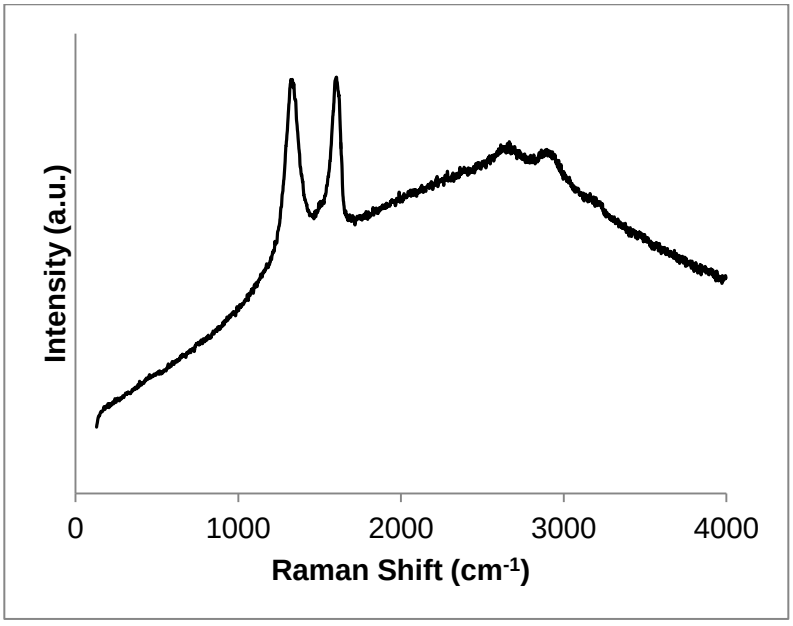

Figure 31: Raman spectrum of RF-HGOM foam sample. The D band of the RF-HGOM foam sample is at 1355 (cm^{-1}) and the G band is at 1594 (cm^{-1}). Note that this is the same Raman band positions (within 1 cm^{-1}) as those for the triethylenetetramine hydrate crosslinked carbon graphene oxide based foam sample of the previous figure.

Samples with different weights and graphene oxide content were made for comparison of the resulting structures. SEM images of the samples were acquired at several different magnifications to reveal the large scale structure and small scale structural elements of the resulting foams. We first look at three samples which have the same graphene oxide concentration per unit volume (8 mg/ml) in the initial mixture. We varied the concentration of the resorcinol-formaldehyde, producing samples which have different weights of initial 'solids'. SEM images of this series of foam samples can be seen in **Figure 32**, **Figure 33**, and **Figure 34**.

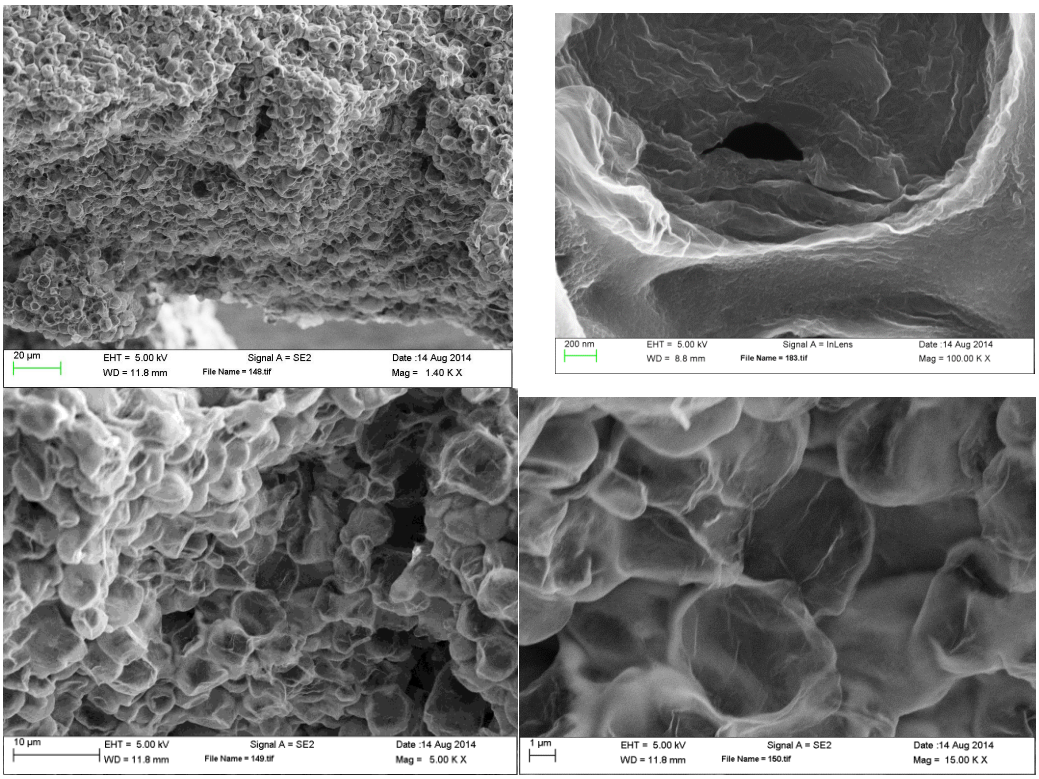

Figure 32: SEM image of HGOM/RF foam sample 40mg/mL: 20% GO, 80% resorcinol-formaldehyde. Scale bars are (a) 20 µm, (b) 10 µm, (c) 1 µm, and (d) 200 nm.

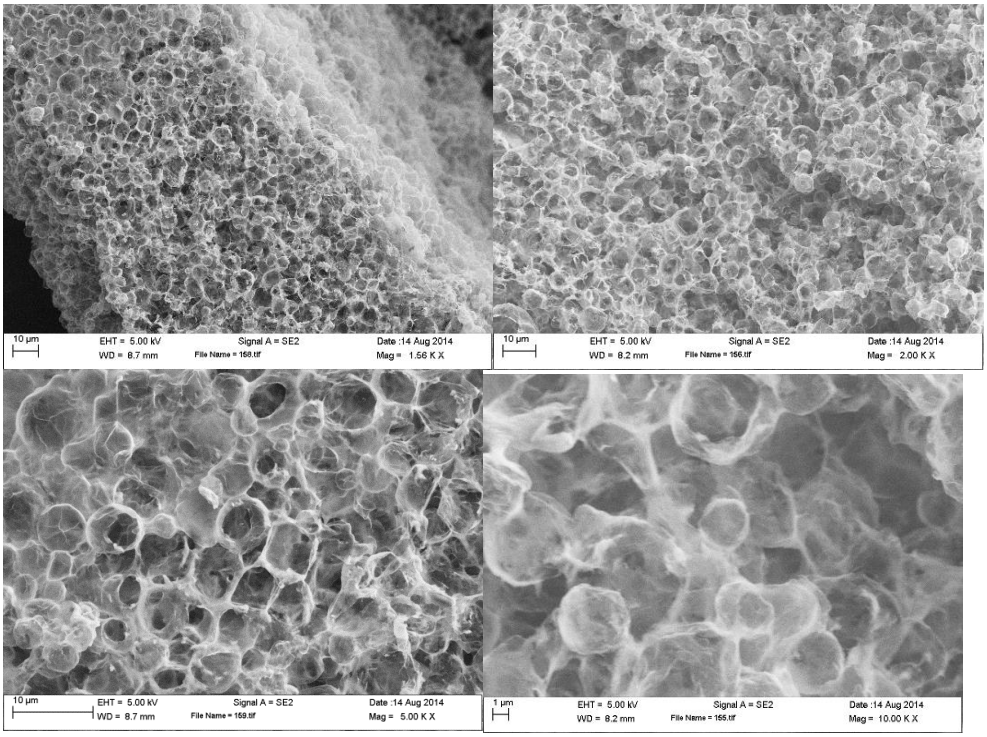

Figure 33: SEM image of HGOM/RF foam sample 20 mg/ml: 40% GO, 60% resorcinol-formaldehyde.

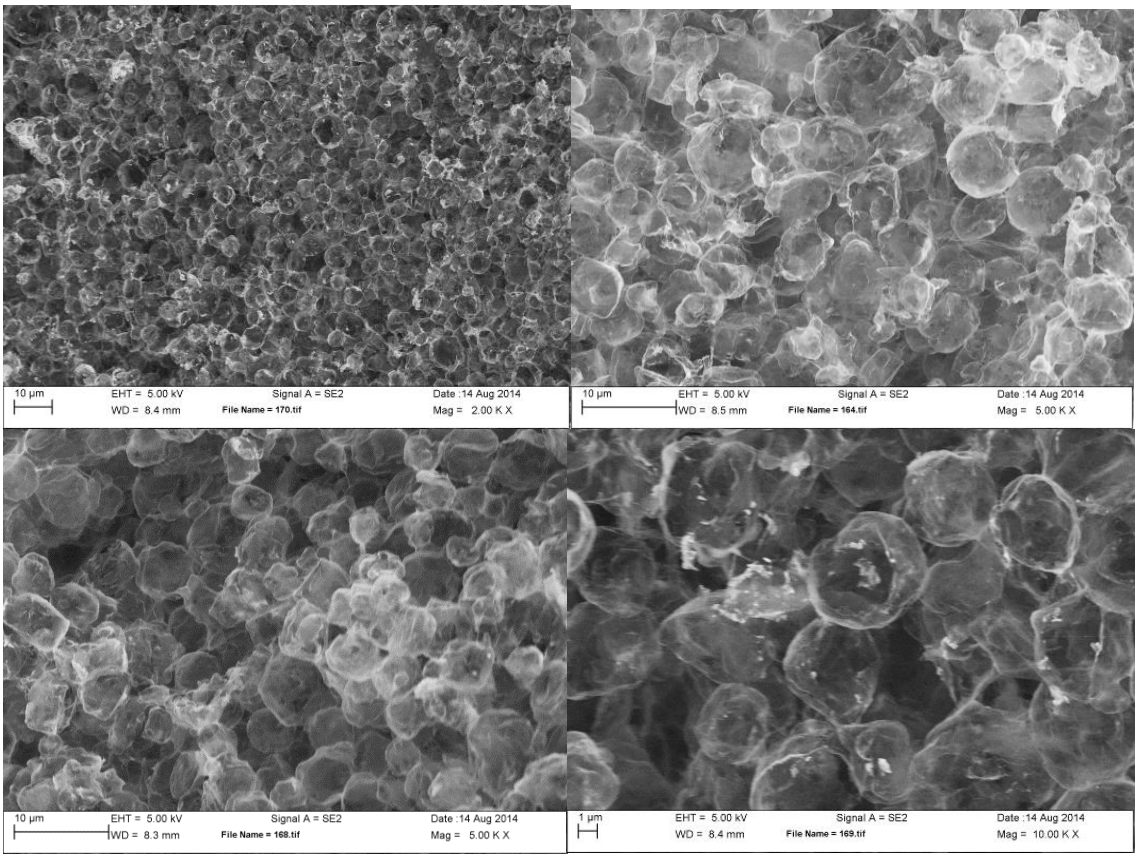

Figure 34: SEM image of HGOM/RF foam sample; 10 mg/mL: 80% GO, 20% resorcinol-formaldehyde.

As mentioned the samples in all these figures are foams made with the *same amount of GO (i.e. 8 mg/ml) but changing the amount of Resorcinol Formaldehyde.* Notice that we indicate the concentrations in mg of solid per ml. **Figure 32** has a concentration of 40 mg/mL of solids: 20% GO, 80% resorcinol-formaldehyde respectively (ie. 8 mg of GO and 32mg of RF). **Figure 33** shows SEM images of HGOM/RF foam sample made with concentrations of graphene oxide of 20 mg/ml: with 40% concentration of graphene oxide and 60% concentration of resorcinol-formaldehyde (ie. 8 mg of GO

and 12 mg of RF) and **Figure 34** has concentrations of 10 mg/mL: 80% GO, 20% resorcinol-formaldehyde (i.e 8mg of GO and 2 mg of RF).

We observe that Figure 33 and Figure 34 which were made with the same amount of GO show samples that display very similar particle size and porosity indicating that the pore size is mainly dominated by the concentration of GO and not the RF. Samples with higher amount of RF (Figure 34) show less transparency and thus thinner membranes than the ones obtained with less amount of RF. So the larger the amount of RF the thicker the membranes. We can observe when the ratio of GO/RF is higher the samples are thicker and more robust (less transparent). This is consistent with our conclusions for the synthesis of the HGOM particles. So for the same amount of GO the particle size does not change much, indicating that the RF does not alter the size of the HGOM particles but just glues them together. The densities of the foam HGOM samples were measured by weighing each sample and dividing by the volume of that sample, as described in the Methods section of this Chapter.

Figure 35 contains the a listing of the density of the HGOM-RF samples in this series of SEM images. Also the density of other samples of HGOM-RF were measured. It is apparent that the density is slightly higher for every sample compared with the original starting 'solids' material density. This is likely because some shrinkage of the foam samples occurs during the curing process. Also, shrinkage might occur as the sample is dried and the cores are sublimed. The standard error of the density measurements is reported in the table.

mg/mL solids	GO wt%	RF wt %	Final mg/mL
2.5	80	20	4.78 ± 0.05
5	80	20	8.2 ± 0.1
10	80	20	11.4 ± 0.2
20	40	60	33.4 ± 0.4
20	20	80	22.5 ± 0.7
35	56	44	52.3 ± 0.2
42	7	93	69.0 ± 0.3
42	41	59	55.8 ± 0.2
52	38	62	77.1 ± 0.2
56	29	71	81.3 ± 0.3

Figure 35: The density of HGOM-RF foams was measured. The "mg/mL solids" column is the theoretical amount of RF which could have formed from the resorcinol and formaldehyde plus the amount of GO in the HGOMs. The "Final mg/ml") column is the dry weight of the sample after sublimation of the Naphthalene core and drying.

Finally SEM images of even lighter weight samples with concentrations of 5 mg/mL solids and 1 mg/mL are depicted in **Figure 36** and Figure 37.

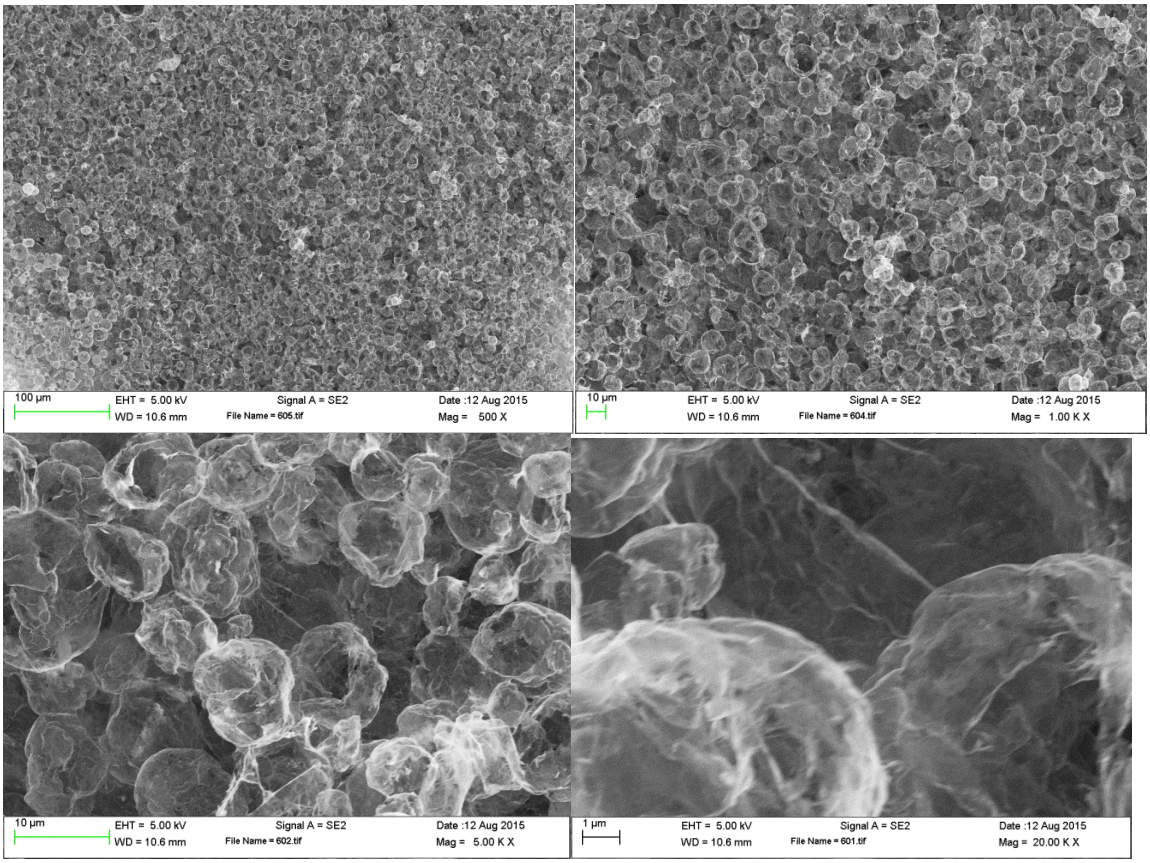

Figure 36: SEM image of HGOM/RF foam sample 5 mg/mL solids.

In Figure 37 a very low density sample was produced. At high magnification, the sample appears to be somewhat transparent. The sample was not sputter coated prior to imaging.

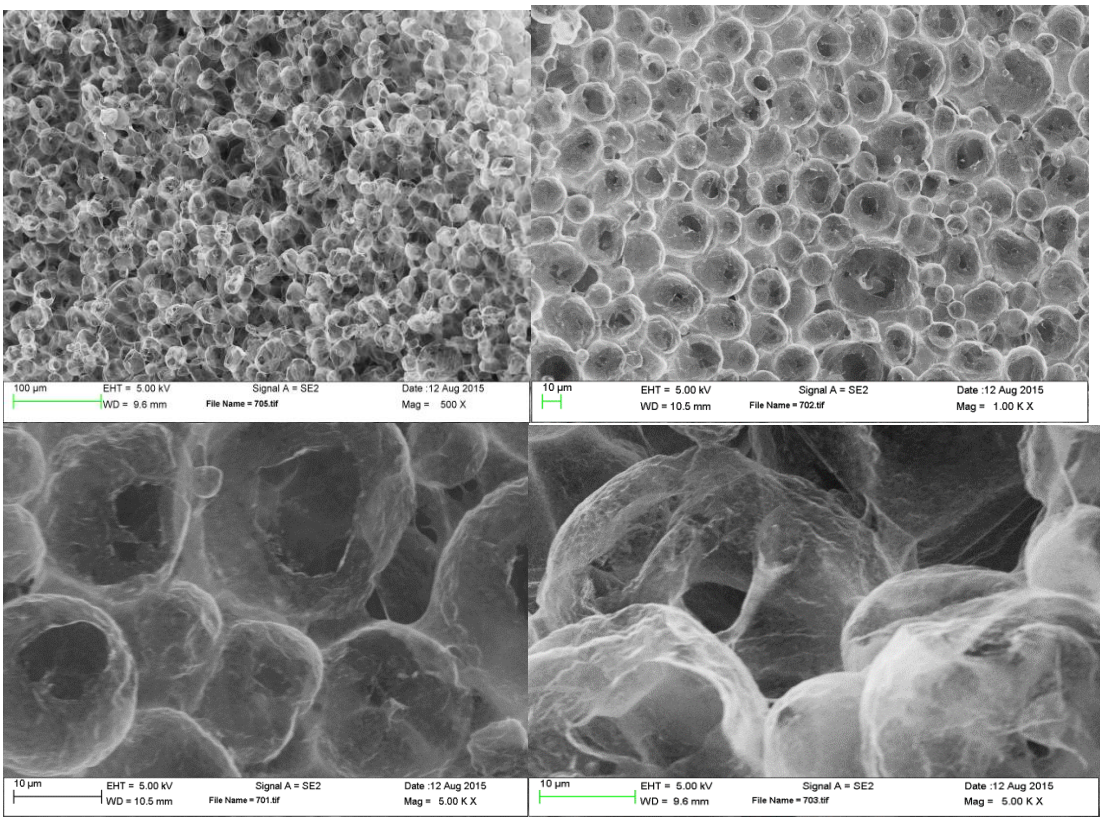

Figure 37: SEM image of a very light weight sample, 1 mg/mL solids.

Figure 38 shows a sample in which two different sizes of HGOMs were added to the foam, potentially adding different properties to the final product.

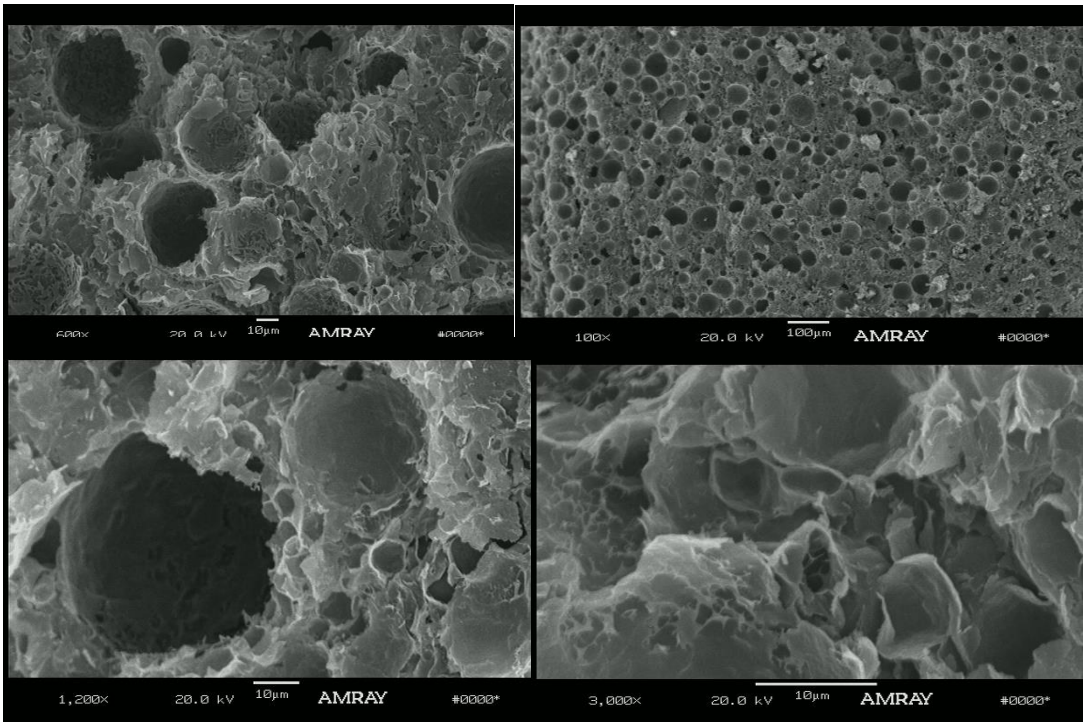

Figure 38: HGOM-RF foams made with a 'solids content' of 42 mg/mL (17mg/mL GO and 25 mg/mL RF) made by incorporating different sizes of HGOM particles into the mixtures.

We also made samples using an acetic acid catalyst instead of the basic sodium carbonate catalyst. The foam samples produced were very brittle, but did not retain the spherical HGOM particles of the sodium carbonate catalyzed foam samples. Clearly, washing any acetic acid from the HGOM before producing the foam samples is necessary to retain the HGOM structures. One of the acid catalyzed samples is seen in the SEM image in **Figure 39**.

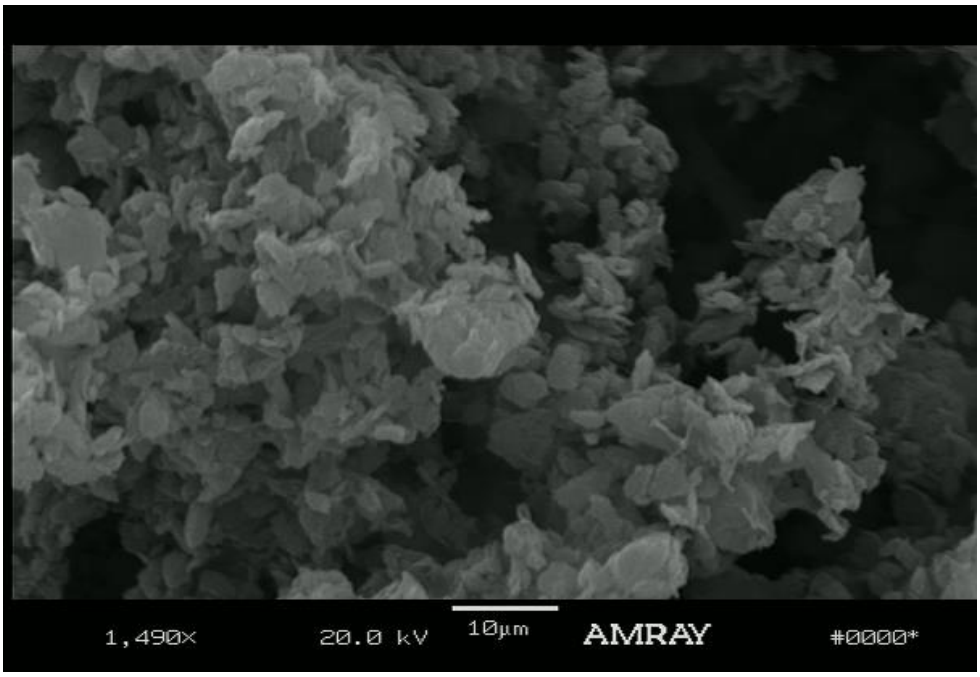

Figure 39: SEM image of acid catalyzed HGOM-RF foam sample.

Adding to the utility of the process, the foam may be cast into nearly any shape, or cut to exact specifications after casting. Figure 40 is of a GO-RF foam sample, initially cast as a cylinder, which was then cut in the dry state after casting. (This is the sample as shown in the SEM image of **Figure 30**. Machining and/or grinding before water/naphthalene removal is also a possibility.

Figure 40: *Photo of sample of a foam cut with a razor blade. Using a casting process can simplify fabrication for specific applications. However, the nanofoams produced by this method can also be cut or milled in the dry state.*

The x-ray diffraction pattern (XRD) in Figure 41 is of a GO-RF foam sample made as a composite from hollow graphene oxide spheres and resorcinol-formaldehyde resin.

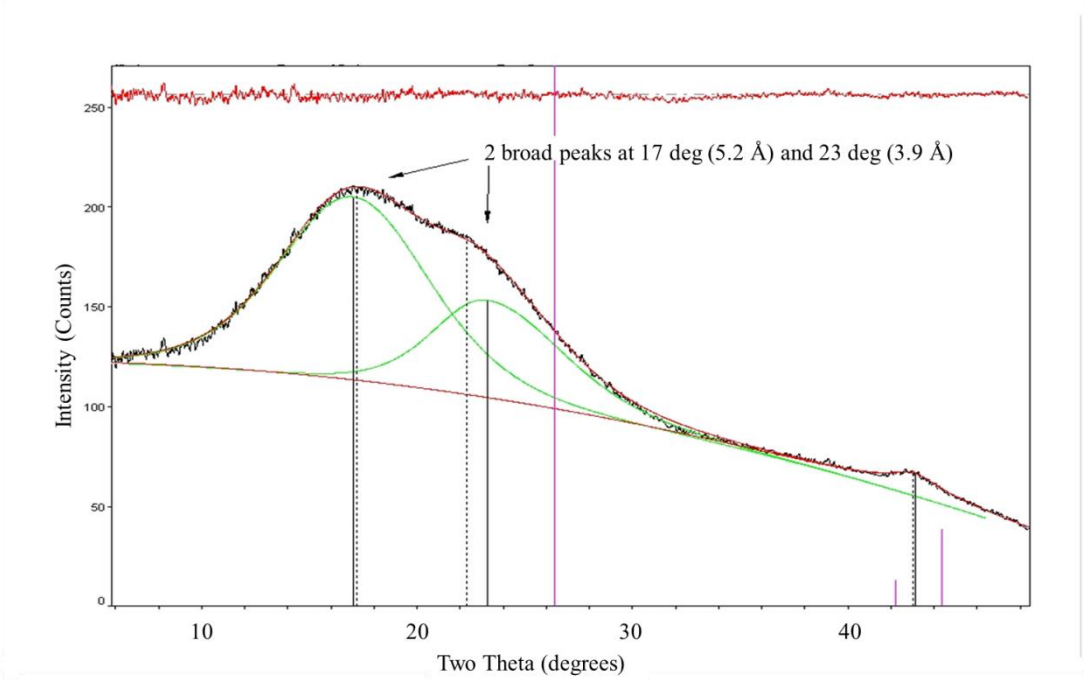

Figure 41: X-ray diffraction pattern of an unpyrolyzed RF-HGOM foam sample.

The two peaks (deconvoluted) of the unpyrolyzed sample at 17 and 23 degrees correspond to the stacking distance of the GO sheets. The interlayer spacing or distance is denoted as d_{002} and can be calculated from the 002 XRD peak position using Bragg's Law. This distance is depends on the number of intercalated water molecules. Typically, this peak position is in the range between 8 to 12 degrees (2Θ). Extensive heating of the sample at 65°C for two weeks and then drying of the sample appears to have eliminated much of the intercalated water. And may have also altered oxides (such as carboxyl and hydroxyl groups) to allow close spaced stacking of at least a portion of the GO/Graphene foam sample. It would appear that the typical graphene oxide peak at 8 to 12 degree has been eliminated due to the extended processing conditions through reduction or dehydration of the water trapped between the graphene oxide sheets. It might be possible that RF has impregnated between the sheets and has changed the long range order of the stacking for the peak that would be expected. The peak in **Figure 41** at 43 degrees is the GO/Graphene 110 peak. The designations of the diffraction pattern peak for graphene and graphene oxide follows the assignments from Physics and Applications of Graphene – Experiments.

Figure 42 show the XRD patterns from for samples of graphene oxide which were obtained by heated under an inert atmosphere for an hour at temperatures between 50°C and 1000°C[66]. The 002 peak gradually migrates to higher 2Θ values (indicating smaller interlayer spacing) as the processing temperature is increased. Two peaks appear in the 170°C to 200°C range These peaks are superimposed the XRD pattern

for our sample in Figure 43. It should be noted that the peak positions are nearly identical from our sample which was processed under wet condtions at 65°C for two weeks, as those heated under an inert atmosphere for one hour at approximately 180°C. Our sample has broader XRD peaks in this region, which could be because of the thin membrans lead to a reduction in the long-range order of the structure.

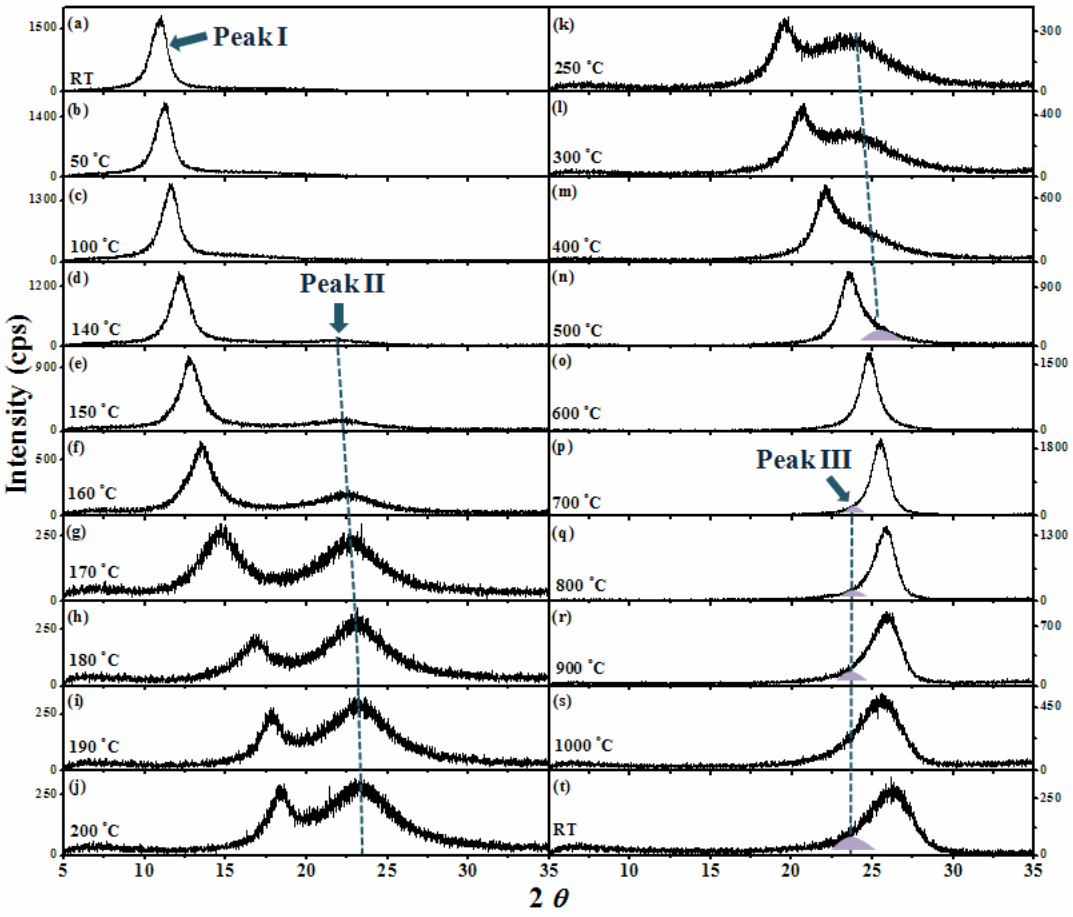

Figure 42: This figure, adapted with permission from Ref.[66], shows the XRD pattern of graphene oxide obtained by heated under an inert atmosphere for an hour at various temperatures.

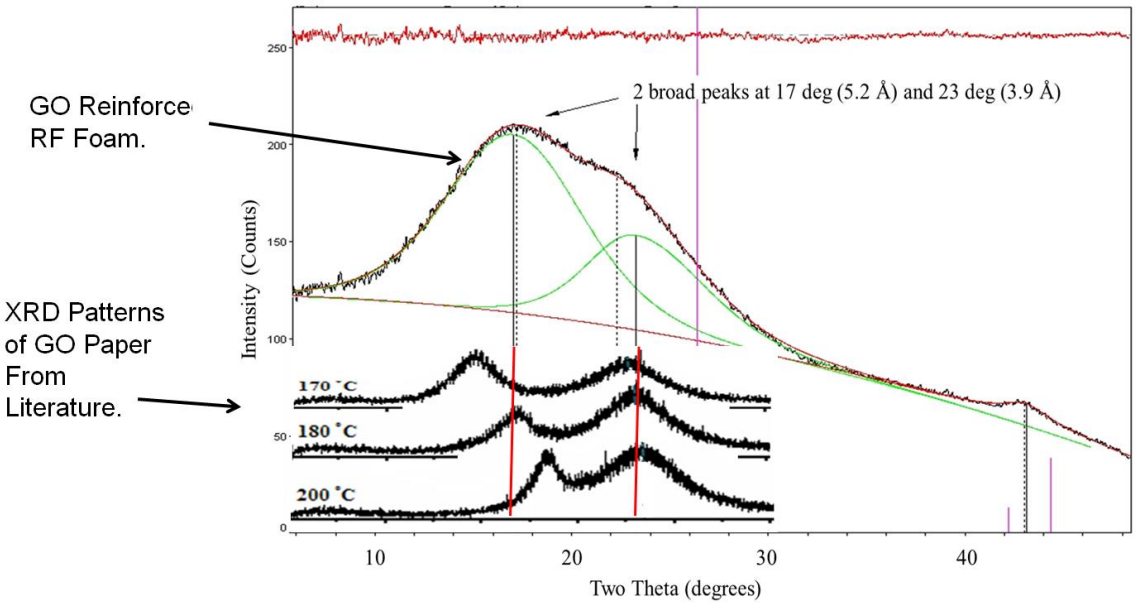

Figure 43: *In the Figure, the XRD pattern of our HGOM-RF foam can be compared with the positions of published data adapted with permission from Ref.[66] These lower left XRD patterns were obtained from samples of graphene oxide which were heated under an inert atmosphere for an hour at the specified temperatures: from the bottom XRD pattern upwards: 200°C, 180°C, and 170°C.[66] Note that the three XRD patterns in the lower left of the image, from Physics and Applications of Graphene – Experiments,[66] are offset along the intensity axis (y-axis) for clarity.*

3.2 Activated HGOM-RF Foams.

The RF-HGOM foam sample was soaked with a 5 M KOH solution and heated to 550 C under flowing nitrogen for one hour. After which the sample was washed with DDI for two days. The X-ray diffraction pattern of the dried activated sample is shown in Figure 44.

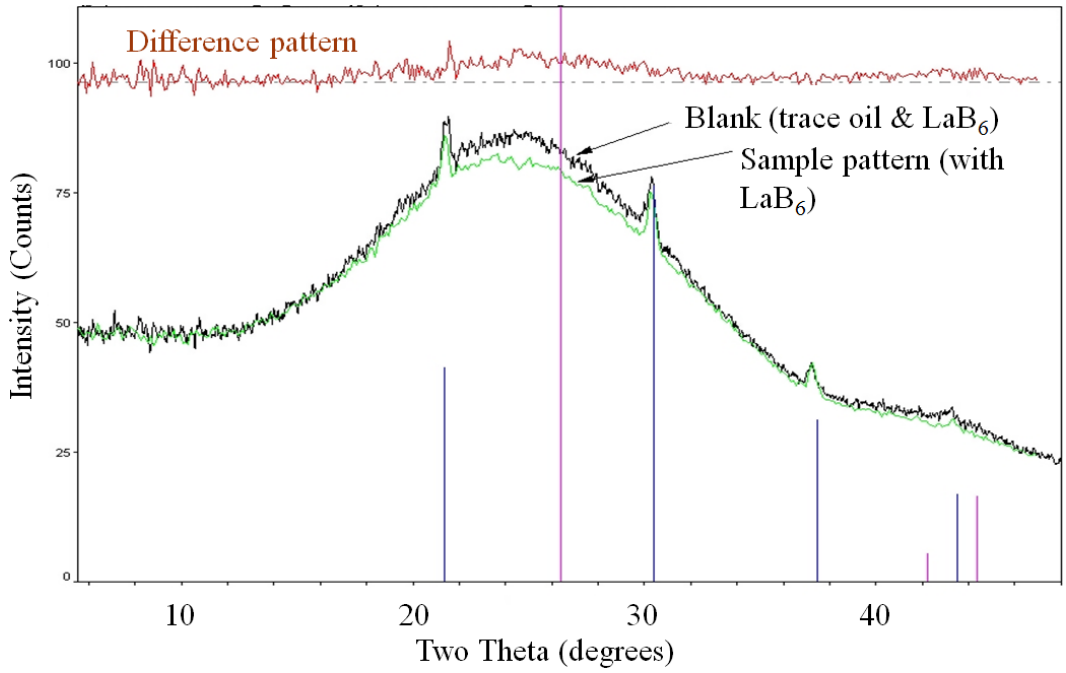

Figure 44: *The XRD difference pattern of the activated sample (with background scattering removed) consists of mostly scattered x-rays. The graphene stacking order of the sample has been greatly disrupted by the activation process and little long range order remains. It appears that there is only a hint of the 002 stacking near 25 degrees and the 110 peak at 43 degrees.*

GO-RF foam samples (approximately 100 mg) were put into 16 mL of aqueous KOH solutions of various concentrations in a capped polyethylene bottle. The samples were allowed to become completely saturated with the aqueous KOH solution. The samples were dried at 120C, transferred to a horizontal tube furnace, heated to 180 °C for 1 hour, and then heated to 700 °C for 1 hour under flowing nitrogen at 100 mL/minute with a heating rate of 5C/minute. The KOH to sample ratios were 2.6, 5.3, 6.9, and 9.6 for KOH solutions of 15, 27, 37, and 45 wt% KOH respectively. The pyrolyzed activated samples were soaked in 100 mL of DDI water for two days to allow potassium compounds to diffuse from the activated carbonized foam. The DDI water was replenished twice daily, after which the sample was air dried at

65 °C. Yield (by mass) upon pyrolysis was 33.2, 23.5, 12.0, and 3.4 percent, for the samples with KOH activation concentrations of 15, 27, 37, and 45 wt % KOH, respectively. The pyrolyzed, but unactivated, sample had a yield of 55.3 percent.

In what follows we show how we calculated the resulting surface area and pore space of these samples using Non-local Density Functional Theory.

3.2.1 Isotherms for the Calculation of Pore Size and Surface Area using Non-Local Density Functional Theory (NLDFT)

In the NLDFT method, theoretical adsorption isotherms calculated using the NLDFT model are validated against the experimental adsorption and desorption isotherms on mesoporous crystals of MCM 41 and SBA-15 types with well characterized cylindrical pores.[140] Within the NLDFT models, the position of capillary condensation in cylindrical pores is associated with so-called mechanism of delayed, or spinodal condensation occurring at the limit of stability of adsorption films, or at the vapor–liquid spinodal. The NLDFT model can precisely predict the capillary condensation and desorption pressures in cylindrical pores wider than ~5 nm. [140] In pores smaller than 5 nm, the NLDFT adsorption isotherms progressively deviate from the experimental isotherm since the NLDFT model does not account for the nucleation phenomenon, therefore for pores smaller than 5 nm NLDFT does not make good predictions. ***Figure 45*** shows the adsorption isotherms of samples that were not treated with KOH. This includes a sample which was not pyrolyzed (no high temperature treatment) and another one which was pyrolyzed. All the pyrolyzed samples (ie. Those in **Figure 45** and all of those in **Figure 47**) were

pyrolyzed at 700 °C for 1 hour under flowing nitrogen at 100 mL/minute in a horizontal tube furnace. The ramp rate to 700 °C was 5 °C per minute.

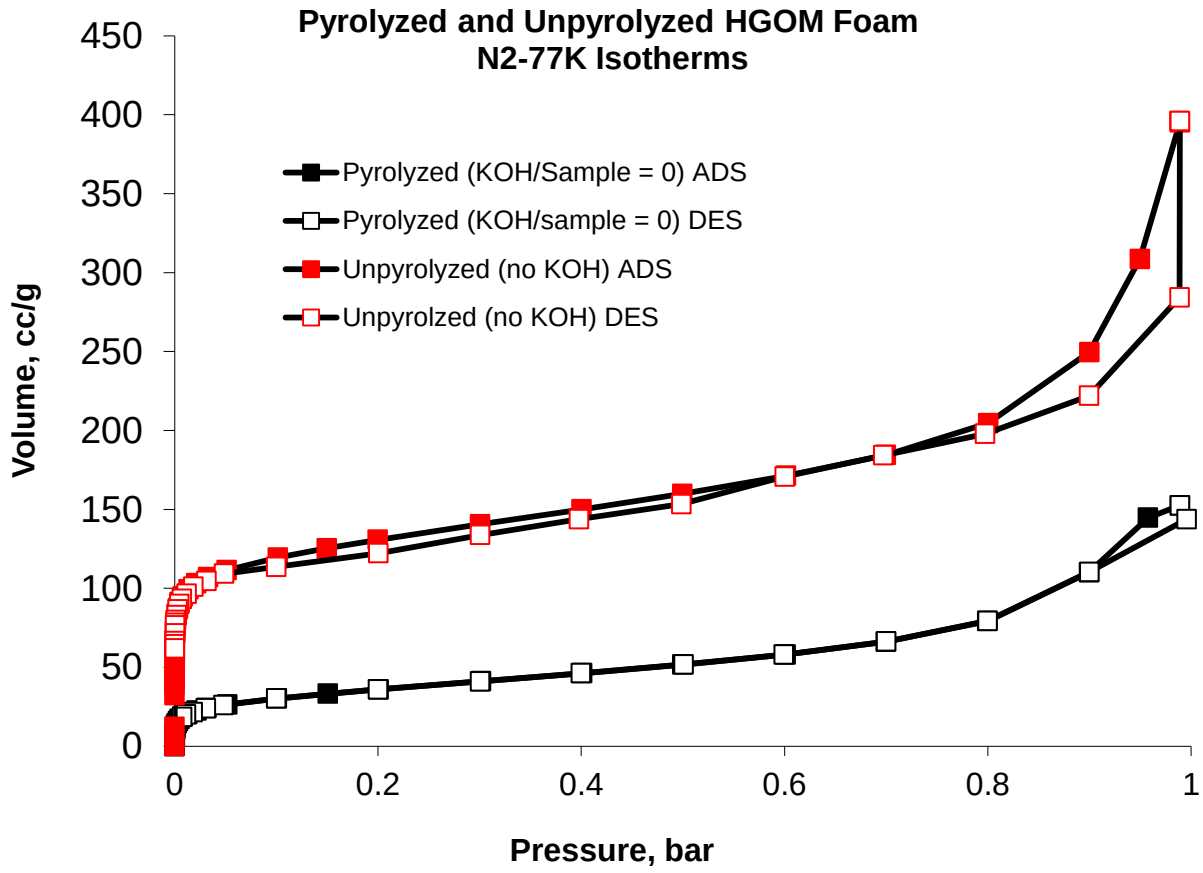

Figure 45: *Adsorption isotherm of pryolyzed and unpyrolyzed HGOM-RF foam samples. These samples were not treated with KOH.*

Figure 47 shows the adsorption isotherms of samples that were treated with KOH. By comparison of our isotherm in ***Figure 45*** with the experimental figure of N2 77K (*Figure 46*) we can say there is no pore blocking. Notice that the y axis is N(nnmol/g) is proportional to the volume in cc/g).

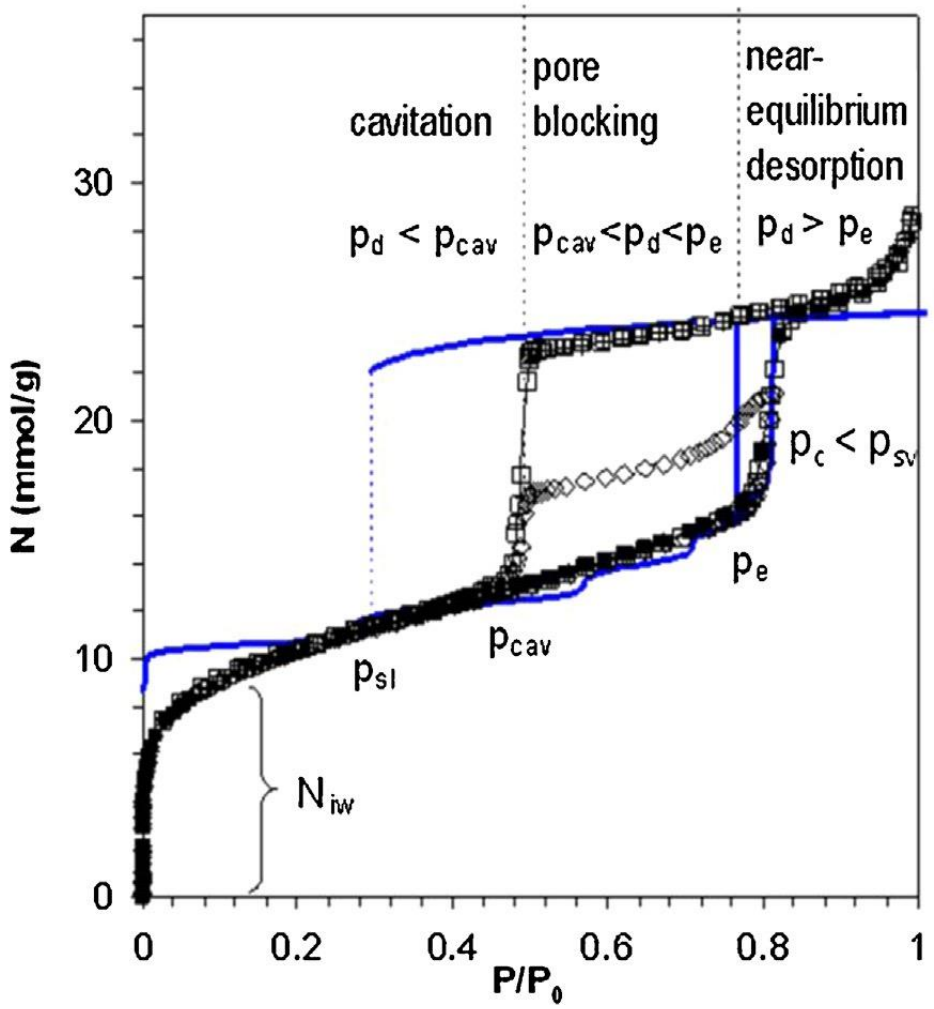

Figure 46 *NLDFT N_2 adsorption–desorption isotherm (at 77 K) in 15.5 nm spherical cavity (thick solid line) and experimental data on a FDU-1 silica sample (points). The theoretical pressures of liquid like spinodal, equilibrium, and vapor like spin- odal are denoted, respectively, as p_{sl} , p_e , and p_{sv} . Experimentally observed pressures of spontaneous capillary condensation and cavitation are denoted as p_c and p_{cav}, respectively ($p_c \approx p_{sv}$ and $p_{sl} < p_{cav} < p_e$). Three possible regimes of evaporation from the cavity are classified with respect to the pressure p_d of desorption from the neighboring pores or from the pore neck. (Adapted with permission from Ref. [140].* *Copyright (2002) American Chemical Society)*

Figure 46 shows the experimental curve of N2 adsorption-desorption at 77K on a FDU -1 silica sample. By comparing the desorption branch of **Figure 47** with *Figure 46* we could infer conclusions on the existence of pore blocking. In this particular figure it is difficult to say because more points would need to be taken on the

desorption branch for an accurate assessment. A sharp drop in the desorption branch would be indicative of pore blocking according.[143] Even though is not very sharp, this drop is indicative of pore blocking. It is known that interconnected porous systems (like silica KIT-6) can give rise to pore blocking effects, then it makes sense that we see this phenomenonm; and most aerogels also possess this type of geometry.

The criterion to determine whether a material is mesoporous is the existence of an hysteresis, although this tends not to be true with metal organic frameworks that do have mesoporosity but do not display an hysteresis.[143] The lack of an hysteresis indicates that the material is microporous. In our case the lack of hysteresis would also suggest that the graphene sheets are collapsed onto its self like activated carbon. The numerical results of the NLDFT model are shown in Table 1 where we see the different surface areas and pore size distributions, Micro (<2nm) and meso (>2nm). [139-141] **Table 1** shows the results of the calculated surfaces areas and pore size distributions derived from the data graphically represented in **Figure 45** and **Figure 47** using various different theoretical methods as described above and also includes Langmuir surface area, Brunauer–Emmett–Teller (BET) surface area which is an extension of the Langmuir theory. This table also includes the calculations for both meso-pores (pores with diameters between 2 and 50 nm) and micro-pores (pores less than 2 nm) surface areas using non-local density functional theory (DFT).

Next in the table is the volume calculated for meso and micro pores using non-local density functional theory (DFT). Finally the Barrett-Joyner-Halenda (BJH) pore volume calculation is included. Traditional Langmuir and BET theories were used to calculate surface areas to allow for direct comparison with other results in the literature.

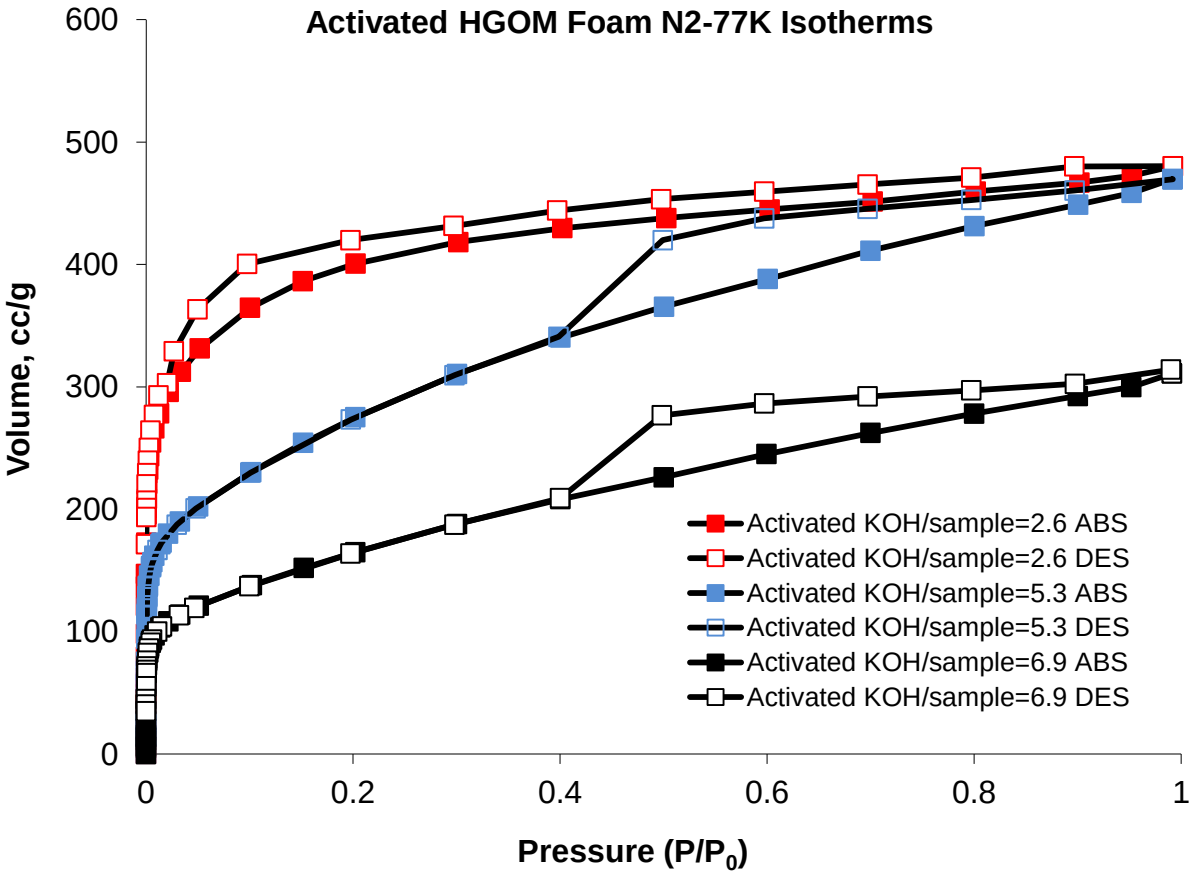

Figure 47: *Adsorption isotherms of activated HGOM-RF foam samples. These samples were treated with KOH and pryolyzed.*

Notice that the table does not explicitly tells the exact profile of the pore sizes, but provides useful information for direct comparison of the samples. The Table shows

results for Meso- and Micro- pores and it should be understood that these are pores in the aforementioned nanometer ranges.

The more recently developed, Non-local Density Functional Theory (DFT) was used for analysis of the pore size and pore space with in the samples, because Non-local Density Functional Theory may provide a more complete analysis for these types of structures. [139-141]

Characteristics of the Activated, Pyrolyzed, and Untreated RF-GO Foams							
Treatment (wt % KOH)	**S_{BET} (m^2/g)**	**S_{Lang} (m^2/g)**	**$S_{meso(DFT)}$ (m^2/g)**	**$S_{micro(DFT)}$ (m^2/g)**	**$V_{meso(DFT)}$ (cm^3/g)**	**$V_{micro(DFT)}$ (cm^3/g)**	**V_{BJH} (cm^3/g)**
0% (unpyrolyzed)	**128**	**204**	**49**	**39**	**0.174**	**0.023**	**0.235**
0% (pyrolyzed)	**425**	**649**	**98**	**436**	**0.398**	**0.142**	**0.607**
14.6	**1268**	**1933**	**559**	**645**	**0.179**	**0.492**	**0.738**
26.6	**968**	**1532**	**247**	**487**	**0.425**	**0.24**	**0.722**
36.6	**587**	**933**	**174**	**273**	**0.313**	**0.133**	**0.478**

Table 1: *The surface area using BET theory and Langmuir adsorption isotherms for samples with different activation treatments are shown in the table. Micro (<2nm) and meso (>2nm) pore size distributions (surface area and volume) are calculated using non-local density functional theory (DFT). Additionally, the total pore volume calculated by BJH is also included. This table characterizes these samples using the Langmuir and BET theories for direct comparison with other results in the literature. Many such studies predate the silt NLDFT method.*

The microporosity and mesoporosity of HGOM-RF samples analyzed with Non-local Density functional theory is depicted in Figure 48. The data in this figure is the same as

can be seen in Table 1 for the different levels of KOH activation. This also produced the highest ratio of mesopores to micropores for the activated samples. Different levels of KOH activation resulted in different levels of surface area. The highest surface area was produced with an activation ratio of 2.6 KOH to the RF-HGOM sample. The high ratio of mesopores to micropores would be expected to provide higher transport rates for many applications, as is described and detailed in section 4.1 of this chapter.

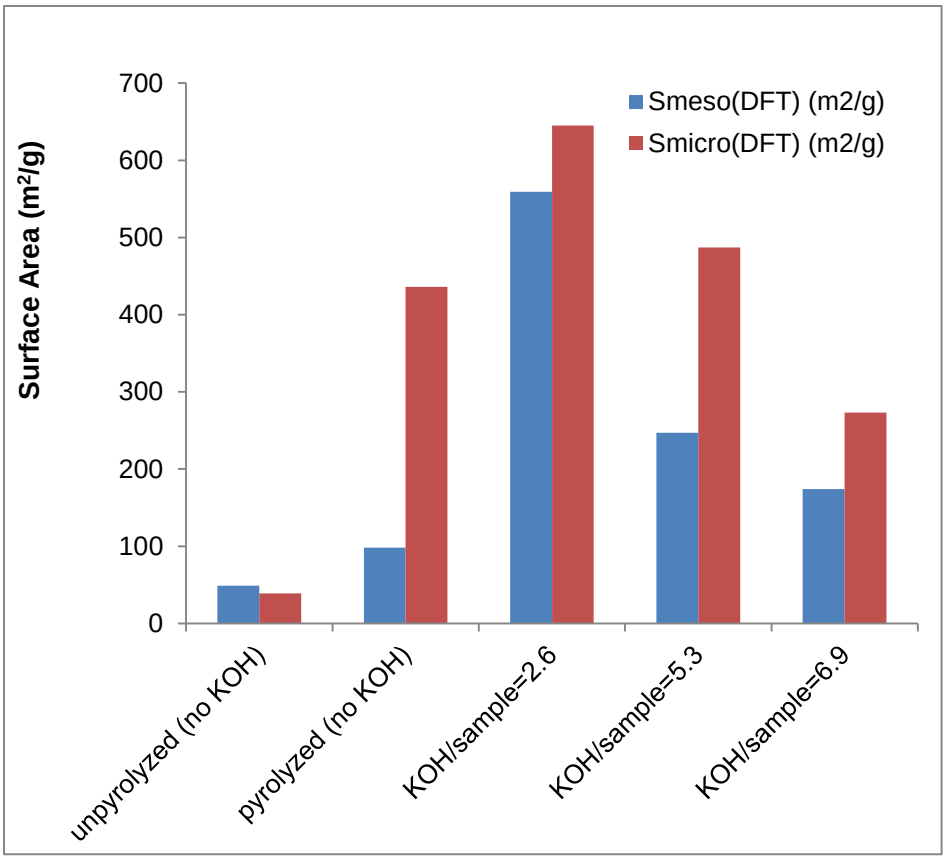

Figure 48: Chart of the microporosity and mesoporosity of HGOM-RF samples with different levels of KOH activation. Note that by comparison, low levels of surface area were obtained in the unpyrolyzed sample.

The Langmuir surface area was increased to a maximum of 1933 m^2/g with the lowest level of activation treatment, and further increases resulted in decreased surface area as can be seen in **Figure 49**. Non-local Density functional theory was

used for analysis of the pore size and pore space within the samples. Although there are reasons to believe the NLDFT is an appropriate method to characterize these porous materials, we have included the Langmuir surface area and BET surface area for comparison with other results previously described in the literature.

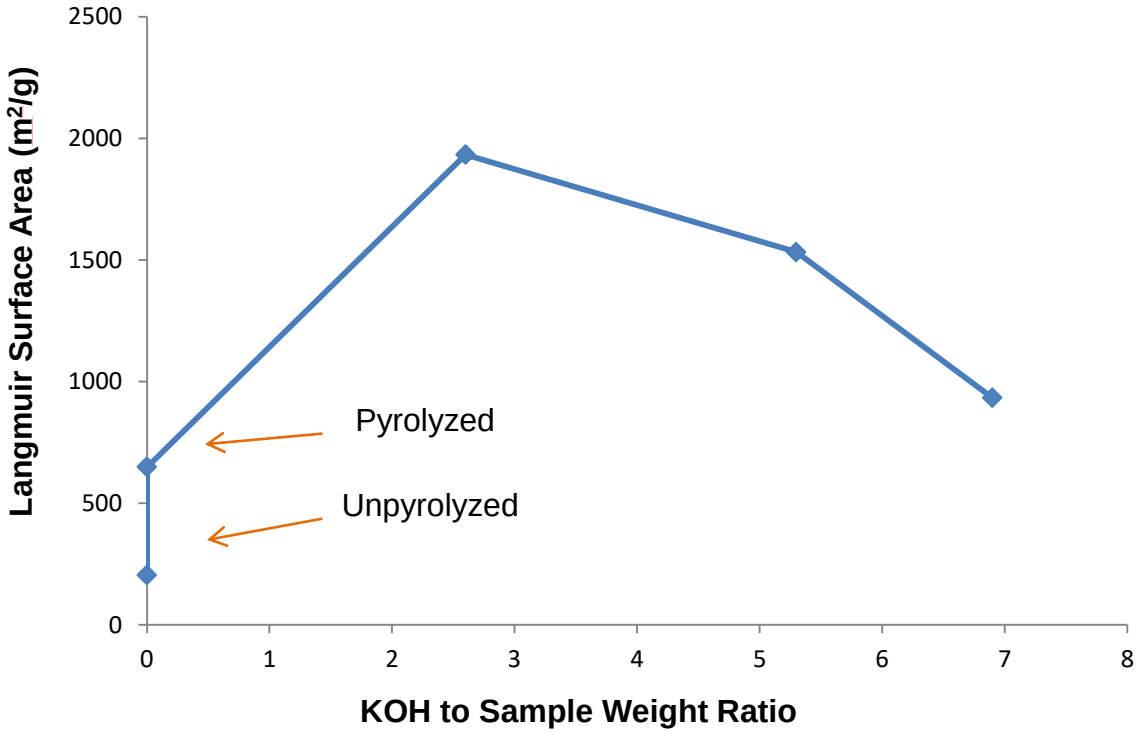

***Figure 49**: Surface area as a function of the amount of KOH taken up by the sample during activation.*

3.3 HGOM-Foams with amine based binding agents (triethylenetetramine hydrate): Treating a suspension of HGOM near its maximum packing density with amine cross-linking agent yields a solid product after drying and sublimation of the naphthalene. The Raman spectrum (with excitation wavelength of 514 nm, smoothed ~4 cm^{-1}) of this reaction product is shown in ***Figure 50***.

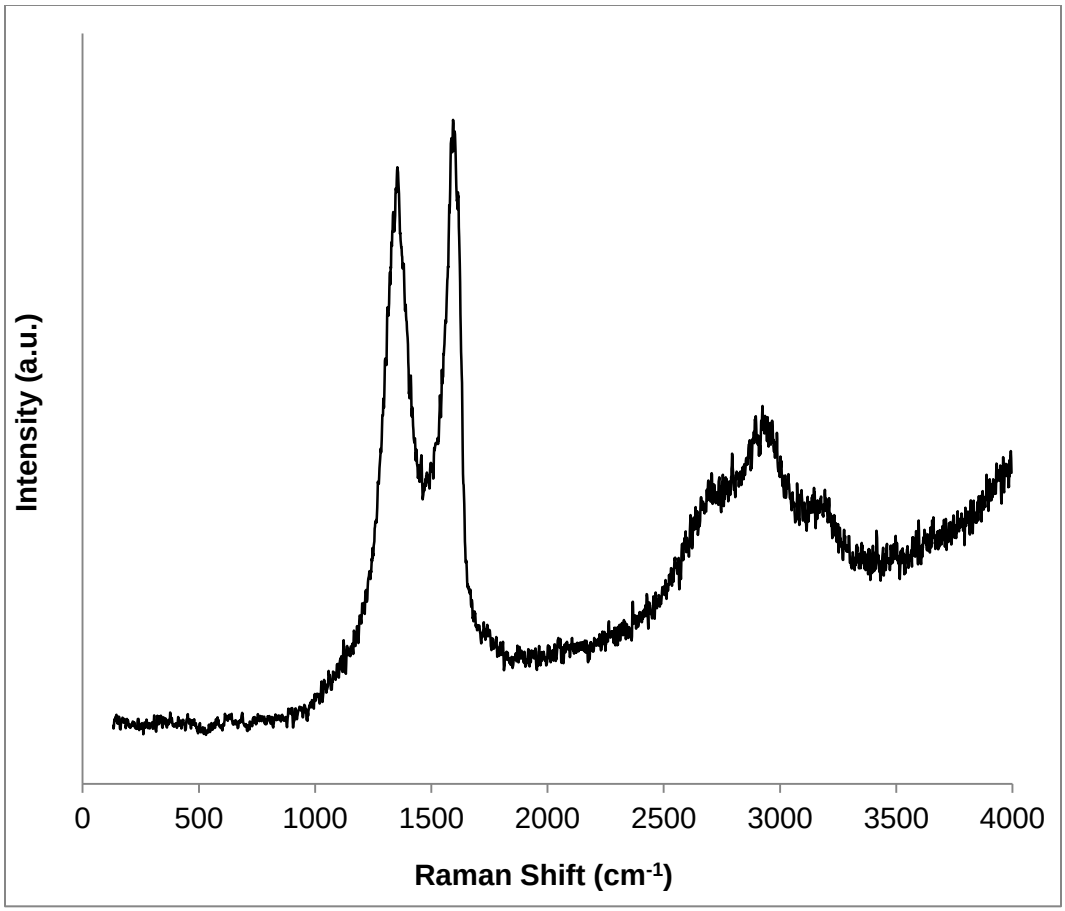

***Figure 50**: Raman spectrum of triethylenetetramine hydrate crosslinked carbon graphene oxide based foam sample. The D band for the triethylenetetramine cross linked sample is at 1355 (cm^{-1}), the G band is at 1595 (cm^{-1})*

The D band for the triethylenetetramine cross linked sample is at 1355 (cm^{-1}), the G band is at 1595 (cm^{-1}), and the D+G peaks at approximately 2943 (cm^{-1}). These values for the D and G bands correspond well to the literature for graphene oxide. Reports in the literature for the D and G bands for graphene oxide range from 1354 to 1362 (cm^{-1}), and 1594 to 1598 (cm^{-1}), respectively.[8,67]

3.4 Ice-segregation-induced self-assembly. (GO-RF). Foam samples were also constructed using an ice-segregation-induced self-assembly method. The details are

of the construction of these foams can be found in the Methods and Materials Section. Columnar structures (micro-channels) formed via ice-segregation-induced self-assembly are seen in the SEM images of a sample prepared with only resorcinol-formaldehyde resin (with no graphene oxide) in ***Figure 51***.

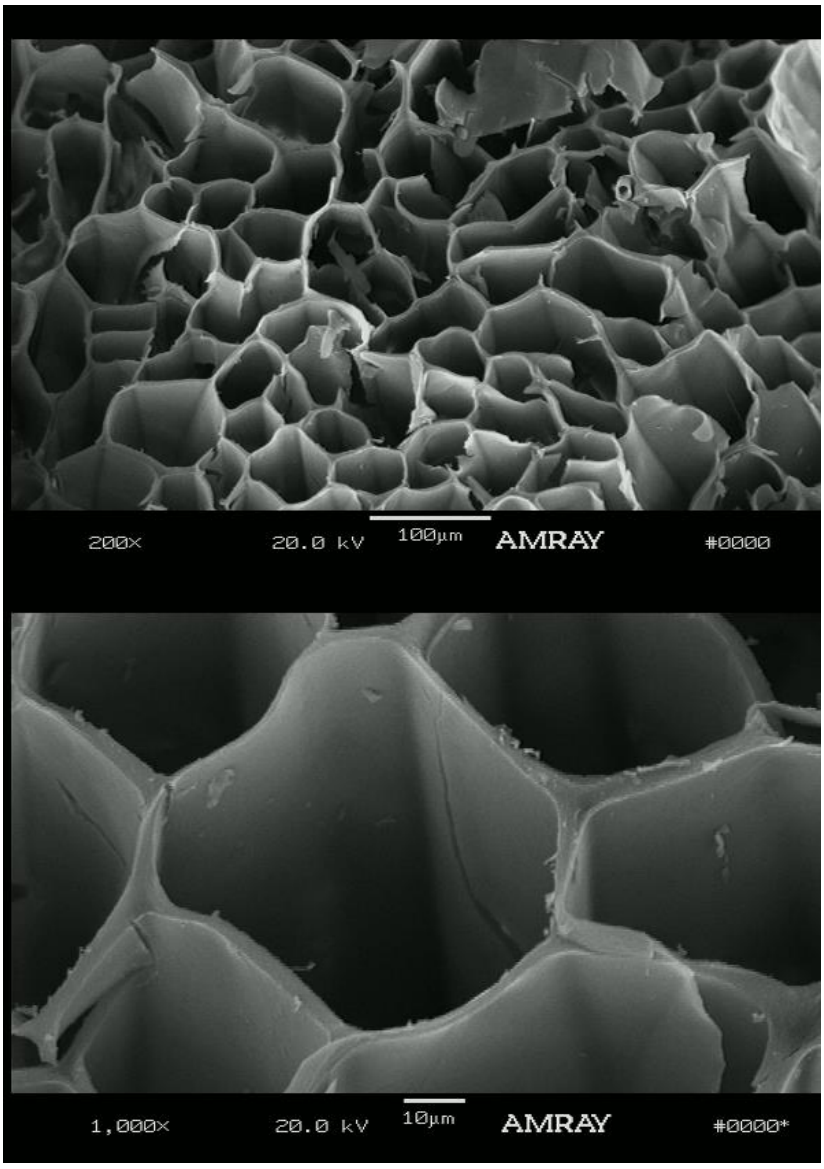

Figure 51: *Ice segregation induced self-assembly of resorcinol-formaldehyde resin. The aqueous resin was 100 mg/mL resorcinol-formaldehyde. Scale bars: (a) 100µm, (b) 10µm.*

This resorcinol-formaldehyde resin (100 mg/mL) sample was made for comparison to the graphene oxide / resorcinol-formaldehyde samples. Additionally, three different samples were made at various ratios of graphene oxide to resorcinol-formaldehyde resin. The overall concentration of the solids in the first GO/RF sample considered was only 12 mg/mL (10 mg/mL resorcinol-formaldehyde resin and 2 mg/mL graphene oxide). SEM images of the sample can be seen in **Figure 52**. Columnar structures somewhat similar to the sample with only resorcinol-formaldehyde are produced; however the column walls are exceptionally thin due to the very low concentration of solids within the sample.

.

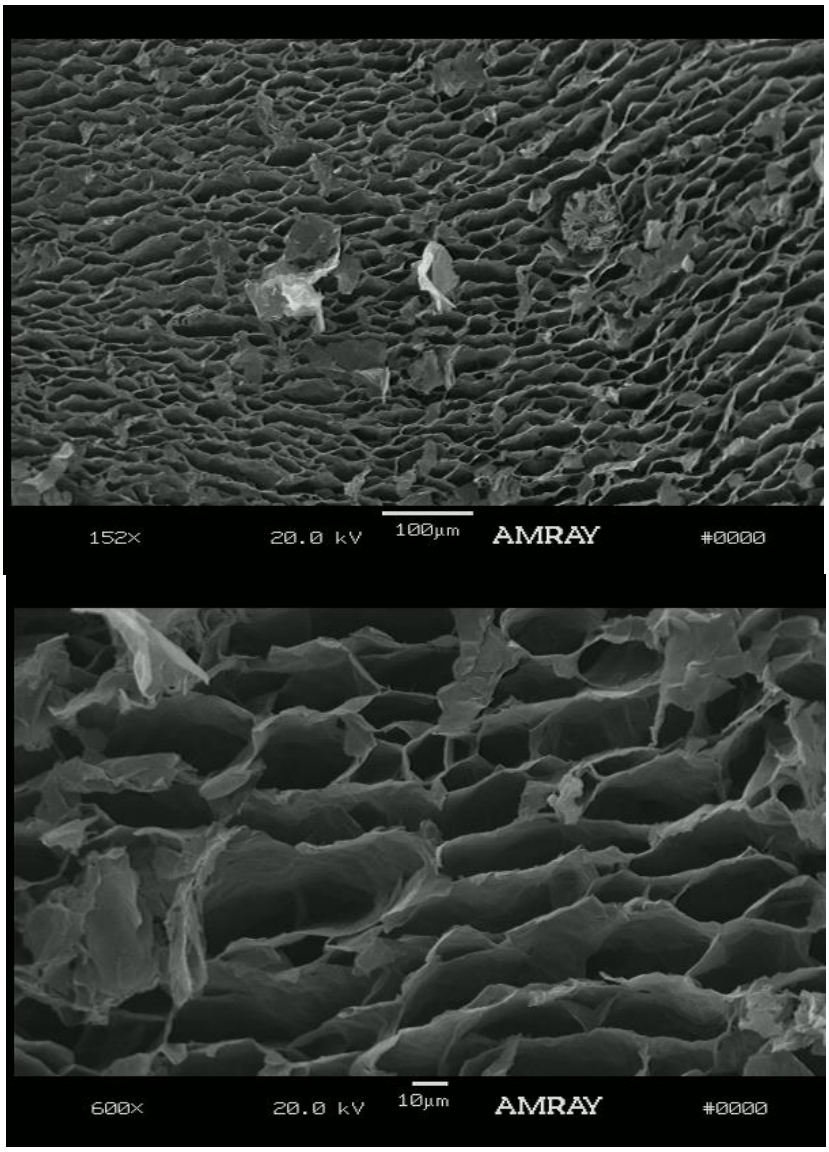
152×
20.0 kV
100µm
AMRAY
#0000
600×
20.0 kV
10µm
AMRAY
#0000

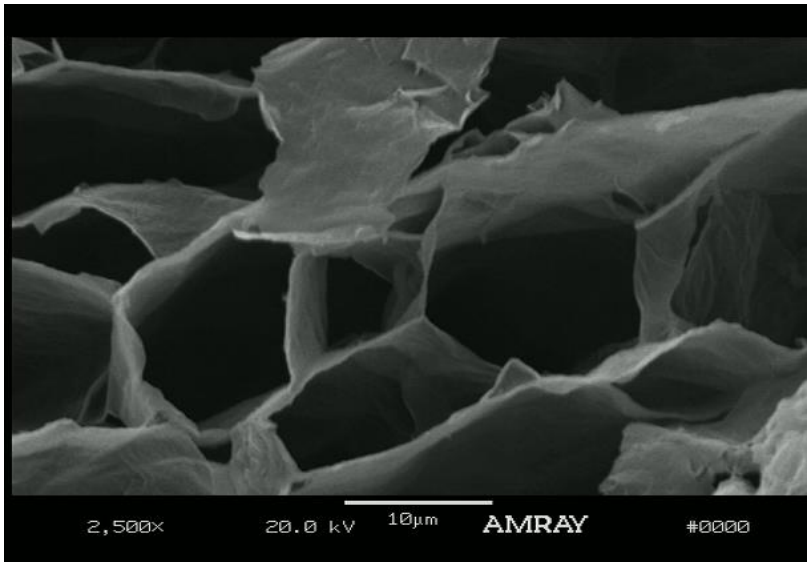

Figure 52: SEM images of light weight graphene oxide/resorcinol-formaldehyde foam with micro-channels formed through ice segregation induced self-assembly. The sample was frozen and then cut prior to subliming the aqueous phase from the frozen sample. The 'solids' in the liquid mixture, prior to setting was 12 mg/mL total: 10 mg/mL resorcinol-formaldehyde and 2 mg/mL graphene oxide. Scale bars are (a) 100 µm, (b) 10 µm, and (c) 10 µm.

This same ice segregation induced self-assembly sample could support 13,500 times its own weight. **Figure 53** is an image of the sample under load, supporting 56.7 grams, though the weight of the foam sample is only 4.2 mg.

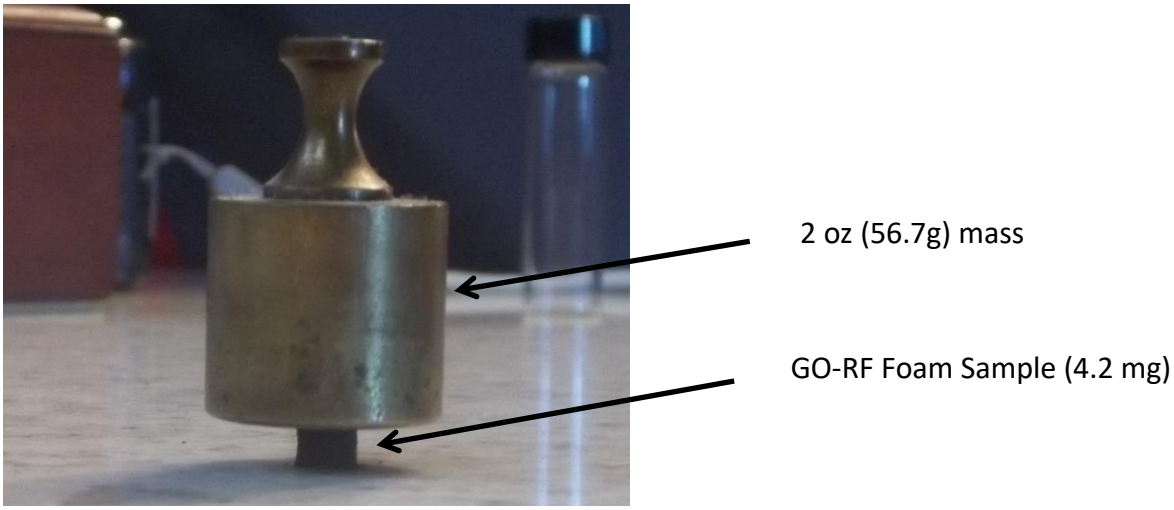

Figure 53: A RF-GO cryogel sample (4.2 mg) supporting a 2 oz (56.7g) counterpoise, or approximately 13,500 times its own weight.

A sample was prepared with a higher ratio of graphene oxide containing 30 mg/mL total solids (20 mg/mL resorcinol-formaldehyde and 10 mg/mL graphene oxide). The SEM images of the sample were obtained by processing the sample as previously described and cutting the sample in the frozen state prior to SEM imaging; the resulting images are found in **Figure 54**. The channels appear less organized and less uniform than the sample with lower ratios of graphene oxide to resorcinol-formaldehyde resin.

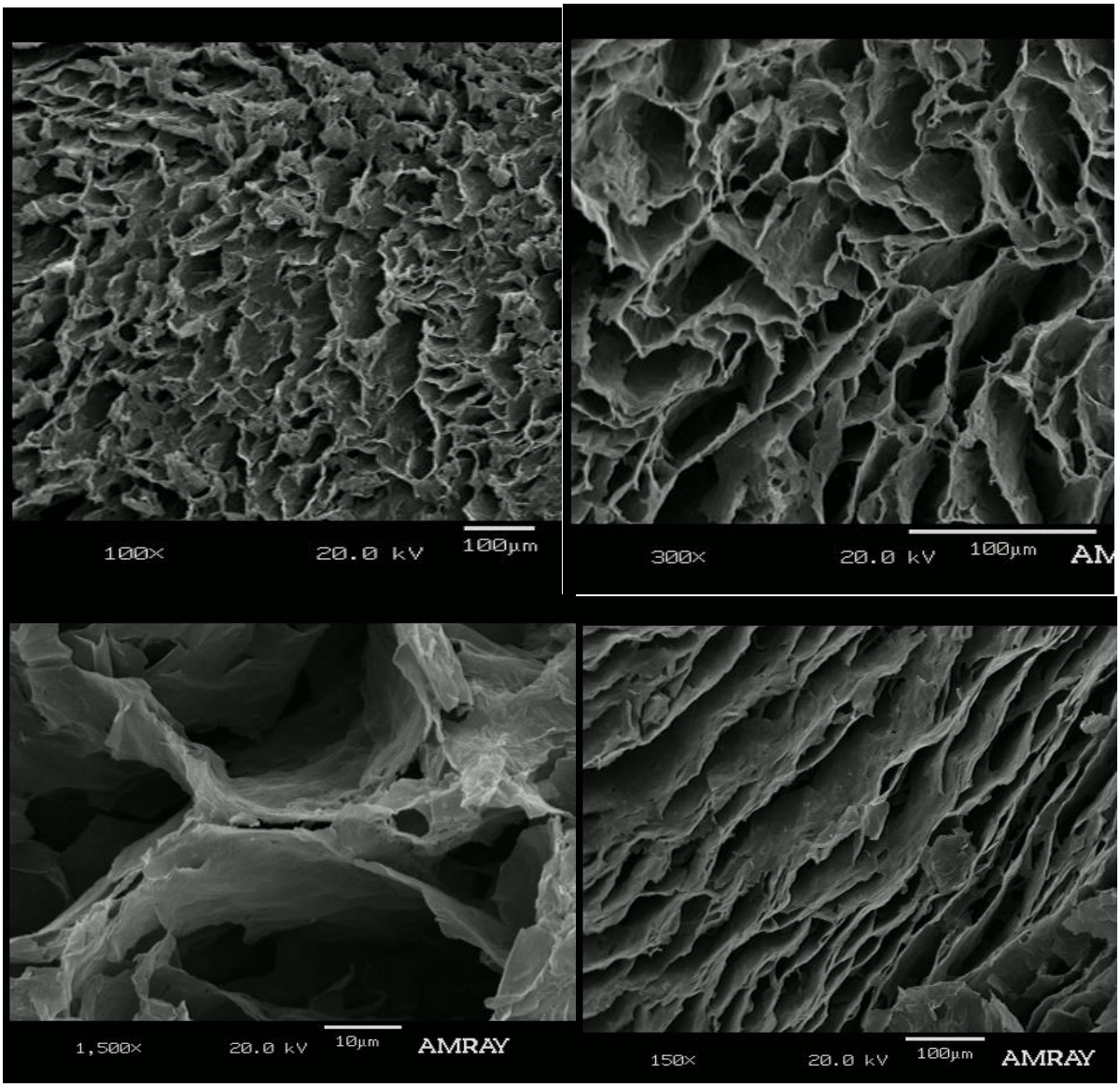

Figure 54: SEM images of sample with micro-channels formed through ice segregation induced self-assembly. The sample formulation was 20 mg/mL resorcinol-formaldehyde and 10mg/mL graphene oxide. SEM images in (a), (b) and (c) were cut perpendicular to the channels formed by the ice growth. The sample in (d) imaged cut parallel to the ice growth prior to SEM imaging, revealing the long channel in which ice growth occurred. (12-5-3)

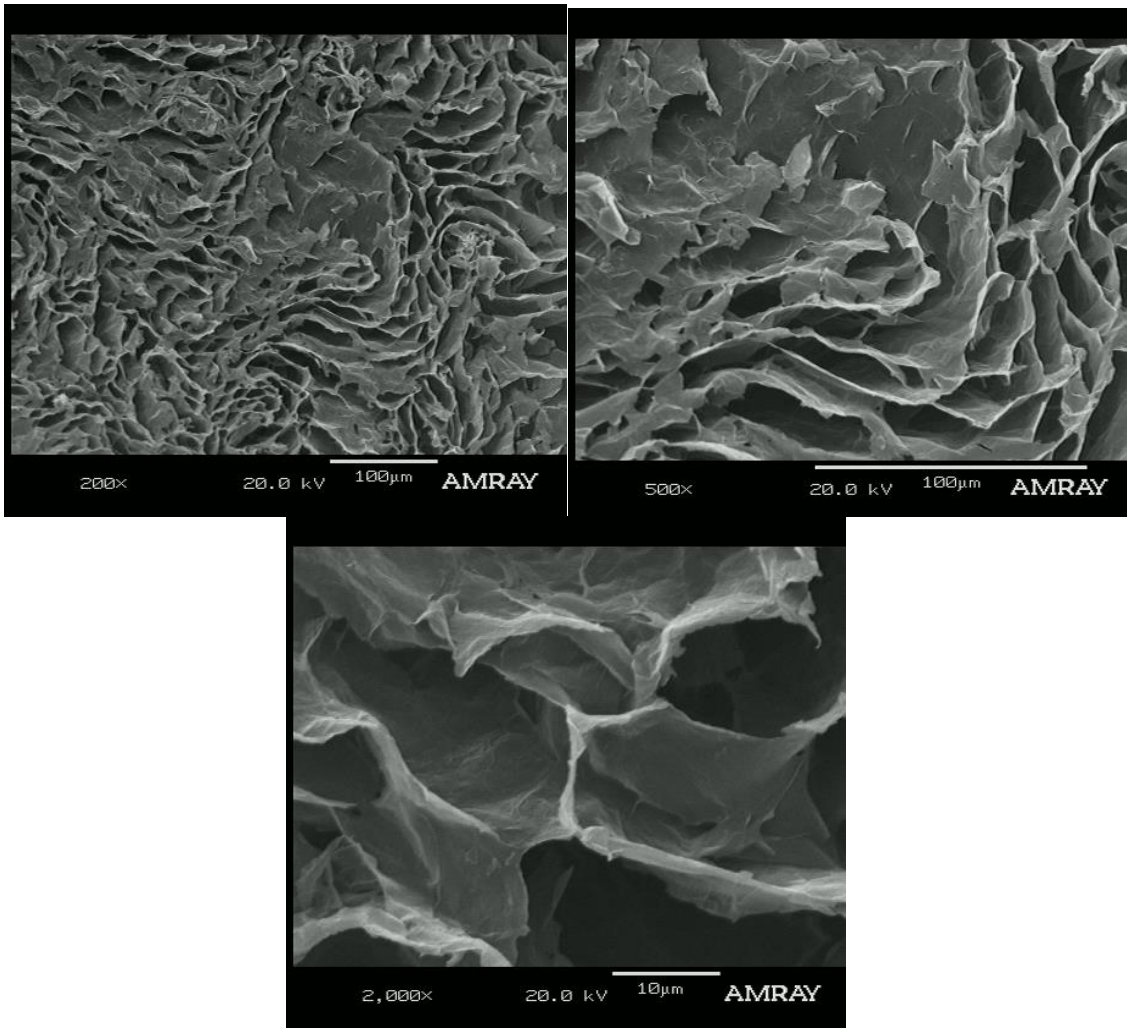

Figure 55: SEM images of HGOM-RF foam sample with solids 5 mg/mL graphene oxide and 5 mg/mL resorcinol formaldehyde resin. (12-5-1)

Analysis of the ice-segregation induced channels in Figure 51, **Figure 52, Figure 54,** and **Figure 55** seem to indicate that ever increasing ratios of graphene oxide to resin may disrupt the channel orientation and regularity in spacing of the channels. However, it is possible to use ice-segregation-induced self-assemble to order and directionally orient the microporous channels within graphene oxide/resorcinol-formaldehyde composites. Finally, we examined a different method of assembly of HGOM-RF foams. The composites were filtered on a 0.2 µm polytetrafluoroethene

(PTFE) filter to consolidate the HGOM particles. Two such examples are shown in the SEM images in **Figure 56**.

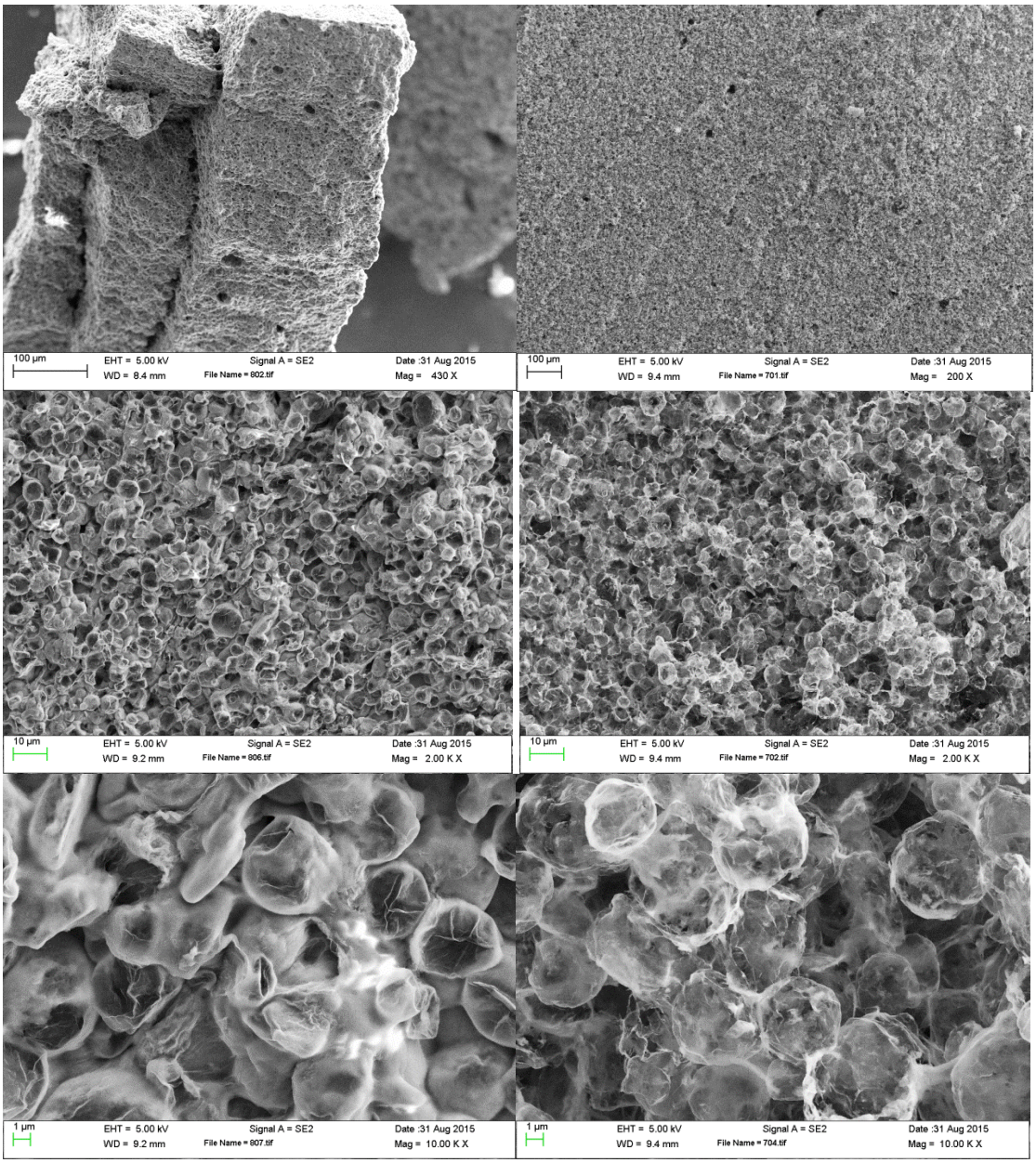

Figure 56: SEM images of made from HGOM-RF/encapsulated PTFE particles set with RF resin to make a solid foam. Left (a), (b), (c) is a higher mass loading of graphene oxide in the composite. Right: (d), (e), (f) is has a low concentration of graphene oxide in the composite. The HGOM shells are somewhat transparent in the sample in (d), (e), (f). (The samples were not sputter coated prior to imaging.) The individual PTFE particles can be seen within the semi-transparent HGOM shells in the SEM image in (f).

4 CONCLUSIONS.

Both thermally reduced GO and thermally reduced RF based gels are prime candidates for a new generation of carbon based energy storage material and have a well-known, but short history of promising results.[29,122,144] Thermal reduction, by pyrolysis in an inert atmosphere, allows for very high electrical conductivity to be achieved for many of the potential applications.

Hierarchical structures are capable of providing many appealing aspects for diverse applications: including catalysis, electrochemical, and electrophysical processes. Building on this background, we have developed several techniques to produce porous structures which can be engineered at the micro-, meso-, and macroporous scales (i.e. (i) the creation of porous structure by "gluing" the HGOM hollow particles with different resins and amines, (ii) by activation of the surface using activation agents such as KOH and (iii) using ice segregation.)

Graphene oxide and resorcinol-formaldehyde based foams were prepared with graphene oxide wall/membrane of thickness between approximately 5 nm and 20 nm. Our results show that the density of the graphene oxide/ resorcinol-formaldehyde based foams range between 5 mg/mL and 80 mg/mL. Upon thermal activation with potassium hydroxide under an inert atmosphere our produced materials revealed surface areas up to 1900 m^2/g. We explored the extent of activation and report this effect on both the meso and micro porous surface areas.

Additionally, we explored a process called ice-segregation-induced self-assembly, which is able to create directional channels through graphene oxide/ resorcinol-formaldehyde foam, and examine different ratios of graphene oxide/ resorcinol-formaldehyde and the resulting structures.

We have used two different techniques to create our foams:

(i) The first method is an emulsion precipitation technique to produce HGOM foams.

(ii) The second one uses ice templating processes.

The beauty of the methods we have invented, of using sublimed scaffolds to structure the foams, have a number of advantages. To the best of our knowledge we do not believe a similar system has been previously described in the literature. Some of the advantages are:

(1) Our method produces lightweight materials (with very thin, ~5 nm structural elements) without collapse during processing due to liquid-vapor surface tension.

(2) With our methods it is possible to control and systematically vary the factors that affect surface chemistry independently of the factors that control the macroporous structure itself. This can be seen in reviewing the activation of a single batch of HGOM-RF, in which different levels of activation was applied. (Table 1, Figure 45, Figure 47, and Figure 49.)

(3) Because of point (2), very high surface area (e.g. 1900 m^2/g) can be achieved while still controlling the macroporous structure. This lends

these materials suitable for a number of applications, including: catalysis, supercapacitors, capacitive desalination, osmotic power production using the capacitive method, and adsorptive remediation of wastes in water, as well as acoustic and thermal insulation, to list only a few applications.

(4) Catalytically active materials, electrochemically active materials (batteries and pseudocapacitors), or polymers suitable for drug loading can be added to the foams with controlled dispersion of the materials throughout the foams.

CHAPTER 5: OVERALL CONCLUSIONS AND FUTURE WORK

5. 1. Overall Conclusions

5.1. 1. Synthesis and Characterization of HGOM particles from Emulsions

- We have produced a novel method of producing nanoscaled HGOM hollow particles after sublimation of a naphthalene core. These structures were produced using an oil-in-water Pickering type emulsion using graphene oxide as the stabilizing agent.
- We have identified processing parameters, such as GO concentration, shear rate and pH that produce graphene oxide stabilized Pickering emulsions
- HGOM particles with diameters as small as 500 nm to 3000 nm were produced for use as carriers for silicon and PTFE nanoparticles, respectively. By decreasing the concentration of graphene oxide, membranes as thin as 3 nm could be produced.
- Because this is fundamentally a directed self-assembly process, it is possible to achieve control over the size of the resulting droplets of the emulsion. It is a directed self-assembly process in the sense, that although the membrane of GO spontaneously forms upon the interface between the oil phase and aqueous phase, energy input (e.g., sonication, rotor-stator, high pressure homogenization, or energetic stirring) is required to finely divide the phases and create the interfacial area. The graphene oxide

provides high stability to the emulsions, on the order of minutes or hours. The emulsions could be stabilized down to graphene oxide concentrations as small as 40 ppm. Increasing the graphene oxide concentrations above 40 ppm enhances the stability of the emulsions.

- Decreasing the pH assists in forming multiple layers of graphene oxide, since lower pH values favor the interactions between individual graphene oxide sheets and these interactions are more favorable than the interactions with the aqueous phase.
- We found that pH conditions which resulted in zeta potentials of approximately -20 mV to -30 mV provided very stable emulsions.
- Future work includes incorporating these HGOMs into foams for use in supercapacitors, as an absorbent for the remediation of oil spills, and core-shell structures for use in catalysis and battery electrodes
- Silicon nanoparticles were encapsulated in hollow graphene shells with controlled void space (yolk-shell particles, a type of core-shell particle) to form an anode with high lithium ion storage capacity. This void space appears to be critical to accommodate the large expansion and contraction of silicon as the battery cycles.
- When thermal reduction (pyrolysis) was applied to the yolk shell particles, powder XRD results confirmed that the graphene oxide sheet spacing was reduced to that similar to graphite (from 2Θ of approximately 12° to 26°, indicating a reduction in sheet spacing from 7 angstroms to 3.4

angstroms). Also the powder XRD pattern confirmed that the silicon nanoparticles remained crystalline, with a calculated diameter of 20 nm.

5.1.2 HGOM Particles for the Creation of Anodes for Li-Ion Batteries

- Yolk-shell anode materials were created with silicon content between 25% and 75%, with the ideal composition of the anodes produced being 75%. Not only was the 75% silicon anode of higher capacity, it was more stable than the 50% silicon anode. It also had a much lower relative capacity reduction when cycled at high charge and discharge rates in relation to the capacity at low rates when compared to the 50% silicon anode.
- Anodes made of yolk-shell particles of 50% silicon were assembled with sodium alginate binder on copper foil current collector and were either left unreduced or chemically reduced with hydrazine vapor.
- The first few cycles of both the unreduced and chemically anodes had nearly identical capacity (just over 1100 mA h/g), however, the chemically reduced anodes exhibited much higher stability as cycling continued.
- Thermally reduced yolk-shell particles were also produced and assembled into anodes with sodium alginate binder on copper foil. At high rates the 75% silicon anodes retained a much higher percentage of the low rate capacity when compared to anodes of 50% silicon.
- We believe that during the emulsion process the larger proportion of graphene oxide may lead to graphene oxide plugging some of the pores spaces around the yolk-shell particles, thus reducing the transport of

lithium by diffusion into the entire depth of the anode. This effect might be solved by reducing the graphene oxide lateral sheet size for lower silicon content anodes, since small sheets of graphene oxide would be less able to bridge the pores on the outside of the yolk-shell particles.

- We also produced free-standing electrodes (with no binder, conductive additive, or copper foil current collector). These electrodes were thermally reduced at 600°C (50% silicon), 700 °C (75% silicon), and 900 °C (75% silicon).
- A free-standing electrode, thermally reduced at 700 °C (75% silicon), exhibited a storage capacity of 1450 mA h/g after 200 cycles and greater than 1300 mA h g-1 after 350 cycles. Capacities greater than 1200 mA-hr/g were possible at a current of 3200 mA/g for an anode thermally reduced at 700 °C. A free-stand anode thermally reduced at 900 °C (75% silicon) also exhibited a storage capacity nearly as high as that produced at 700 °C, with slightly improved cycling stability.
- The coulombic efficiency of both the anodes produced at 700°C and 900 °C rapidly rose as cycling continued, eventually reaching 99.9%. By comparison the anode thermally reduced at 600°C (50% silicon) did not cycle with as much stability compared to those produced at 700 °C and 900 °C.
- Both thermally reduced GO and thermally reduced RF based gels are prime candidates for a new generation of carbon based energy storage material and have a well-known, but short history of promising results.[29,122,144]

Thermal reduction, by pyrolysis in an inert atmosphere, allows for very high electrical conductivity to be achieved for many of the potential applications.

5.1.3 Hierarchical Structured Foams: Ordered Lightweight Foams with High Surface Area

We developed three techniques to produce porous structures which can be engineered at the micro-, meso-, and macroporous scales

(i) the creation of porous structure by "gluing" the HGOM hollow particles with different resins and amines,

(ii) by activation of the surface using activation agents such as KOH and

(iii) by using ice segregation.

- Our foams were synthesized using graphene oxide and resorcinol-formaldehyde and with graphene oxide wall/membrane of thickness between approximately 5 nm and 20 nm.
- The density of the resulting graphene oxide/ resorcinol-formaldehyde based foams ranges between 5 mg/mL and 80 mg/mL.
- Upon thermal activation with potassium hydroxide under an inert atmosphere our produced materials revealed surface areas up to 1900 m^2/g.
- We obtained foams with pore sizes less than 5 nm and others with pore sizes between 5 and 20 nm. The pore size depended on the GO concentration and the initial diameter of the HGOM particles.

- We explored the extent of activation and report this effect on both the meso and micro porous surface areas.
- The ice-segregation-induced self-assembly process yielded directional channels whose directions depended on the concetration ratios of graphene oxide and resorcinol-formaldehyde.
- Our methods produce lightweight materials (with very thin, ~5 nm structural elements) without collapse during processing due to liquid-vapor surface tension. With our methods it is possible to control and systematically vary the factors that affect surface chemistry independently of the factors that control the macroporous structure itself.

5. 2. Future Work:

In this work, HGOM particles were synthesized and fully characterized. Other metal oxides such as Fe_2O_3 and Fe_3O_4 were tested to determine the feasibility of preparing HGOM with different properties; however, these trials were not conclusive. It is recommended to explore HGOM combined with different metal oxides as the active material for the construction of anodes and cathodes. Different combination of Fe_2O_3, Fe_3O_4, SnO_2 or MnO_2 and an entire library of polymers and resins or amine resins and thus possibilities for particle composition is constantly expanding; for example. The use of natural polymers such as chitosan[145], gelatin, fibrin, collagen, and alginate[146] is another avenue that should be explored for the production of new and exciting hollow particles. For example chitosan-linked Fe_3O_4 (CL-Fe_3O_4) can be

prepared by electrostatic interactions between citrate-capped Fe_3O_4 (C-Fe_3O_4) (with negatively charged carboxylate groups) and chitosan oligosaccharide lactate (with positively charged amine groups), and utilized as anodes for lithium-ion batteries.

Chitosan has been shown that be combined with Molibdenun disulfide and graphene [145]. to produce MoS_2/graphene heterostructures. This idea can be expanded into our Hollow graphene particles for Li-ion battery with very promising electrochemical performance. Therefore those materials are good candidates to combine with our graphene oxide particles, for the construction of anode material for lithium-ion batteries.

Another example worth to be explored are MnO_2 particles, which can be grown on the surface of our hollow porous graphene oxide forming a composite MnO_2-graphene oxide for aqueous rechargeable lithium ion batteries. A quick literature search reveals MnO_2 can be combined with graphene to increase their capacity[147]. The incorporation of graphene into the composites can provide them with the unique properties of graphene and also possibly induce new properties and functions based on synergetic effects. The specific capacitance of the composite is evidently much higher than that of the virginal MnO_2.

Also SnO_2 can be combined with Fe_2O_3[148] to produce high surface area. Because of the great synergism between Fe_2O_3 with graphene SnO_2/Fe_2O_3 hybrid combination may also be good candidate to enhance our HGOM particles. Both SnO_2 and Fe_2O_3

contribute to the lithium storage and the hybrid structure exhibits a synergistic effect when participating in electrochemical reactions.

Recent review for asymmetric supercapacitor[149] (i.e. a supercapacitor based on two different electrode materials. One electrode is based on redox reactions, and the other one is mostly based on electric double-layer (electrostatic) absorption/desportion) shows that aqueous electrolytes tend to have higher ionic conductivity, larger capacitance and better safety than the organic electrolytes. Therefore, they propose key electrode materials to work in the future for aqueous asymmetric supercapacitors, which provide a new direction for power sources to have higher energy density at high power densities, compared with traditional capacitors. Negative electrode materials include carbonaceous materials (porous carbons, carbon nanotubes and graphene), oxides (V_2O_5 and MoO_3) and their composites, and their positive electrode materials include carbonaceous materials, oxides (RuO_2, MnO_2, MoO_3, V_2O_5, PbO_2, Co_3O_4), Ni(OH)(2), intercalation compounds ($LiCoO_2$, $LiMn_2O_4$, Li[NiCoMn](1/3)O-2, $NaMnO_2$ and $KMnO_2$.

Other core materials should be explored such as wax that are sublimed with heat. Characterization of tensile and compressive strength, conductivity and electrical properties are avenues worthwhile to be explored.

Additionaly, we have examined the possibility of improve battery cell cycling stability by exploring how functionalization of the silicon nanoparticles improves

the dispersion of the active material within the oil phase of the emulsion, when the particle shells are being formed.

Previously we have hydrogen capped the surface of the silicon nanoparticles to make them hydrophobic However, these results were not conclusive so more studies need to be done, mainly because the hydrogen capped surface may have been oxidized and we were unable to eliminate oxygen from the emulsification system. Although our results were very good, there is the pssibility that the situation may lead to incomplete hydrogen capping by the end of the emulsification process, potentially leading to some of the silicon nanoparticles not in the oil phase.

As a solution to this issue, we propose that in future work, the silicon surface should be treated with a more robust treatment such as an alkane surface treatment. An alkane surface of the nanoparticles is very thermodynamically favorable for incorporation of the silicon nanoparticles exclusively within the oil phase (naphthalene). Perhaps even more important is that the change in surface chemistry of the silicon could allow for other core materials in addition to Naphthalene and the other materials we have identified.

Several methods of achieving alkane capped silicon surfaces have been achieved, with varying coverage fractions and stabilities. Some of the methods, such as those achieved using a radical initiator, achieve a long-chain alkane surface which is stable in a diverse conditions including; organic solvents, air, boiling water, and acids and

bases.[150,151] In the method using a radical initiator, long-chain 1-alkenes are reacted with hydrogen terminated silicon surface at 100°C in the presence of a radical initiator in an organic solvent.[151] Another method uses a photochemical reaction applying UV light to initiate the reaction.[152] One example, that attempts to produce very specific surface treatment of silicon is shown in Figure 57 [used with permisssion from source [151]].

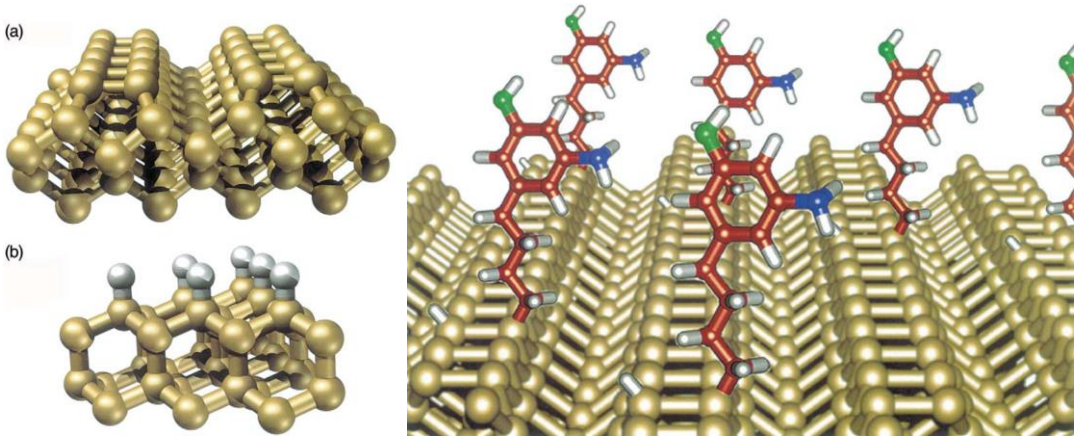

Figure 57: The figure is a cartoon of functionalization of a silicon surface. (a) A silicon surface with no additional chemistry (not even oxygen). (b) The Si (1 1 1) surface is here bonded only to hydrogen, where hydrogen atoms are lighter in color. (c) Illustration of organic molecules attaching to the surface.[151]

REFERENCES

1 Lee, C., Wei, X. D., Kysar, J. W. & Hone, J. Measurement of the elastic properties and intrinsic strength of monolayer graphene. *Science* **321**, 385-388, doi:10.1126/science.1157996 (2008).

2 Singh, V. *et al.* Graphene based materials: Past, present and future. *Prog. Mater. Sci.* **56**, 1178-1271, doi:10.1016/j.pmatsci.2011.03.003 (2011).

3 Goodenough, J. B. & Park, K. S. The Li-Ion Rechargeable Battery: A Perspective. *J. Am. Chem. Soc.* **135**, 1167-1176, doi:10.1021/ja3091438 (2013).

4 Jariwala, D., Sangwan, V. K., Lauhon, L. J., Marks, T. J. & Hersam, M. C. Carbon nanomaterials for electronics, optoelectronics, photovoltaics, and sensing. *Chem. Soc. Rev.* **42**, 2824-2860, doi:10.1039/c2cs35335k (2013).

5 Huang, Y., Liang, J. J. & Chen, Y. S. An Overview of the Applications of Graphene-Based Materials in Supercapacitors. *Small* **8**, 1805-1834, doi:10.1002/smll.201102635 (2012).

6 Novoselov, K. S. *et al.* Electric field effect in atomically thin carbon films. *Science* **306**, 666-669, doi:10.1126/science.1102896 (2004).

7 Geim, A. K. & Novoselov, K. S. The rise of graphene. *Nat. Mater.* **6**, 183-191, doi:10.1038/nmat1849 (2007).

8 Stankovich, S. *et al.* Synthesis of graphene-based nanosheets via chemical reduction of exfoliated graphite oxide. *Carbon* **45**, 1558-1565, doi:10.1016/j.carbon.2007.02.034 (2007).

9 Hu, H. T. *et al.* Preparation and properties of graphene nanosheets-polystyrene nanocomposites via in situ emulsion polymerization. *Chem. Phys. Lett.* **484**, 247-253, doi:10.1016/j.cplett.2009.11.024 (2010).

10 Zhang, L. M., Xia, J. G., Zhao, Q. H., Liu, L. W. & Zhang, Z. J. Functional Graphene Oxide as a Nanocarrier for Controlled Loading and Targeted Delivery of Mixed Anticancer Drugs. *Small* **6**, 537-544, doi:10.1002/smll.200901680 (2010).

11 Bao, H. Q. *et al.* Chitosan-Functionalized Graphene Oxide as a Nanocarrier for Drug and Gene Delivery. *Small* **7**, 1569-1578, doi:10.1002/smll.201100191 (2011).

12 Kim, J. *et al.* Graphene Oxide Sheets at Interfaces. *J. Am. Chem. Soc.* **132**, 8180-8186, doi:10.1021/ja102777p (2010).

13 Xie, P. F. *et al.* Pickering emulsion polymerization of graphene oxide-stabilized styrene. *Colloid Polym. Sci.* **291**, 1631-1639, doi:10.1007/s00396-013-2897-x (2013).

14 Man, S. H. C., Thickett, S. C., Whittaker, M. R. & Zetterlund, P. B. Synthesis of polystyrene nanoparticles "armoured" with nanodimensional graphene

oxide sheets by miniemulsion polymerization. *J. Polym. Sci. Pol. Chem.* **51**, 47-58, doi:10.1002/pola.26341 (2013).

15 Thickett, S. C., Wood, N., Ng, Y. H. & Zetterlund, P. B. Hollow hybrid polymer-graphene oxide nanoparticles via Pickering miniemulsion polymerization. *Nanoscale* **6**, 8590-8594, doi:10.1039/c4nr01175a (2014).

16 Guo, P., Song, H. H. & Chen, X. H. Hollow graphene oxide spheres self-assembled by W/O emulsion. *Journal of Materials Chemistry* **20**, 4867-4874, doi:10.1039/b927302f (2010).

17 Luo, J. Y. *et al.* Crumpled Graphene-Encapsulated Si Nanoparticles for Lithium Ion Battery Anodes. *J. Phys. Chem. Lett.* **3**, 1824-1829, doi:10.1021/jz3006892 (2012).

18 Etmimi, H. M., Mallon, P. E. & Sanderson, R. D. Polymer/graphite nanocomposites: Effect of reducing the functional groups of graphite oxide on water barrier properties. *Eur. Polym. J.* **49**, 3460-3470, doi:10.1016/j.eurpolymj.2013.08.004 (2013).

19 Luo, Q. M., Wei, P. R. & Pentzer, E. Hollow microcapsules by stitching together of graphene oxide nanosheets with a di-functional small molecule. *Carbon* **106**, 125-131, doi:10.1016/j.carbon.2016.05.024 (2016).

20 Guan, Y., Yu, L. & Lou, X. W. Chemically Assisted Formation of Monolayer Colloidosomes on Functional Particles. *Adv. Mater.* **28**, 9596-+, doi:10.1002/adma.201603622 (2016).

21 Guan, B. Y., Yu, L. & Lou, X. W. Formation of Asymmetric Bowl-Like Mesoporous Particles via Emulsion-Induced Interface Anisotropic Assembly. *J. Am. Chem. Soc.* **138**, 11306-11311, doi:10.1021/jacs.6b06558 (2016).

22 Buchold, D. H. M. & Feldmann, C. Nanoscale gamma-AlO(OH) hollow spheres: Synthesis and container-type functionality. *Nano Lett.* **7**, 3489-3492, doi:10.1021/nl072074f (2007).

23 Feng, L. Y., Wu, L. & Qu, X. G. New Horizons for Diagnostics and Therapeutic Applications of Graphene and Graphene Oxide. *Adv. Mater.* **25**, 168-186, doi:10.1002/adma.201203229 (2013).

24 Yang, K., Feng, L. Z., Shi, X. Z. & Liu, Z. Nano-graphene in biomedicine: theranostic applications. *Chem. Soc. Rev.* **42**, 530-547, doi:10.1039/c2cs35342c (2013).

25 Shen, H., Zhang, L. M., Liu, M. & Zhang, Z. J. Biomedical Applications of Graphene. *Theranostics* **2**, 283-294, doi:10.7150/thno.3642 (2012).

26 Kovtyukhova, N. I. *et al.* Layer-by-layer assembly of ultrathin composite films from micron-sized graphite oxide sheets and polycations. *Chem. Mat.* **11**, 771-778, doi:10.1021/cm981085u (1999).

27 Kerdouss, F. *et al.* Two-phase mass transfer coefficient prediction in stirred vessel with a CFD model. *Comput. Chem. Eng.* **32**, 1943-1955, doi:10.1016/j.compchemeng.2007.10.010 (2008).

28 Luo, J. Y. *et al.* Graphene Oxide Nanocolloids. *J. Am. Chem. Soc.* **132**, 17667-17669, doi:10.1021/ja1078943 (2010).

29 Lee, J. K., Smith, K. B., Hayner, C. M. & Kung, H. H. Silicon nanoparticles-graphene paper composites for Li ion battery anodes. *Chem. Commun.* **46**, 2025-2027, doi:10.1039/b919738a (2010).

30 Aveyard, R., Binks, B. P. & Clint, J. H. Emulsions stabilised solely by colloidal particles. *Adv. Colloid Interface Sci.* **100**, 503-546, doi:10.1016/s0001-8686(02)00069-6 (2003).

31 Tomassone, M. S., Couzis, A., Maldarelli, C., Banavar, J. R. & Koplik, J. Phase transitions of soluble surfactants at a liquid-vapor interface. *Langmuir* **17**, 6037-6040, doi:10.1021/la0103113 (2001).

32 Jones, C. D. & Lyon, L. A. Synthesis and characterization of multiresponsive core-shell microgels. *Macromolecules* **33**, 8301-8306, doi:10.1021/ma001398m (2000).

33 Garbuzenko, O. B., Winkler, J., Tomassone, M. S. & Minko, T. Biodegradable Janus Nanoparticles for Local Pulmonary Delivery of Hydrophilic and Hydrophobic Molecules to the Lungs. *Langmuir* **30**, 12941-12949, doi:10.1021/la502144z (2014).

34 Romanski, F. S., Winkler, J. S., Riccobene, R. C. & Tomassone, M. S. Production and Characterization of Anisotropic Particles from Biodegradable Materials. *Langmuir* **28**, 3756-3765, doi:10.1021/la2044834 (2012).

35 Liu, Z., Robinson, J. T., Sun, X. M. & Dai, H. J. PEGylated nanographene oxide for delivery of water-insoluble cancer drugs. *J. Am. Chem. Soc.* **130**, 10876-+, doi:10.1021/ja803688x (2008).

36 Sun, X. M. *et al.* Nano-Graphene Oxide for Cellular Imaging and Drug Delivery. *Nano Res.* **1**, 203-212, doi:10.1007/s12274-008-8021-8 (2008).

37 Tarascon, J. M. & Armand, M. Issues and challenges facing rechargeable lithium batteries. *Nature* **414**, 359-367, doi:10.1038/35104644 (2001).

38 Chan, C. K. *et al.* High-performance lithium battery anodes using silicon nanowires. *Nat. Nanotechnol.* **3**, 31-35, doi:10.1038/nnano.2007.411 (2008).

39 Lee, K. T. & Cho, J. Roles of nanosize in lithium reactive nanomaterials for lithium ion batteries. *Nano Today* **6**, 28-41, doi:10.1016/j.nantod.2010.11.002 (2011).

40 Zhang, T. *et al.* Natural graphite coated by Si nanoparticles as anode materials for lithium ion batteries. *Journal of Materials Chemistry* **17**, 1321-1325, doi:10.1039/b612967f (2007).

41 Xiang, H. F. *et al.* Graphene/nanosized silicon composites for lithium battery anodes with improved cycling stability. *Carbon* **49**, 1787-1796, doi:10.1016/j.carbon.2011.01.002 (2011).

42 Su, M. R. *et al.* Multi-layered carbon coated Si-based composite as anode for lithium-ion batteries. *Powder Technol.* **323**, 294-300, doi:10.1016/j.powtec.2017.09.005 (2018).

43 Su, M. R. *et al.* Silicon@graphene composite prepared by spray-drying method as anode for lithium ion batteries. *J. Electroanal. Chem.* **844**, 86-90, doi:10.1016/j.jelechem.2019.04.072 (2019).

44 Liu, M. X. *et al.* Core-shell reduced graphene oxide/MnOx@carbon hollow nanospheres for high performance supercapacitor electrodes. *Chem. Eng. J.* **313**, 518-526, doi:10.1016/j.cej.2016.12.091 (2017).

45 Yang, L. Y. *et al.* Dual yolk-shell structure of carbon and silica-coated silicon for high-performance lithium-ion batteries. *Scientific Reports* **5**, 9, doi:10.1038/srep10908 (2015).

46 Qi, Y., Guo, H. B., Hector, L. G. & Timmons, A. Threefold Increase in the Young's Modulus of Graphite Negative Electrode during Lithium Intercalation. *J. Electrochem. Soc.* **157**, A558-A566, doi:10.1149/1.3327913 (2010).

47 McDowell, M. T., Lee, S. W., Nix, W. D. & Cui, Y. 25th Anniversary Article: Understanding the Lithiation of Silicon and Other Alloying Anodes for Lithium-Ion Batteries. *Adv. Mater.* **25**, 4966-4984, doi:10.1002/adma.201301795 (2013).

48 Liu, X. H. *et al.* Size-Dependent Fracture of Silicon Nanoparticles During Lithiation. *ACS Nano* **6**, 1522-1531, doi:10.1021/nn204476h (2012).

49 McDowell, M. T. *et al.* In Situ TEM of Two-Phase Lithiation of Amorphous Silicon Nanospheres. *Nano Lett.* **13**, 758-764, doi:10.1021/nl3044508 (2013).

50 Lee, S. W., McDowell, M. T., Berla, L. A., Nix, W. D. & Cui, Y. Fracture of crystalline silicon nanopillars during electrochemical lithium insertion. *Proc. Natl. Acad. Sci. U. S. A.* **109**, 4080-4085, doi:10.1073/pnas.1201088109 (2012).

51 Xu, K. Nonaqueous liquid electrolytes for lithium-based rechargeable batteries. *Chem. Rev.* **104**, 4303-4417, doi:10.1021/cr030203g (2004).

52 Liu, N. *et al.* A Yolk-Shell Design for Stabilized and Scalable Li-Ion Battery Alloy Anodes. *Nano Lett.* **12**, 3315-3321, doi:10.1021/nl3014814 (2012).

53 Lu, W. J. *et al.* Core-shell materials for advanced batteries. *Chem. Eng. J.* **355**, 208-237, doi:10.1016/j.cej.2018.08.132 (2019).

54 Zhang, Q., Lee, I., Joo, J. B., Zaera, F. & Yin, Y. D. Core-Shell Nanostructured Catalysts. *Accounts Chem. Res.* **46**, 1816-1824, doi:10.1021/ar300230s (2013).

55 Smith, K. B. & Tomassone, M. S. Ultrathin Hollow Graphene Oxide Membranes for Use as Nanoparticle Carriers. *Langmuir* **33**, 3765-3775, doi:10.1021/acs.langmuir.6b04583 (2017).

56 Zhou, Y. *et al.* Facile synthesis of silicon/carbon nanospheres composite anode materials for lithium-ion batteries. *Mater. Lett.* **168**, 138-142, doi:10.1016/j.matlet.2016.01.009 (2016).

57 Wu, C. *et al.* A Review: Enhanced Anodes of Li/Na-Ion Batteries Based on Yolk-Shell Structured Nanomaterials. *Nano-Micro Lett.* **10**, 18, doi:10.1007/s40820-018-0194-4 (2018).

58 Mi, H. W., Yang, X. D., Li, Y. L., Zhang, P. X. & Sun, L. N. A self-sacrifice template strategy to fabricate yolk-shell structured silicon@void@carbon composites for high-performance lithium-ion batteries. *Chem. Eng. J.* **351**, 103-109, doi:10.1016/j.cej.2018.06.065 (2018).

59 Liu, N. *et al.* A pomegranate-inspired nanoscale design for large-volume-change lithium battery anodes. *Nat. Nanotechnol.* **9**, 187-192, doi:10.1038/nnano.2014.6 (2014).

60 Zhai, W. *et al.* Walnut-inspired microsized porous silicon/graphene core-shell composites for high-performance lithium-ion battery anodes. *Nano Res.* **10**, 4274-4283, doi:10.1007/s12274-017-1584-5 (2017).

61 Xiang, Y., Chen, Z., Chen, C. M., Wang, T. H. & Zhang, M. Design and synthesis of Cr2O3@C@G composites with yolk-shell structure for Li+ storage. *J. Alloy. Compd.* **724**, 406-412, doi:10.1016/j.jallcom.2017.07.052 (2017).

62 Chazalviel, J. N. & Ozanam, F. In situ infrared characterization of the silicon surface in hydrofluoric acid. *J. Appl. Phys.* **81**, 7684-7686, doi:10.1063/1.365348 (1997).

63 Linford, M. R. & Chidsey, C. E. D. ALKYL MONOLAYERS COVALENTLY BONDED TO SILICON SURFACES. *J. Am. Chem. Soc.* **115**, 12631-12632, doi:10.1021/ja00079a071 (1993).

64 Tomasini, M. D., Rinaldi, C. & Tomassone, M. S. Molecular dynamics simulations of rupture in lipid bilayers. *Exp. Biol. Med.* **235**, 181-188, doi:10.1258/ebm.2009.009187 (2010).

65 Wu, R. H. *et al.* Preparation of graphene sponge by vapor phase reduction for oil and organic solvent removal. *Mater. Res. Express* **3**, 7, doi:10.1088/2053-1591/3/10/105602 (2016).

66 (ed Sergey Mikhailov) 540 (InTech, , 2011).

67 Chen, W. F., Yan, L. F. & Bangal, P. R. Preparation of graphene by the rapid and mild thermal reduction of graphene oxide induced by microwaves. *Carbon* **48**, 1146-1152, doi:10.1016/j.carbon.2009.11.037 (2010).

68 Paredes, J. I., Villar-Rodil, S., Solis-Fernandez, P., Martinez-Alonso, A. & Tascon, J. M. D. Atomic Force and Scanning Tunneling Microscopy Imaging of Graphene Nanosheets Derived from Graphite Oxide. *Langmuir* **25**, 5957-5968, doi:10.1021/la804216z (2009).

69 Lie, L. H. *et al.* Immobilisation and synthesis of DNA on Si(111), nanocrystalline porous silicon and silicon nanoparticles. *Faraday Discuss.* **125**, 235-249, doi:10.1039/b302845c (2004).

70 Piscanec, S. *et al.* Raman spectrum of silicon nanowires. *Mater. Sci. Eng. C-Biomimetic Supramol. Syst.* **23**, 931-934, doi:10.1016/j.msec.2003.09.084 (2003).

71 Meador, M. A. B., Capadona, L. A., McCorkle, L., Papadopoulos, D. S. & Leventis, N. Structure-property relationships in porous 3D nanostructures as a function of preparation conditions: Isocyanate cross-linked silica aerogels. *Chem. Mat.* **19**, 2247-2260, doi:10.1021/cm070102p (2007).

72 Zhang, K., Ang, B. T., Zhang, L. L., Zhao, X. S. & Wu, J. S. Pyrolyzed graphene oxide/resorcinol-formaldehyde resin composites as high-performance supercapacitor electrodes. *Journal of Materials Chemistry* **21**, 2663-2670, doi:10.1039/c0jm02850a (2011).

73 Dikin, D. A. *et al.* Preparation and characterization of graphene oxide paper. *Nature* **448**, 457-460, doi:10.1038/nature06016 (2007).

74 Chen, H., Muller, M. B., Gilmore, K. J., Wallace, G. G. & Li, D. Mechanically strong, electrically conductive, and biocompatible graphene paper. *Adv. Mater.* **20**, 3557-+, doi:10.1002/adma.200800757 (2008).

75 Zhu, Y. W. *et al.* Graphene and Graphene Oxide: Synthesis, Properties, and Applications. *Adv. Mater.* **22**, 3906-3924, doi:10.1002/adma.201001068 (2010).

76 Zhang, X. T. *et al.* Mechanically strong and highly conductive graphene aerogel and its use as electrodes for electrochemical power sources. *Journal of Materials Chemistry* **21**, 6494-6497, doi:10.1039/c1jm10239g (2011).

77 Xu, Y. X., Sheng, K. X., Li, C. & Shi, G. Q. Self-Assembled Graphene Hydrogel via a One-Step Hydrothermal Process. *ACS Nano* **4**, 4324-4330, doi:10.1021/nn101187z (2010).

78 Yuan, Z. Y. & Su, B. L. Insights into hierarchically meso-macroporous structured materials. *Journal of Materials Chemistry* **16**, 663-677, doi:10.1039/b512304f (2006).

79 Feinle, A., Elsaesser, M. S. & Husing, N. Sol-gel synthesis of monolithic materials with hierarchical porosity. *Chem. Soc. Rev.* **45**, 3377-3399, doi:10.1039/c5cs00710k (2016).

80 Budhiraju, V. S., Kumar, R., Sharma, A. & Sivakumar, S. Structurally stable hollow mesoporous graphitized carbon nanofibers embedded with NiMoO4 nanoparticles for high performance asymmetric supercapacitors. *Electrochim. Acta* **238**, 337-348, doi:10.1016/j.electacta.2017.04.039 (2017).

81 Yang, L. *et al.* Structuring the reduced graphene oxide/polyHIPE foam for piezoresistive sensing via emulsion-templated polymerization. *Composites Part a-Applied Science and Manufacturing* **134**, doi:10.1016/j.compositesa.2020.105898 (2020).

82 Wang, W. D. *et al.* Synthesis and electrochemical performance of gold nanoparticles deposited onto a reduced graphene oxide/nickel foam hybrid structure for hydrazine detection. *Journal of Materials Science*, doi:10.1007/s10853-020-04684-6.

83 Karimi, A., Kazeminezhad, I., Naderi, L. & Shahrokhian, S. Construction of a Ternary Nanocomposite, Polypyrrole/Fe-Co Sulfide-Reduced Graphene Oxide/Nickel Foam, as a Novel Binder-Free Electrode for High-Performance Asymmetric Supercapacitors. *Journal of Physical Chemistry C* **124**, 4393-4407, doi:10.1021/acs.jpcc.9b11010 (2020).

84 He, R. A., Lou, Z. M., Gui, J., Tang, B. & Xu, D. F. Room-temperature synthesis of BiOI/Graphene oxide foam composite for phenol removal under visible light. *Applied Surface Science* **504**, doi:10.1016/j.apsusc.2019.144370 (2020).

85 Guo, X. J. *et al.* A chitosan-graphene oxide/ZIF foam with anti-biofouling ability for uranium recovery from seawater. *Chemical Engineering Journal* **382**, doi:10.1016/j.cej.2019.122850 (2020).

86 Sun, L. M., Wen, F. C., Shi, L. L. & Li, S. Pd and CoOx decorated reduced graphene oxide self-assembled on Ni foam as Al-H2O2 semi-fuel cells cathodes. *Journal of Alloys and Compounds* **815**, doi:10.1016/j.jallcom.2019.152361 (2020).

87 Liang, C. B. *et al.* Constructing interconnected spherical hollow conductive networks in silver platelets/reduced graphene oxide foam/epoxy nanocomposites for superior electromagnetic interference shielding effectiveness. *Nanoscale* **11**, 22590-22598, doi:10.1039/c9nr06022g (2019).

88 Li, B. P. *et al.* Reduced graphene oxide foam supported CoNi nanosheets as an efficient anode catalyst for direct borohydride hydrogen peroxide fuel cell. *Applied Surface Science* **491**, 659-669, doi:10.1016/j.apsusc.2019.06.110 (2019).

89 Li, H. S. *et al.* Construction of core-shell cobalt sulfide/manganese molybdate nanostructure on reduced graphene oxide/Ni foam as an advanced electrode for high-performance asymmetric supercapacitor. *Electrochimica Acta* **312**, 213-223, doi:10.1016/j.electacta.2019.05.008 (2019).

90 Zhu, Y. *et al.* High Internal Phase Oil-in-Water Pickering Emulsions Stabilized by Chitin Nanofibrils: 3D Structuring and Solid Foam. *Acs Applied Materials & Interfaces* **12**, 11240-11251, doi:10.1021/acsami.9b23430 (2020).

91 Pan, J. M. *et al.* Competitive adsorption of three phenolic compounds to hydrophilic urea-formaldehyde macroporous foams derived from lignin-based Pickering HIPEs template. *Rsc Advances* **6**, 93894-93904, doi:10.1039/c6ra20919j (2016).

92 Li, X. N., Zhu, C. L., Wei, Y. Z. & Lu, Z. J. Fabrication of macroporous foam and microspheres of polystyrene by Pickering emulsion polymerization. *Colloid and Polymer Science* **292**, 115-122, doi:10.1007/s00396-013-3058-y (2014).

93 Yu, H., Wang, Q., Zhao, Y. L. & Wang, H. T. A Convenient and Versatile Strategy for the Functionalization of Silica Foams Using High Internal Phase Emulsion Templates as Microreactors. *Acs Applied Materials & Interfaces* **12**, 14607-14619, doi:10.1021/acsami.0c01273 (2020).

94 Gibson, L. J. Mechanical behavior of metallic foams. *Annu. Rev. Mater. Sci.* **30**, 191-227, doi:10.1146/annurev.matsci.30.1.191 (2000).

95 Chung, H. J. & Park, T. G. Surface engineered and drug releasing pre-fabricated scaffolds for tissue engineering. *Adv. Drug Deliv. Rev.* **59**, 249-262, doi:10.1016/j.addr.2007.03.015 (2007).

96 Twigg, M. V. & Richardson, J. T. Fundamentals and applications of structured ceramic foam catalysts. *Ind. Eng. Chem. Res.* **46**, 4166-4177, doi:10.1021/ie061122o (2007).

97 Garcia-Moreno, F. Commercial Applications of Metal Foams: Their Properties and Production. *Materials* **9**, 27, doi:10.3390/ma9020085 (2016).

98 Zhang, F. Q. *et al.* Ordered bimodal mesoporous silica with tunable pore structure and morphology. *Microporous Mesoporous Mat.* **98**, 6-15, doi:10.1016/j.micromeso.2006.08.013 (2007).

99 Hossain, M. S. & Shabani, B. Metal foams application to enhance cooling of open cathode polymer electrolyte membrane fuel cells. *J. Power Sources* **295**, 275-291, doi:10.1016/j.jpowsour.2015.07.022 (2015).

100 Sommers, A. *et al.* Ceramics and ceramic matrix composites for heat exchangers in advanced thermal systems-A review. *Appl. Therm. Eng.* **30**, 1277-1291, doi:10.1016/j.applthermaleng.2010.02.018 (2010).

101 Zhou, Y. G. & Chen, T. Y. Combining foam injection molding with batch foaming to improve cell density and control cellular orientation via multiple gas dissolution and desorption processes. *Polym. Adv. Technol.*, 16, doi:10.1002/pat.4935.

102 Jaouen, L., Renault, A. & Deverge, M. Elastic and damping characterizations of acoustical porous materials: Available experimental methods and applications to a melamine foam. *Appl. Acoust.* **69**, 1129-1140, doi:10.1016/j.apacoust.2007.11.008 (2008).

103 Srivastava, V. & Srivastava, R. On the polymeric foams: modeling and properties. *J. Mater. Sci.* **49**, 2681-2692, doi:10.1007/s10853-013-7974-5 (2014).

104 Baughman, R. H., Shacklette, J. M., Zakhidov, A. A. & Stafstrom, S. Negative Poisson's ratios as a common feature of cubic metals. *Nature* **392**, 362-365, doi:10.1038/32842 (1998).

105 Lakes, R. ADVANCES IN NEGATIVE POISSONS RATIO MATERIALS. *Adv. Mater.* **5**, 293-296, doi:10.1002/adma.19930050416 (1993).

106 Hartmann, M. & Schwieger, W. Hierarchically-structured porous materials: from basic understanding to applications. *Chem. Soc. Rev.* **45**, 3311-3312, doi:10.1039/c6cs90043g (2016).

107 Lakes, R. MATERIALS WITH STRUCTURAL HIERARCHY. *Nature* **361**, 511-515, doi:10.1038/361511a0 (1993).

108 Schwieger, W. *et al.* Hierarchy concepts: classification and preparation strategies for zeolite containing materials with hierarchical porosity. *Chem. Soc. Rev.* **45**, 3353-3376, doi:10.1039/c5cs00599j (2016).

109 Hartmann, M., Machoke, A. G. & Schwieger, W. Catalytic test reactions for the evaluation of hierarchical zeolites. *Chem. Soc. Rev.* **45**, 3313-3330, doi:10.1039/c5cs00935a (2016).

110 *Novel Nanomaterials for Biomedical, Environmental and Energy Applications*. (2019).

111 Rolison, D. R. Catalytic nanoarchitectures - The importance of nothing and the unimportance of periodicity. *Science* **299**, 1698-1701, doi:10.1126/science.1082332 (2003).

112 Koresh, J. & Soffer, A. Double Layer Capacitance and Charging Rate of Ultramicroporous Carbon Electrodes. *J. Electrochem. Soc.* **9**, 1379-1385 (1977).

113 Nielsen, T. K., Manickam, K., Hirscher, M., Besenbacher, F. & Jensen, T. R. Confinement of MgH2 Nanoclusters within Nanoporous Aerogel Scaffold Materials. *ACS Nano* **3**, 3521-3528, doi:10.1021/nn901072w (2009).

114 Gross, A. F., Vajo, J. J., Van Atta, S. L. & Olson, G. L. Enhanced hydrogen storage kinetics of LiBH4 in nanoporous carbon scaffolds. *J. Phys. Chem. C* **112**, 5651-5657, doi:10.1021/jp711066t (2008).

115 Hwang, S. W. & Hyun, S. H. Synthesis and characterization of tin oxide/carbon aerogel composite electrodes for electrochemical supercapacitors. *J. Power Sources* **172**, 451-459, doi:10.1016/j.jpowsour.2007.07.061 (2007).

116 Li, J., Wang, X. Y., Huang, Q. H., Gamboa, S. & Sebastian, P. J. Studies on preparation and performances of carbon aerogel electrodes for the application of supercapacitor. *J. Power Sources* **158**, 784-788, doi:10.1016/j.jpowsour.2005.09.045 (2006).

117 Le, D. B. *et al.* High surface area V2O5 aerogel intercalation electrodes. *J. Electrochem. Soc.* **143**, 2099-2104, doi:10.1149/1.1836965 (1996).

118 Moreno-Castilla, C. & Maldonado-Hodar, F. J. Carbon aerogels for catalysis applications: An overview. *Carbon* **43**, 455-465, doi:10.1016/j.carbon.2004.10.022 (2005).

119 Fang, B. Z. & Binder, L. A modified activated carbon aerogel for high-energy storage in electric double layer capacitors. *J. Power Sources* **163**, 616-622, doi:10.1016/j.jpowsour.2006.09.014 (2006).

120 Zhu, Y. W. *et al.* Carbon-Based Supercapacitors Produced by Activation of Graphene. *Science* **332**, 1537-1541, doi:10.1126/science.1200770 (2011).

121 Nielsen, T. K., Besenbacher, F. & Jensen, T. R. Nanoconfined hydrides for energy storage. *Nanoscale* **3**, 2086-2098, doi:10.1039/c0nr00725k (2011).

122 Biener, J. *et al.* Advanced carbon aerogels for energy applications. *Energy Environ. Sci.* **4**, 656-667, doi:10.1039/c0ee00627k (2011).

123 Brogioli, D. Extracting Renewable Energy from a Salinity Difference Using a Capacitor. *Physical Review Letters* **103**, 058501 (2009).

124 Boon, N. & van Roij, R. 'Blue energy' from ion adsorption and electrode charging in sea and river water. *Mol. Phys.* **109**, 1229-1241, doi:10.1080/00268976.2011.554334 (2011).

125 Brogioli, D. *et al.* Exploiting the spontaneous potential of the electrodes used in the capacitive mixing technique for the extraction of energy from salinity difference. *Energy Environ. Sci.* **5**, 9870-9880, doi:10.1039/c2ee23036d (2012).

126 Rica, R. A. *et al.* Electro-diffusion of ions in porous electrodes for capacitive extraction of renewable energy from salinity differences. *Electrochim. Acta* **92**, 304-314, doi:10.1016/j.electacta.2013.01.063 (2013).

127 Mesalhy, O., Lafdi, K. & Elgafy, A. Carbon foam matrices saturated with PCM for thermal protection purposes. *Carbon* **44**, 2080-2088, doi:10.1016/j.carbon.2005.12.019 (2006).

128 Chung, D. D. L. Electromagnetic interference shielding effectiveness of carbon materials. *Carbon* **39**, 279-285, doi:10.1016/s0008-6223(00)00184-6 (2001).

129 Worsley, M. A. *et al.* High Surface Area, sp(2)-Cross-Linked Three-Dimensional Graphene Monoliths. *J. Phys. Chem. Lett.* **2**, 921-925, doi:10.1021/jz200223x (2011).

130 Yu, Y. Y., Wang, Y. L., Deng, P. H. & Zhang, T. H. Fe3O4@rGO hybrids intercalated nanocellulose-based aerogels for enhanced ferromagnetic and

mechanical properties. *J. Appl. Polym. Sci.* **137**, doi:10.1002/app.48564 (2020).

131 Pekala, R. W. ORGANIC AEROGELS FROM THE POLYCONDENSATION OF RESORCINOL WITH FORMALDEHYDE. *J. Mater. Sci.* **24**, 3221-3227, doi:10.1007/bf01139044 (1989).

132 Zhou, G. M. *et al.* Graphene-Wrapped Fe(3)O(4) Anode Material with Improved Reversible Capacity and Cyclic Stability for Lithium Ion Batteries. *Chem. Mat.* **22**, 5306-5313, doi:10.1021/cm101532x (2010).

133 Liu, C. G., Yu, Z. N., Neff, D., Zhamu, A. & Jang, B. Z. Graphene-Based Supercapacitor with an Ultrahigh Energy Density. *Nano Lett.* **10**, 4863-4868, doi:10.1021/nl102661q (2010).

134 Islam, A., Ahmad, H., Zaidi, N. & Kumar, S. A graphene oxide decorated with triethylenetetramine-modified magnetite for separation of chromium species prior to their sequential speciation and determination via FAAS. *Microchim. Acta* **183**, 289-296, doi:10.1007/s00604-015-1641-2 (2016).

135 Mahler, W. & Bechtold, M. F. FREEZE-FORMED SILICA FIBERS. *Nature* **285**, 27-28, doi:10.1038/285027a0 (1980).

136 Gutierrez, M. C., Ferrer, M. L. & del Monte, F. Ice-templated materials: Sophisticated structures exhibiting enhanced functionalities obtained after unidirectional freezing and ice-segregation-induced self-assembly. *Chem. Mat.* **20**, 634-648, doi:10.1021/cm702028z (2008).

137 Han, S. *et al.* Carbon encapsulated Fe3O4/graphene framework with oriented macropores for lithium ion battery anode with enhanced cycling stability. *RSC Adv.* **5**, 98399-98403, doi:10.1039/c5ra20257d (2015).

138 Arndt, E. M., Gawryla, M. D. & Schiraldi, D. A. Elastic, low density epoxy/clay aerogel composites. *Journal of Materials Chemistry* **17**, 3525-3529, doi:10.1039/b704114d (2007).

139 Neimark, A. V., Lin, Y. Z., Ravikovitch, P. I. & Thommes, M. Quenched solid density functional theory and pore size analysis of micro-mesoporous carbons. *Carbon* **47**, 1617-1628, doi:10.1016/j.carbon.2009.01.050 (2009).

140 Landers, J., Gor, G. Y. & Neimark, A. V. Density functional theory methods for characterization of porous materials. *Colloid Surf. A-Physicochem. Eng. Asp.* **437**, 3-32, doi:10.1016/j.colsurfa.2013.01.007 (2013).

141 Lazar, P. *et al.* Adsorption of Small Organic Molecules on Graphene. *J. Am. Chem. Soc.* **135**, 6372-6377, doi:10.1021/ja403162r (2013).

142 Ko, T. H., Kuo, W. S. & Chang, Y. H. Raman study of the microstructure changes of phenolic resin during pyrolysis. *Polym. Compos.* **21**, 745-750, doi:10.1002/pc.10229 (2000).

143 Thommes, M. *et al.* Physisorption of gases, with special reference to the evaluation of surface area and pore size distribution (IUPAC Technical Report). *Pure Appl. Chem.* **87**, 1051-1069, doi:10.1515/pac-2014-1117 (2015).

144 Frackowiak, E. & Beguin, F. Carbon materials for the electrochemical storage of energy in capacitors. *Carbon* **39**, 937-950, doi:10.1016/s0008-6223(00)00183-4 (2001).

145 Ma, L. *et al.* Chitosan-assisted fabrication of ultrathin MoS2/graphene heterostructures for Li-ion battery with excellent electrochemical performance. *ELECTROCHIMICA ACTA* **167** Pages: 39-47 (2015).

146 Huang, H. B. *et al.* High-performance Si flexible anode with rGO substrate and Ca2+ crosslinked sodium alginate binder for lithium ion battery. *Synthetic Metals* **247**, 212-218, doi:10.1016/j.synthmet.2018.12.011 (2019).

147 Z. Fan *et al.* Asymmetric Supercapacitors Based on Graphene/MnO2 and Activated Carbon Nanofiber Electrodes with High Power and Energy Density *Adv. Funct. Mater.* **21**, 2366 (2011).

148 Zan, F. *et al.* SnO2/Fe2O3 hybrid nanofibers as high performance anodes for lithium-ion batteries. *Nanotechnology* **31**, doi:10.1088/1361-6528/ab6d1f (2020).

149 Wang, F. X. *et al.* Electrode materials for aqueous asymmetric supercapacitors. *Rsc Advances* **3**, 13059-13084, doi:10.1039/c3ra23466e (2013).

150 Hua, F. J., Erogbogbo, F., Swihart, M. T. & Ruckenstein, E. Organically capped silicon nanoparticles with blue photoluminescence prepared by hydrosilylation followed by oxidation. *Langmuir* **22**, 4363-4370, doi:10.1021/la0529106 (2006).

151 Bent, S. F. Organic functionalization of group IV semiconductor surfaces: principles, examples, applications, and prospects. *Surf. Sci.* **500**, 879-903, doi:10.1016/s0039-6028(01)01553-9 (2002).

152 DeBenedetti, W. J. I. *et al.* Conversion from Red to Blue Photoluminescence in Alcohol Dispersions of Alkyl-Capped Silicon Nanoparticles: Insight into the Origins of Visible Photoluminescence in Colloidal Nanocrystalline Silicon. *J. Phys. Chem. C* **119**, 9595-9608, doi:10.1021/acs.jpcc.5b01137 (2015).